2013

The Development of tunable metalation resistant pincer ligands for supporting f-elements

Kamenz, Breanne Leigh

Lethbridge, Alta. : University of Lethbridge, Dept. of Chemistry and Biochemistry

THE DEVELOPMENT OF TUNABLE METALATION RESISTANT PINCER LIGANDS FOR SUPPORTING *f*-ELEMENTS

BREANNE LEIGH KAMENZ
Bachelor of Science, University of Lethbridge, 2011

A Dissertation
Submitted to the School of Graduate Studies
of the University of Lethbridge
in Partial Fulfilment of the
Requirements for the Degree

MASTER OF SCIENCE

Department of Chemistry and Biochemistry
University of Lethbridge
LETHBRIDGE, ALBERTA, CANADA

Success nullifies. You then have to do it again, preferably differently.

– Karl Lagerfeld

Preface

The experimental ideas presented herein were collaboratively determined between Ms. Breanne L. Kamenz, Dr. Paul G. Hayes, and Dr. Kevin R. D. Johnson. The presented synthetic research was performed under the supervision of Dr. Paul G. Hayes with assistance from Dr. Kevin R. D. Johnson. The computational research described involved guidance from conversations with Dr. Lesley R. Rutledge and Ms. Cassandra M. Churchill. All novel compounds in the context of this thesis were synthesized and fully characterized by Ms. Breanne L. Kamenz. The lanthanide starting materials $Lu(CH_2SiMe_3)_3(THF)_2$ and $Y(CH_2SiMe_3)_3(THF)_2$ were prepared and purified by Dr. Kevin R. D. Johnson. Single crystal X-ray diffraction experiments and structure refinement were performed by Ms. Breanne L. Kamenz with the assistance of Dr. Kevin R. D. Johnson. The remaining experimental research presented was performed solely by Ms. Breanne L. Kamenz.

Abstract

The synthesis and characterization of a carbazole-based family of *NNN* tridentate pincer ligands and their respective organolanthanide chemistry was explored using both traditional synthetic and computational methodologies. The two modular ancillaries, a bis(phosphinimine)carbazole and a bis(pyrazolyl)carbazole ligand, were systematically developed with the intent of mitigating intramolecular cyclometalative reactivity that had been observed in previous ligand systems. The bis(phosphinimine)carbazole ligand was designed with geometrically constrained phospholane rings, which were incorporated into the ligand in a bid to reduce the propensity of cyclometalation at the PR_2 site. The bis(pyrazolyl)carbazole ancillary explored the incorporation of strongly electron donating pyrazolyl rings into the ligand scaffold, as an alternative donor moiety to phosphinimines. Between the two scaffolds, distinguishable reactivity and stability was apparent upon formation of dialkyl lanthanide complexes. These differences were directly correlated to the unique steric and electronic properties provided by each framework.

Acknowledgements

Thank you to my supervisor, Dr. Paul Hayes, for allowing me to work under your tutelage for the past 5 years. Through your constant guidance and support, I have developed a variety of skills that will certainly be beneficial to my future endeavours. You took a risk on a second year undergraduate student that approached you in the local mall, and I hope it paid off!

My "lab family" of fellow students both within the Hayes group and at the University of Lethbridge has been instrumental to my growth as a researcher and a person. I would like to thank Dr. Hudson Sun for being the "lab dad" and keeping the lab in top form, and Drs. Craig Wheaton and Jamie Ritch for acting like brothers to me. I also had the pleasure of working with a fantastic group of undergraduates that I now consider as lifelong friends, Saif Zahir (a.k.a baby Saif), Majken Villiger, Jackson Knott (a.k.a J-Money), and Brooke MacKay, who always made the lab a much more enjoyable (and entertaining) place to be, and for that I'd like to thank them. Finally, thanks to the three most incredible women I had the honor of becoming friends with during my time in the Wetmore lab, Dr. Lesley Rutledge, Dr. Andrea Millen, and soon to be Dr. Cassandra Churchill. You girls are among the most amazing, kind-hearted, and supportive people I know. Though we have all gone our separate ways in life, modern technology has allowed us to stay as good friends, and for that I am blessed.

The Faculty and staff at the University of Lethbridge have provided tremendous support to me throughout my degree. In particular, I would like to thank my research committee members, Dr. Michael Gerken and Dr. Peter Dibble,

for providing excellent feedback with regards to both my research and program progress, and my external examiner, Dr. David Emslie, for attending my M. Sc. defence. I would also like to thank Dr. Stacey Wetmore for introducing me to computational chemistry, and providing me with the resources necessary to pursue computational modeling of my own systems. I am also extremely grateful for our administrative assistant, Mrs. Susan Hill, for her constant aid and friendship throughout the years.

Throughout my Masters, I had the amazing opportunity to serve as the Program Coordinator of Let's Talk Science. This wonderful opportunity vastly broadened my graduate studies experience to one outside of the lab, and I am extremely proud of all that's been accomplished over the past two years. Of course, none of this would have been possible without an incredible team of faculty and site coordinators, and for that I'd like to thank Dr. Ute Kothe-Wieden, Dr. Ken Vos, Mrs. Helena Danyk, Mr. Wayne Lippa, Jenna Friedt, Kirsten Rosler, and Laura Keffer-Wilkes for all of their support and hard work the past two years.

I would like to deeply thank my wonderful parents, Denny and Sheryl Kamenz, for their continued support throughout the years. My parents have always taught me to be strong, independent, and to work hard for what you want. Without their constant motivation, advice, and a good dose of tough love now and then, I would not have been able to accomplish what I have thus far. For this I am extremely grateful. Thanks to my brother, and the other chemist in our family, Brent. Being the older sibling, you've always indirectly paved the way for my future. Always first to set the bar, you've pushed me to be the best that I can be. This

usually meant beating you, which wasn't easy! I would like to thank my best friend and partner in crime, Amanda Rollag. We've been through thick and thin together since high school, and no one understands me like you do. To my extended family, Vance Johnson, Debbie and David Gaunt, Heather Johnson, and Lisa and Ross Alexander, thank you for your continued support throughout the years. Finally, thank you to my amazing fiancé, Kevin Johnson. You're calming outlook on life and relentless love have been invaluable to me. For that, you are my better half.

Table of Contents

Signature Page ii

Quotation iii

Preface iv

Abstract v

Acknowledgements vi

Table of Contents ix

List of Tables xii

List of Figures xiv

List of Schemes xviii

List of Selected Introduction Compounds xxi

List of New Compounds xxii

List of Symbols and Abbreviations xxiv

Chapter 1 1

1.1 Properties of the Rare Earth Metals 1

1.2 Synthetic Considerations 5

1.3 Evolution of Ancillary Ligand Design for Rare Earth Metals 7

1.3.1 Cyclopentadienyl Ligand 7

1.3.2 Cyclopentadienyl Based Lanthanide Compounds 8

1.3.3 Ancillary Ligand Design 13

1.3.4 β-Diketiminate Scaffolds 14

1.3.5 Imine Containing Pincer Ligands 19

1.3.6 Previous Work 25

1.4 Project Goals 28

Chapter 2 30

2.1 Overview 30

2.2 Introduction to Phosphinimines 31

2.2.1 Phosphinimine-Containing Pincer Ligands 31

2.3 Ligand Design 39

2.3.1 Properties of Phosphinimine Functionalities 39

2.3.2 Structural Features 40

2.4 Ligand Synthesis 43

2.4.1 Preparation of Literature Procedures 43

2.4.2 Phospholane Installation 46

2.4.3 Phosphinimine Formation 49

2.5 Metal Complexation 53

2.5.1 In situ Generation of $L_1^{Pipp}Lu(CH_2SiMe_3)_2$ (**12**) 54

2.5.2 Thermal Decomposition of **12** 55

2.5.3 Kinetic Analysis of Ligand Metalation 57

2.5.4 In situ Synthesis of $L_1^{Pipp}Sc(CH_2SiMe_3)_2$ (**14**) 60
2.5.5 Thermal Decomposition of **14** 61
2.6 Computational Analysis of HL_1^{Pipp} and Associated Metal Complexes 66
2.6.1 Computational Analysis of $L_1^{Pipp}Lu(CH_2SiMe_3)_2$ (**12**) and $L_1^{Pipp}Sc(CH_2SiMe_3)_2$ (**14**) 67
2.7 Conclusions 75
Chapter 3 77
3.1 Overview 77
3.1.1 N-Heterocyclic Containing Ligands 78
3.2 Ligand Design 85
3.2.1 Structural Features 85
3.2.2 Ligand Synthesis 86
3.3 Metal complexation 92
3.3.1 Synthesis of $L_2^{Me}Lu(CH_2SiMe_3)_2$ (**18**) 92
3.3.2 Synthesis of $L_2^{Me}Sc(CH_2SiMe_3)_2$ (**19**) 93
3.3.1 In situ Formation of $L_2^{Me}Y(CH_2SiMe_3)_2$ (**20**) 95
3.4 Computational Analysis of HL_2^{Me} and Associated Metal Complexes 97
3.4.1 Computational Analysis of HL_2^{Me} (**17**) 97
3.4.2 Computational Investigation of **18**, **19**, and **20** 99
3.4.3 Probing Steric Bulk: Investigating Alternative CzPz Ancillaries 104
3.4.4 Metal Complexes of Bulkier CzPz Analogues 107
3.5 Reactivity of CzPzMe Lanthanide Complexes 115
3.5.1 Reactivity of $L_2^{Me}Lu(CH_2SiMe_3)_2$ (**18**) 116
3.5.2 Reactivity of $L_2^{Me}Sc(CH_2SiMe_3)_2$ (**19**) 117
3.6 Conclusions 119
Chapter 4 122
4.1.1 HL_1^{Pipp} Organometallic Chemistry 122
4.1.2 HL_2^{Me} Organometallic Chemistry 124
4.2 Tuning of Existing Ligands 126
4.2.1 HL_1^{Pipp} Modifications 126
4.2.2 HL_2 Modifications 130
4.3 Alternative Ancillary Ligands 131
4.4 Alternative Ligand Synthesis 133
4.4.1 Synthesis of HL_1^{Pipp} 133
4.4.2 Synthesis of HL_2^{Me} 135
4.5 Conclusions 137
Chapter 5 139
5.1 General Procedures 139
5.1.1 Laboratory Equipment and Apparatus 139
5.1.2 Solvents and Purification 140
5.1.3 NMR Spectroscopy 140
5.1.4 Kinetic Analysis 141
5.1.5 Computational Methodology 142
5.1.6 Other Instrumentation and Analysis 146

5.1.7 Materials 147
5.1.8 Preparation of Materials from Modified Procedures 147
Synthesis of $ClP(C_4H_8)$[110] 147
Synthesis of Pyrimidine Azide[161-162] 148
Synthesis of 3,6-dimethylpyrimidine azide[161] 149
5.2 Experimental Procedures Pertaining to Chapter 2 150
5.2.1 Synthesis of Compounds 150
Synthesis of 1,8-bis(phospholano)-3,6-dimethyl-9-^{t}BOC-carbazole (**9**) 150
Synthesis of 1,8-bis(phospholano)-3,6-dimethyl-9-H-carbazole (**10**) 151
Synthesis of HL_1^{Pipp} (**11**) 152
In situ Generation of $(L_1^{Pipp})Lu(CH_2SiMe_3)_2$ (**12**) 153
Decomposition of (**12**) to (**13**) 153
In situ Generation of $(L_1^{Pipp})Sc(CH_2SiMe_3)_2$ (**14**) 154
Decomposition of (**14**) to (**16**) 155
5.3 Experimental Procedures Pertaining to Chapter 3 156
5.3.1 Synthesis of Compounds 156
Synthesis of HL_2^{Me} (**17**) 156
Synthesis of $(L_2^{Me})Lu(CH_2SiMe_3)_2$ (**18**) 157
Synthesis of $(L_2^{Me})Sc(CH_2SiMe_3)_2$ (**19**) 158
In situ Generation of $(L_2^{Me})Y(CH_2SiMe_3)_2$ (**20**) 158
In situ Generation of $(L_2^{Me})Lu(CH_2SiMe_3)(NHMes^*)$ (**21**) 159
In situ Generation of $(L_2^{Me})Sc(NHMes)_2$ (**22**) 160
5.4 Experimental Procedures Pertaining to Chapter 4 161
5.4.1 Synthesis of Compounds 161
Synthesis of $HL_1^{2,4\text{-diMePym}}$ (**23**) 161
In situ Generation of $(L_1^{2,4\text{-diMePym}})Lu(CH_2SiMe_3)_2$ (**24**) 161
Synthesis of 1,8-$(P(Cl/Br)_2)_2$-3,6-dimethyl-9-^{t}BOC-carbazole (**25**) 162
5.5 X-ray Crystallography 163
Specific Crystallographic Refinement Details for **25** 164
References 166

List of Tables

Table 2.1. Selected bond lengths (Å), bond angles (°), and torsion angles (°) for compound ***10****.* 48

Table 2.2. Selected bond lengths (Å), bond angles (°), and torsion angles (°) for compound ***11****.* 53

Table 2.3 ^{1}*H NMR resonances of THF in different chemical environments in benzene-*d_6*.* 55

Table 2.4 k_{obsvd} *and half-lives for the decomposition of* ***12*** *at different temperatures.* 58

Table 2.5 Comparison of ^{1}*H NMR THF resonances in different chemical environments in benzene-*d_6*.* 60

Table 2.6 Select bond lengths (Å) and angles (°) of the computationally and crystallographically determined structure of ***11****.* 66

Table 2.7 Relative energies of the different geometry optimizations for compound ***12****.* 71

Table 2.8 Select bond lengths (Å) and angles (°) of the computationally determined molecular structure of ***12a****.* 71

Table 2.9 Relative energies of the different geometry optimizations of compound ***14****.* 74

Table 2.10 Select bond lengths (Å) and angles (°) of the computationally determined molecular structure of ***14a****.* 75

Table 3.1 Select bond lengths (Å) and angles (°) of HL_2^{Me} *(****17****).* 92

Table 3.2 Select bond lengths (Å) and angles (°) from the geometry optimized structure of H L_2^{Me}*.* 98

Table 3.3 Bond lengths (Å) and angles (°) from the computationally determined molecular structure of ***18****.* 102

Table 3.4 Select bond lengths (Å) and angles (°) of the computationally derived molecular structure of ***19****.* 102

Table 3.5 Select bond lengths (Å) and angles (°) of the computationally derived molecular structure of ***20****.* 103

Table 3.6 Select bond lengths (Å) and angles (°) for the computationally determined structures of CzPz^{i}*Pr, CzPz*^{t}*Bu, and CzPzPh.* 107

Table 3.7 Select bond lengths (Å) and angles (°) for computationally derived CzPz^{i}*Pr lanthanide complexes.* 110

Table 3.8 Select bond lengths (Å) and angles (°) of the computationally determined CzPz^{t}*Bu metal complexes.* 112

Table 3.9 Select bond lengths (Å) and angles (°) of the computationally determined CzPzPh metal complexes. 115

Table 5.1 Basis sets employed for calculations performed on lanthanide containing compounds. Effective core pseudopotentials (ECP) are in brackets. 143

Table 5.2 Summary of X-ray crystallography data collection and structure refinement for compounds ***10***, ***11***, ***17***, *and* ***25*** 165

List of Figures

Figure 1.1 The 7 4f molecular orbitals 4

*Figure 1.2 Generic process for **A** - "ate" complex formation and **B** - intramolecular C–H bond activation (cyclometalation).* 5

Figure 1.3 Synthesis of the cyclopentadienide anion from dicyclopentadiene 8

*Figure 1.4 Example of **A** – sandwich and **B** - bent metallocene complexes of Cp** 10

Figure 1.5 Ansa cyclopentadienyl based scaffold for supporting rare earth metals. 13

Figure 1.6. General structure of nacnac supported organolanthanide compounds. 15

Figure 1.7. Novel family of nacnac supported scandium dialkyl compounds. 16

Figure 1.8 Nacnac supported scandium dialkyl with enhanced steric bulk. 17

Figure 1.9. Nacnac framework with pendant amine donors. 17

Figure 1.10. Tridentate NNN ligand for dialkyl lanthanide compounds. 18

Figure 1.11 Isolable terminal scandium imide 19

Figure 1.12. Mixed anilido-imine framework for supporting rare earth metal compounds. 23

Figure 1.13. Pyridine based mixed anilido-amine ligand scaffold for rare earth metal complexation 24

Figure 1.14. Bis(imine)pyrrolyl scaffold for organolanthanide chemistry. 24

Figure 1.15. First generation carbazole based NNN tridentate phosphinimine pincer ligand 25

Figure 2.1 Generic phosphinimine framework. 32

*Figure 2.2 Bis(phosphinimino)methane ligands, where **i** is a neutral ligand, **ii** is a monoanionic ligand, and **iii** is a dianionic ligand* 32

*Figure 2.3 Bonding motifs of both the **i**) mono- and **ii**) dianionic variations of the bis(phosphinimino)methane ligand* 33

Figure 2.4 PNP backbone pincer ligand for rare earth metal complexation. 36

*Figure 2.5 Imino isomer (**i**) and amino isomer (**ii**) of a mono(phosphinimine) ligand.* 37

Figure 2.6 Mixed phosphinimine-anilido ligand system 38

Figure 2.7 Proposed monoanionic pincer ligand scaffold. 42

*Figure 2.8 Phospholane (**i**) and phosphorane (**ii**).* 43

*Figure 2.9 Thermal ellipsoid plot (50% probability) of bis(phospholane) **10**. All hydrogen atoms, except for H1, have been omitted for clarity.* 47

Figure 2.10 Top view of bis(phospholane) ***10*** *represented with 50% probability ellipsoids. All hydrogen atoms, with the exception of H1, have been omitted for clarity.* *48*

Figure 2.11 Thermal ellipsoid plot (50% probability) of ***11*** *where hydrogen atoms have been omitted for clarity.* *51*

Figure 2.12 Molecular structure of ***11*** *represented with 50% probability ellipsoids. Hydrogen atoms have been omitted for clarity.* *51*

Figure 2.13 Stacked plot of $^{31}P\{^{1}H\}$ NMR spectra following the decomposition of ***12*** *to* ***13*** *at 295.3 K from t = 300 s to t = 10800 s.* *58*

Figure 2.14 First order plots for the decomposition of ***12*** *at temperatures from 273.0 K – 303.0 K.* *59*

Figure 2.15 Eyring plot of the cyclometalation of ***12.*** *59*

Figure 2.16 Stacked plot of the decomposition of ***14*** *followed by $^{31}P\{^{1}H\}$ NMR spectroscopy at 294.2 K.* *62*

Figure 2.17 DEPT–135 NMR spectrum of ***16.*** *63*

Figure 2.18 DEPT–90 NMR spectrum of ***16.*** *64*

Figure 2.19 Computationally optimized structure of ***11*** *using B3WP91/6-31G(d,p).* *67*

Figure 2.20 Molecular representation of $L_1^{Pipp}Lu(CH_2SiMe_3)_2$ ***(12a)*** *with two free THF molecules. H atoms have been omitted for clarity.* *69*

Figure 2.21 Molecular representation of $L_1^{Pipp}Lu(CH_2SiMe_3)_2$ ***(12b)*** *with one coordinated and one free THF molecule. H atoms have been omitted for clarity.* *69*

Figure 2.22 Molecular representation of $L_1^{Pipp}Lu(CH_2SiMe_3)_2$ ***(12c)****, whereby the starting approximation included two coordinated THF molecules. H atoms have been omitted for clarity.* *70*

Figure 2.23 Molecular representation of $L_1^{Pipp}Sc(CH_2SiMe_3)_2$ ***(14a)*** *with two free THF molecules. H atoms have been omitted for clarity.* *72*

Figure 2.24 Molecular representation of $L_1^{Pipp}Sc(CH_2SiMe_3)_2$ ***(14b)*** *with one coordinated and one free THF molecule. H atoms have been omitted for clarity.* *73*

Figure 2.25 Molecular representation of $L_1^{Pipp}Sc(CH_2SiMe_3)_2$ ***(14c)****, whereby the starting approximation included two coordinated THF molecules. H atoms have been omitted for clarity.* *73*

Figure 3.1 Generic pybox ligand scaffold. *79*

Figure 3.2 Pybox supported rare earth dimer. *79*

Figure 3.3 Bis(oxazolinyl)methane ligand ***(A)*** *and monoanionic bis(oxazolinato)methane ligand* ***(B).*** *80*

Figure 3.4 Carbazole based bis(oxazoline) supported lanthanide complexes. 82

Figure 3.5 Generic scorpionate (Tp) ligand..... 83

Figure 3.6 Structure of the di(2-pyrazolyl-aryl)amine ligand. 85

Figure 3.7 Proposed CzPz ligand for organolanthanide chemistry. 86

Figure 3.8 Molecular structure of ligand ***17*** *represented by 50% probability thermal ellipsoids. Hydrogen atoms, excluding H1, have been omitted for clarity*..... 91

Figure 3.9 Molecular representation of HL_2^{Me} *from computational geometry optimization at the B3WP91/6-31G(d,p) level of theory. Hydrogen atoms, excluding* H_1*, have been omitted for clarity.* 98

Figure 3.10 Geometry optimized structure of $L_2^{Me}Lu(CH_2SiMe_3)_2$ *performed at the B3WP91/6-31G(d,p) level of theory.* 100

Figure 3.11 Molecular representation of $L_2^{Me}Sc(CH_2SiMe_3)_2$ *from geometry optimization using B3WP91/6-31G(d,p)*..... 100

Figure 3.12 Molecular representation of $L_2^{Me}Y(CH_2SiMe_3)_2$ *from geometry optimization using B3WP91/6-31G(d,p)*..... 101

Figure 3.13 Computationally calculated molecular structure of $CzPz^iPr$*. Optimization was performed at the B3WP91/6-31G(d,p) level of theory.*..... 105

Figure 3.14 Computationally calculated molecular structure of $CzPz^tBu$*. Optimization was performed at the B3WP91/6-31G(d,p) level of theory.*..... 106

Figure 3.15 Computationally calculated molecular structure of CzPzPh. Optimization was performed at the B3WP91/6-31G(d,p) level of theory...... 106

Figure 3.16 Molecular representation of $CzPz^iPrLu(CH_2SiMe_3)_2$ *from geometry optimization using B3WP91/6-31G(d,p)*..... 108

Figure 3.17 Molecular representation of $CzPz^iPrSc(CH_2SiMe_3)_2$ *from geometry optimization using B3WP91/6-31G(d,p)*..... 108

Figure 3.18 Molecular representation of $CzPz^iPrY(CH_2SiMe_3)_2$ *from geometry optimization using B3WP91/6-31G(d,p)*..... 109

Figure 3.19 Computationally determined structure of $CzPz^tBuLu(CH_2SiMe_3)_2$ *from geometry optimization using B3WP91/6-31G(d,p)*..... 111

Figure 3.20 Computationally determined structure of $CzPz^tBuSc(CH_2SiMe_3)_2$ *from geometry optimization using B3WP91/6-31G(d,p)*..... 111

Figure 3.21 Computationally determined structure of $CzPz^tBuY(CH_2SiMe_3)_2$ *from geometry optimization using B3WP91/6-31G(d,p)*..... 112

Figure 3.22 Molecular structure of $CzPzPhLu(CH_2SiMe_3)_2$ *from geometry optimization using B3WP91/6-31G(d,p)*..... 113

Figure 3.23 Molecular structure of $CzPzPhSc(CH_2SiMe_3)_2$ *from geometry optimization using B3WP91/6-31G(d,p)*..... 114

Figure 3.24 Molecular structure of $CzPzPhY(CH_2SiMe_3)_2$ from geometry optimization using B3WP91/6-31G(d,p) 114

Figure 4.1 Modified HL_1 ligand with pyrimidine N-aryl groups. 127

*Figure 4.2 Proposed family of CzPz ligands of different steric bulk: **A)** ^{i}Pr **B)** ^{t}Bu **C)** Ph.* 131

Figure 4.3 Potential CzIndz ligands. 132

*Figure 4.4 Molecular representation of the bis(dichlorophosphine/bromine) **(25)** at the 50% probability level. Hydrogen atoms, except H_1, have been removed for clarity.* 135

List of Schemes

Scheme 1.1. Proposed synthesis for the formation of organolanthanide complexes.....6

Scheme 1.2 Synthesis of tris(cyclopentadienyl) lanthanide complexes.....8

*Scheme 1.3 Dinitrogen activation (**A**) and alkyne/CO activation (**B**) from Cp* supported Sm^{2+} compounds.....10*

Scheme 1.4 Synthesis of bis(Cp) organolanthanide compounds.....11*

Scheme 1.5. Reaction chemistry of compounds Cp^*_2LnR in C–H bond activation and olefin insertion.....12

Scheme 1.6 Synthesis of β-diketiminate ligand.....14

Scheme 1.7 Intramolecular C–H bond activation in nacnac supported scandium dialkyl complex.....16

Scheme 1.8 Select reactivity of a terminal imido scandium complex.....19

Scheme 1.9. Preparation of imine containing ligands via a Schiff base condensation reaction.....20

Scheme 1.10. Preparation of salicylaldiminato supported lanthanide complexes.....21

Scheme 1.11. Thermal decomposition pathway of rare earth complexes supported by less bulky derivatives of the salicylaldiminato ligand.....21

Scheme 1.12 Metalation of a bulkier salicylaldiminato ligand for supporting rare earth metals.....22

Scheme 1.13 Formation of an yttrium cation via alkyl extraction using $B(C_6F_5)_3$.....23

*Scheme 1.14 Cyclometalative decomposition pathway of a lutetium dialkyl (**1a** and **1b**).....26*

*Scheme 1.15 Reactivity of **4** with Mes^*NH_2.....27*

*Scheme 1.16. Reactivity of **7** with $Lu(CH_2SiMe_3)_3(DMAP)_2$.....28*

Scheme 2.1 Synthetic pathways used in the formation of bis(amido)lanthanide complexes supported by the bis(phosphinimino)methanide ligand.....34

Scheme 2.2 Protonolysis reactivity of NPNPN ligand.....36

Scheme 2.3 Attempted synthesis of rare earth dialkyls from a mixed phosphinimino-amine ligand.....38

Scheme 2.4 Decomposition pathway of phosphinimine-anilido supported lanthanide dialkyl complex.....39

Scheme 2.5 Synthesis of 1-chlorophospholane.....44

*Scheme 2.6 Synthetic pathways for the **A**) methylation and **B**) Friedel-Crafts alkylation of carbazole.....45*

Scheme 2.7 Bromination and protection of 3,6-dimethylcarbazole. 46

Scheme 2.8 Synthesis of bis(phospholane) (**10**). 47

Scheme 2.9 Synthesis of HL_1^{Pipp} (**11**) 50

Scheme 2.10. Synthesis of $L_1^{Pipp}Lu(CH_2SiMe_3)_2$ (**12**). 54

Scheme 2.11. Intramolecular C-H bond activation of $L_1^{Pipp}Lu(CH_2SiMe_3)_2$ (**12**) *to form* **13**. 56

Scheme 2.12 Synthesis of $L_1^{Pipp}Sc(CH_2SiMe_3)_2$ (**14**). 61

Scheme 2.13 Decomposition of **14** *through two sequential intramolecular metalative processes.* 65

Scheme 3.1 Generic silylcyanation of an aldehyde catalyzed by a pybox supported Ln complex. 80

Scheme 3.2 Reactivity of BoxH ligand with tris(alkyl/amido)lanthanide compounds. 81

Scheme 3.3 Hydroamination of aminoalkenes via a Box supported lanthanide catalyst. 81

Scheme 3.4 Synthesis of LnTp complexes via salt metathesis. 84

Scheme 3.5 Preparation of Tp Ln complexes via protonolysis. 84

Scheme 3.6 Synthesis of **17** *using an Ullmann coupling reaction.* 87

Scheme 3.7 Proposed synthetic pathway for the generation of **17** *using an Ullmann coupling reaction.* 89

Scheme 3.8 Synthesis of $L_2^{Me}Lu(CH_2SiMe_3)_2$ (**18**) 92

Scheme 3.9 Formation of **19** *via alkane elimination.* 94

Scheme 3.10 In situ formation of **20**. 95

Scheme 3.11 In situ synthesis of **21**. 116

Scheme 3.12 Scoping reactions of **19** *with various anilines to determine steric bulk requirements.* 118

Scheme 4.1 Proposed synthetic pathway for the formation of a terminal Lu imido complex. 123

Scheme 4.2 Reactivity of **12** *to form the bis(anilido) compound* $L_1^{Pipp}Lu(NHPipp)_2$ 124

Scheme 4.3 Proposed synthetic approach for the formation of a lutetium phosphinidene 125

Scheme 4.4 Synthesis of a lutetium silylene complex from compound **17** 125

Scheme 4.5 Reactivity of bis(diphenylphosphine) pyrimidine ligand. 128

Scheme 4.6 1,5-alkyl migration in a dialkyl lutetium complex. 128

*Scheme 4.7 Reaction of compound **23** with $Lu(CH_2SiMe_3)_2(THF)_2$ to yield the NNNNN bound dialkyl lutetium **24**.* 129

Scheme 4.8 1,3-CH_2SiMe_3 alkyl migration of a terpy supported lutetium dialkyl complex. 130

*Scheme 4.9 Synthesis of 1H-indazole (**D**) and 2H-indazole (**E**).* 132

*Scheme 4.10 Proposed CzIndz**D** synthesis.* 133

*Scheme 4.11 Alternative synthetic approach for the formation of **9**.* 134

Scheme 4.12 Synthesis of 2-fluoro-4-methylphenyl trifluoromethanesulfonate. 136

Scheme 4.13 Alternative synthesis of HL_2. 136

List of Selected Introduction Compounds

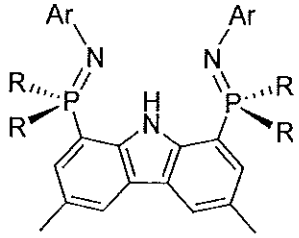

1a (R = Ph; Ar = Ph)
1b (R = Ph; Ar = Pipp)

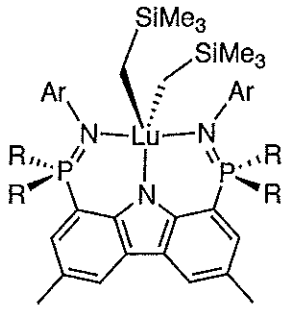

2a (R = Ph; Ar = Ph)
2b (R = Ph; Ar = Pipp)

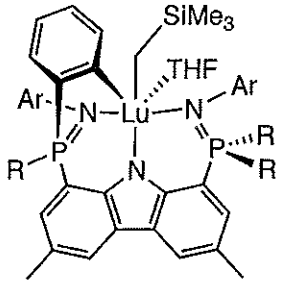

3a (R = Ph; Ar = Ph)
3b (R = Ph; Ar = Pipp)

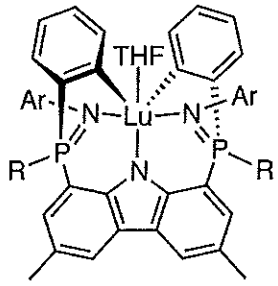

4a (R = Ph; Ar = Ph)
4b (R = Ph; Ar = Pipp)

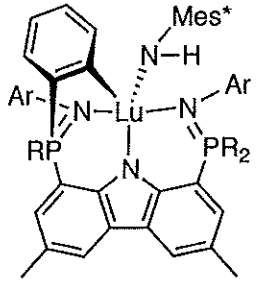

5a (R = Ph; Ar = Ph)
5b (R = Ph; Ar = Pipp)

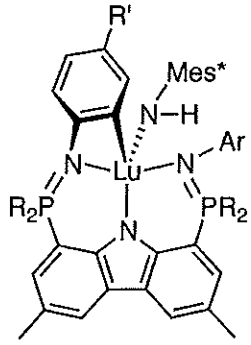

6a (R = Ph; Ar = Ph; R' = H)
6b (R = Ph; Ar = Pipp; R' = Me)

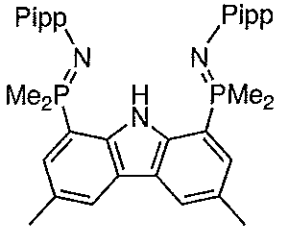

7

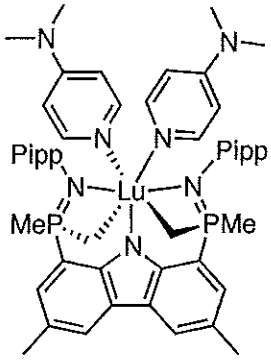

8

List of New Compounds

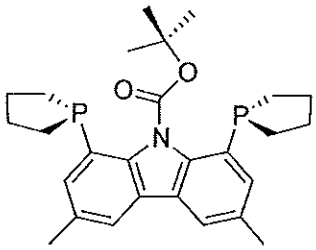

9

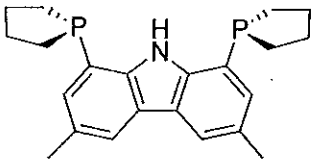

10

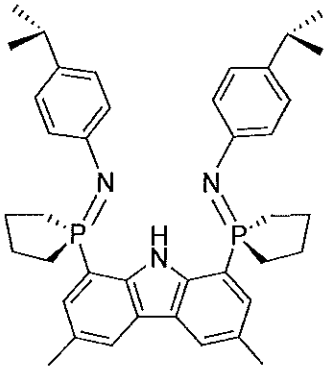

11
HL_1^{Pipp}

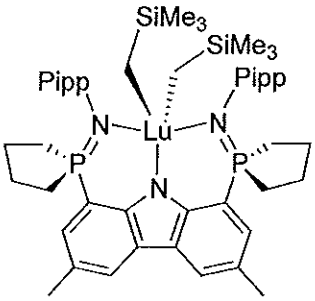

12
$L_1^{Pipp}Lu(CH_2SiMe_3)_2$

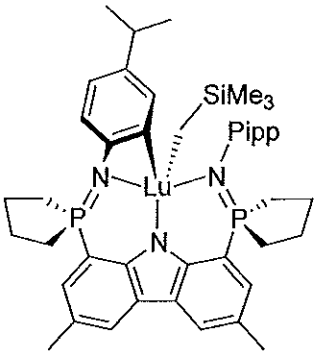

13
$(L_1^{Pipp}\text{-}\kappa^3N, \kappa^1C)Lu(CH_2SiMe_3)$

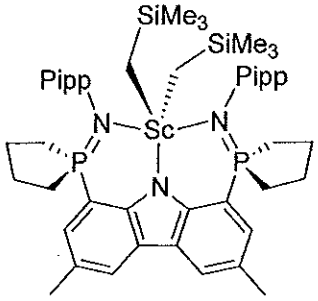

14
$L_1^{Pipp}Sc(CH_2SiMe_3)_2$

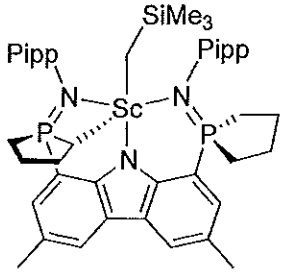

15[i]
$(L_1^{Pipp}\text{-}\kappa^3N, \kappa^1C)Sc(CH_2SiMe_3)$

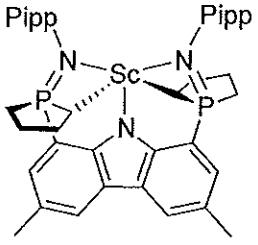

16
$(L_1^{Pipp}\text{-}\kappa^3N, \kappa^2C)Sc$

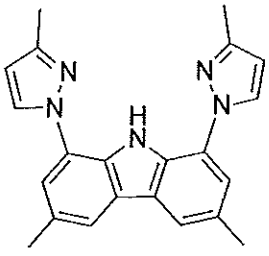

17
HL_2^{Me}

[i] This species is not a fully characterized new compound, but a proposed intermediate.

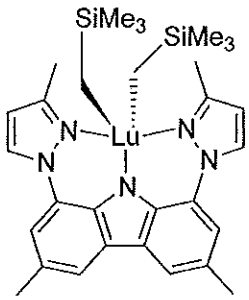

18

$L_2^{Me}Lu(CH_2SiMe_3)_2$

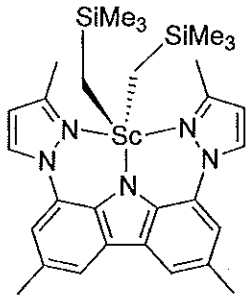

19

$L_2^{Me}Sc(CH_2SiMe_3)_2$

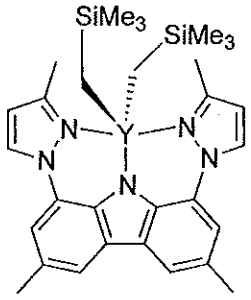

20

$L_2^{Me}Y(CH_2SiMe_3)_2$

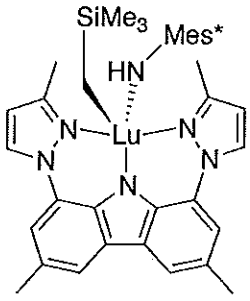

21

$L_2^{Me}Lu(CH_2SiMe_3)(NHMes^*)$

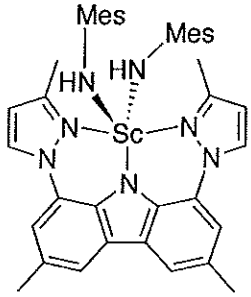

22

$L_2^{Me}Sc(NHMes)_2$

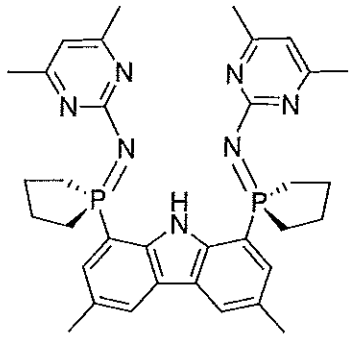

23

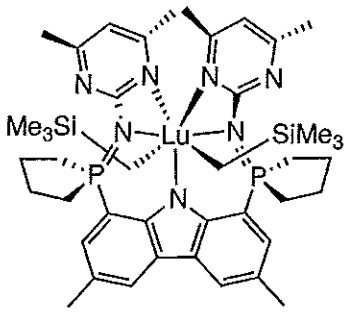

24

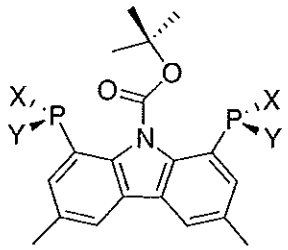

25

X = Cl, Br; Y = Cl, Br

List of Symbols and Abbreviations

a, b, c, α, β, γ	crystallographic unit cell parameters
Å	angstrom, 10^{-10} metres
Anal. Calcd.	analysis calculated
Ar	aryl group
ATR	attenuated total reflectance
BOC	*tert*-butoxycarbonyl
br	broad
C	Celsius
cm^{-1}	reciprocal centimetres
Cp	η^5-cyclopentadienyl (C_5H_5)
Cp*	η^5-pentamethylcyclopentadienyl (C_5Me_5)
Cz	carbazole
d	doublet
D_{calc}	calculated density
DCM	dichloromethane
dd	doublet of doublets
DEPT	distortionless enhancement by polarization transfer
Dipp	2,6-diisopropylphenyl
DMAP	4-dimethylaminopyridine
dt	doublet of triplets
E	element
Et	ethyl
F_c	calculated structure factor
F_o	observed structure factor
FW	formula weight
g	gram(s)
GoF	goodness of fit
h	hour(s) or Planck's constant
Hz	hertz
I	nuclear spin quantum number or intensity
^{i}Pr	isopropyl
IR	infrared
J	Joules
k	rate constant
K	Kelvin
kJ	kilojoules
L	ligand or litre
Ln	lanthanide or group 3 metal
m	multiplet (NMR) or medium (IR)
m-	*meta*
mL	millilitre
M	metal or molar

Me	methyl
Mes	2,4,6-trimethylphenyl
Mes*	2,4,6-tri-*tert*-butylphenyl
mg	milligram(s)
MHz	megahertz
min	minute(s)
mmol	millimole(s)
N	number of measured reflections
NBS	*N*-bromosuccinimide
n-Bu	normal butyl
N_{ind}	number of independent reflections
NHC	*N*-heterocyclic carbene
$^{n}J_{AB}$	coupling constant between nuclei A and B, separated by n bonds
NMR	nuclear magnetic resonance
o-	*ortho*
ov	overlapping
p-	*para*
Ph	phenyl
Pipp	*para*-isopropylphenyl
ppm	parts per million
py	pyridine
Pz	pyrazole
Pym	pyrimidine
R	alkyl group
R_1	conventional agreement index
R^2	coefficient of determination for a linear regression
s	second(s), singlet (NMR) or strong (IR)
sp	septet
t	time or triplet (NMR)
T	temperature
T_1	spin lattice relaxation time
$t_{1/2}$	half-life
t- or *tert*-	tertiary
t-Bu	*tert*-butyl
terpy	2,2′:6′,2″-terpyridine
THF	tetrahydrofuran
TMEDA	*N*,*N*,*N*′,*N*′-tetramethylethylenediamine
Tp	tris(pyrazolyl)borate
Trip	2,4,6-triisopropylphenyl
vw	very weak (IR)
w	weak (IR)
wR_2	weighted agreement index
Z	number of formula units per unit cell
{^{1}H}	proton decoupled
{^{31}P}	phosphorus decoupled
°	degree(s)

δ	chemical shift relative to the reference signal
Δ	heat
$\Delta H^{\ddagger}$	enthalpy of activation
$\Delta S^{\ddagger}$	entropy of activation
$\Delta\rho_{max}$ and $\Delta\rho_{min}$	largest difference map peak and hole in terms of electron density
η^n	hapticity of order n
κ^n	denticity of order n
λ	wavelength
μ	absorption coefficient or bridging
μL	microlitre
ν	frequency
$\nu_{1/2}$	peak width at half height
σ	standard uncertainty

Chapter 1

Introduction

1.1 Properties of the Rare Earth Metals

Rapid interest and advancement in the field of rare earth organometallic chemistry has been observed over the past 20 years. Prior to the 1970's, the rare earth metals[ii] received little recognition in the chemical literature. This void within the literature can be attributed to a lack of chemical understanding from both fundamental and synthetic perspectives.[1] In addition, preconceived notions surrounding organolanthanide chemistry, such as the thought that the lanthanides were unable to form stable organometallic compounds, were extreme limiters for potential research within the field.[2] Postulates surfaced regarding the reduced applications of organolanthanides in areas such as small molecule activation and catalysis simply due to a lack of reported examples. Curiosity regarding specific

[ii] In the context of this thesis, the rare earth metals may be used interchangeably with the term lanthanides, in which both terms encompass the Group 3 metals (Sc, Y, Lu), and the 14 lanthanide metals (La – Yb).

ligand systems, however, sparked much of the current work performed in organolanthanide chemistry.

From a fundamental viewpoint, the 14 lanthanide metal ions exhibit unique electronic and chemical properties that contrast their transition metal analogues, as outlined below.[3]

I. Distinctive [Xe]$4f^n$ electron configuration: The lanthanides have *s*, *p*, *d*, and energetically available *f* orbitals. While the 7 4*f* orbitals, which are presented in Figure 1.1, often contain electrons, they exhibit little to no bonding interactions in the presence of a ligand due to a combination of poor radial extension and shielding by the outer shell 6*s*5*d* orbitals. As a result, electrons in the 4*f* orbitals generally behave like core electrons. A consequence of this phenomenon is that the lanthanides do not obey the 18 electron rule observed for the transition metals, nor do they follow the anticipated 32 electron rule. Electron filling of the orbitals is highly dictated by changes in stability of the 4*f* orbitals with respect to the 5*d* orbitals.

II. Greater than expected decrease in ionic radii with increasing atomic number: This process, commonly referred to as the lanthanide contraction, is attributed to the shielding of the 4*f* orbitals by the 5*s* and 5*p* orbitals. Penetration of the 5*s* and 5*p* orbitals makes them susceptible to the increasing nuclear charge, thus, as the atomic number increases, the orbitals contract. This trend in turn affects the 5d transition metals following the lanthanides, as they exhibit

substantially smaller atomic radii than anticipated based on periodic trends. As such, the 5d transition metals largely resemble their 4d counterparts in size.

III. Predominantly exist in the +3 oxidation state: The ionization energies of the lanthanide metals greatly hinder the ability of the lanthanides to access +5 or +1 oxidation states. In addition, the +2 and +4 oxidation states are rare. This in turn limits certain forms of reactivity often observed in transition metal chemistry, such as the 2 electron processes of oxidative addition and reductive elimination, which have yet to be observed for lanthanide complexes in the +3 oxidation state.

IV. Highly ionic bonding: Preference for the +3 oxidation state results in highly ionic bonding motifs between the lanthanides and a given ligand rather than covalent bonding. For stabilization purposes, "hard" ligands are preferred for bonding. Examples of preferred donor atoms in current lanthanide chemistry include nitrogen and oxygen.

V. Large ionic radii: While the ionic radii decrease with increasing atomic number, the ionic radii across the lanthanide series are still relatively large in comparison to the transition metals. As such, steric saturation of these metals is typically important for stability purposes, which can be addressed by employing sterically encumbering ligands.

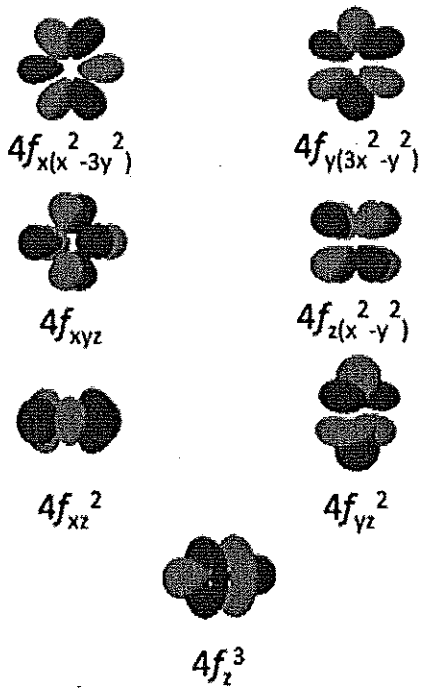

Figure 1.1 The 7 4*f* molecular orbitals.

The group 3 metals scandium (Sc), yttrium (Y), and lutetium (Lu) tend to exhibit properties that parallel that of lanthanum and the rest of the lanthanide series.[4] For this reason, the group 3 metals are often discussed in close association with the 4*f* elements, and as previously stated, are combinedly referred to as the rare earth metals.

While the general properties of the rare earth metals are believed to contribute to novel reactivity and bonding motifs not observed by the transition metals, their inherent nature also results in synthetic challenges associated with the preparation of well-behaved discrete compounds. For instance, organolanthanide compounds are extremely air and moisture sensitive, and as such, require an inert environment for preparation, storage, and investigation of reactivity.[5] This can, in

turn, make processes such as synthesis and purification challenging and time consuming due to limited available techniques. Furthermore, the large ionic radii possessed by the *4f* elements can lead to limited stability and high reactivity. To alleviate these synthetic issues, extreme steric and electronic saturation with respect to the metal centre is often required, and as such, bulky substituents are commonly employed to control/limit the number of open coordination sites. If these constraints are not sufficiently addressed, unwanted side reactions such as dimerization/oligomerization, intramolecular C–H bond activation, "ate" complex formation, and/or Lewis base retention, may occur (Figure 1.2).

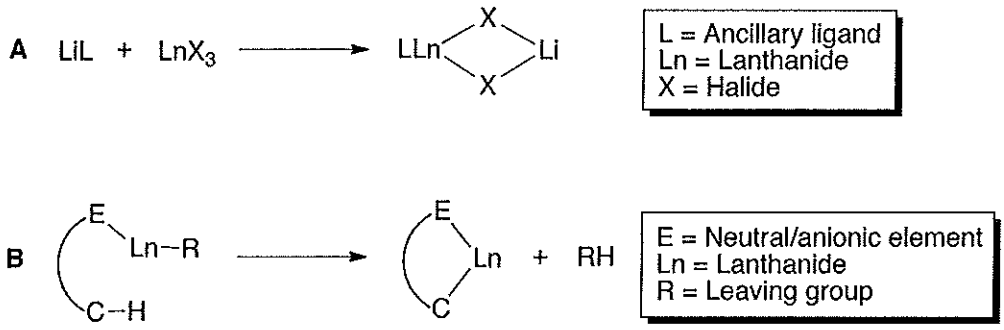

Figure 1.2 Generic process for **A** - "ate" complex formation and **B** - intramolecular C–H bond activation (cyclometalation).

1.2 Synthetic Considerations

Synthesis of organolanthanide starting materials is frequently accomplished *via* salt metathesis pathways (Scheme 1.1), whereby reaction of a metal trihalide source with an appropriate alkyl or amine salt (often in the presence of a donating solvent such as THF or diethyl ether due to solubility limitations) yields the desired

tris(alkyl/amine) complex.[5] Alternatively, direct reaction of lanthanide trihalides with an alkali metal salt of a given ancillary ligand can often afford the ligated lanthanide halide, which can then be further derivatized by reaction with an alkyl or amine salt (Scheme 1.1).[5] The driving force of such reactions is the precipitation of the corresponding insoluble salt, which can usually be separated with ease *via* standard filtration methods. While utilization of Lewis basic solvents is typically important with regards to enhancing the solubility of rare earth metal starting materials, it can often result in formation of the Lewis base adduct of the desired product, which increases the steric and electronic saturation of the metal centre.[5] This saturation also has the potential to limit or change the subsequent chemistry of the metal.

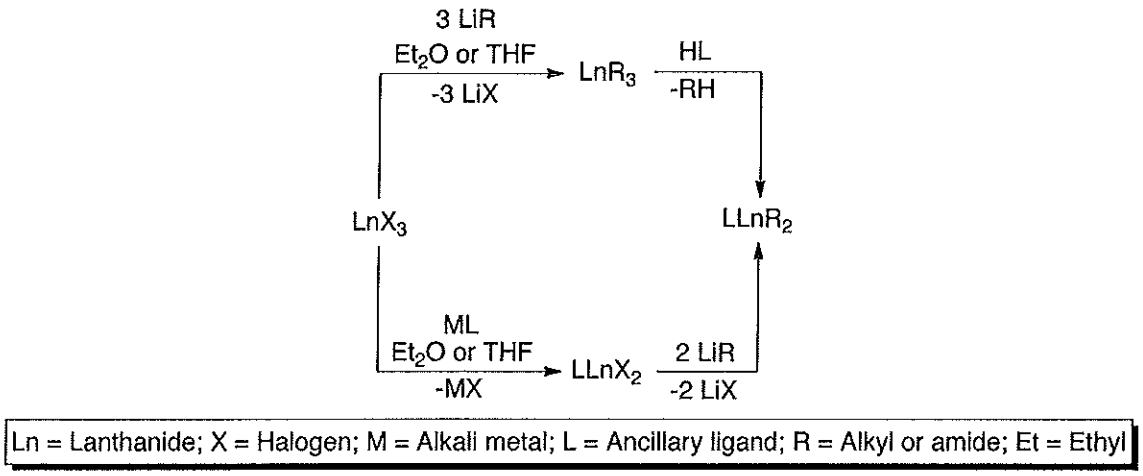

Scheme 1.1. Proposed synthesis for the formation of organolanthanide complexes.

Further reactivity of the subsequent organometallic lanthanide complexes of the form LnR_3 can be achieved through either alkane or amine elimination pathways (Scheme 1.1) in the presence of a protic ancillary ligand. This synthetic method is desirable as it eliminates the potential for "ate" complex formation. Additionally, the

use of alkane or amine elimination routes simplifies the reaction work-up procedures as the resultant alkane or amine byproduct is typically volatile and can be readily removed under dynamic vacuum. However, the thermally sensitive nature of many organolanthanide starting materials where R = alkyl can make handling and isolation quite difficult. This proves especially true for smaller alkyl groups, such as methyl, ethyl, and isopropyl, as they do not provide enough steric saturation to the metal centre. As a result, bulkier alkyl and amine groups are often utilized.[5-6] The use of bulkier tris(alkyl/amine) lanthanide reagents creates limitations with respect to ligand attachment due to restrictions imposed by the binding pocket. If the binding pocket is too small, a facile reaction will not be observed. If too large on the other hand, undesirable intra- or intermolecular side reactions may occur to both electronically and sterically saturate the metal coordination sphere.

1.3 Evolution of Ancillary Ligand Design for Rare Earth Metals

1.3.1 Cyclopentadienyl Ligand

Interest regarding cyclopentadienyl (Cp) ligand systems began in 1954.[7] During this time, a broad survey of the periodic table was conducted to test the limitations and properties of this novel scaffold.[7] In comparison to existing ligands at that time, Cp was desirable in that it was a 6-electron monoanionic donor ligand.[8-9] Additional properties, such as free bond rotation and symmetrical binding motifs simplified processes such as spectral characterization.

While beneficial for metal complexation, the actual synthesis of Cp is not straightforward. Cracking of dicyclopentadiene at elevated temperatures yields monomeric cyclopentadiene. However, without immediate use of the monomer or proper storage (−78 °C), self Diels-Alder reactions occur, generating the dicyclopentadiene starting material. Monomeric cyclopentadiene can be converted into the monoanionic cyclopentadienide *via* deprotonation with various bases (*e.g.* sodium metal) (Figure 1.3).[10]

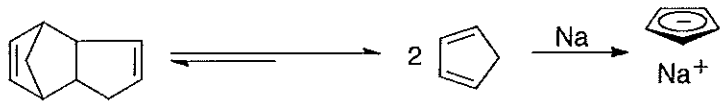

Figure 1.3 Synthesis of the cyclopentadienide anion from dicyclopentadiene.

1.3.2 Cyclopentadienyl Based Lanthanide Compounds

The Cp work performed by Wilkinson and Birmingham in 1954 also included the synthesis and characterization of a series of organometallic lanthanide compounds.[7,11] These complexes, which were the first organometallic lanthanide compounds known, incorporated the use of Cp *via* a salt metathesis reaction between the anhydrous $LnCl_3$ and sodium cyclopentadienide, yielding the base free tris(cyclopentadienyl) lanthanide compounds ($LnCp_3$) (Scheme 1.2).[7,11-12] Structural analysis as well as similar reactivity patterns for all $LnCp_3$ analogues suggested highly ionic bonding and unique reaction chemistry for these lanthanide complexes.

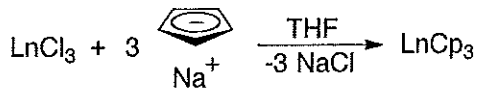

Scheme 1.2 Synthesis of tris(cyclopentadienyl) lanthanide complexes.

The promise of the Cp anion to sufficiently meet the steric and electronic requirements for the formation of thermally stable organolanthanide complexes led to further carbocyclic ligand developments.[13] Most notably, small, methodical derivatizations at the Cp rings allowed for both steric and electronic fine tuning of the metal centre, yielding novel bonding motifs and reactivity. The development of the pentamethylcyclopentadienyl (Cp*) ligand, which became popularized in the 1980's,[14-16] is one such example, whereby both trivalent and the more elusive divalent organometallic rare earth compounds were discovered. Accessibility of the divalent state for the lanthanides Eu, Yb, and Sm, is achievable with Cp* due to the presence of additional bulk imparted by the methyl moieties, allowing for a high degree of steric saturation at the metal centre.[17] Most notable is the samarium derivative, $Cp^*_2Sm(THF)_2$, which was the first reported divalent organolanthanide compound.[18] The unsolvated analogue, Cp^*_2Sm, was synthesized shortly thereafter, and exhibits a unique bent metallocene geometry which contrasts the parallel Cp rings in transition metal sandwich complexes (Figure 1.4).[19] The synthesis of both of these divalent compounds allowed for development of novel reactivity parallel to reductive transformations observed with the transition metals. Of particular interest, bonding and subsequent reactivity of the aforementioned Sm^{2+} compounds with unsaturated substrates including dinitrogen, alkynes, and CO, to name only a few, was achieved (Scheme 1.3).[17]

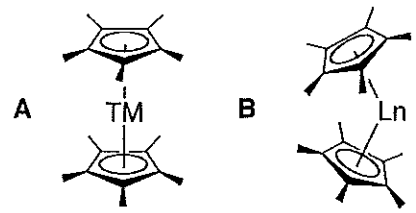

Figure 1.4 Example of **A** – sandwich and **B** - bent metallocene complexes of Cp*.

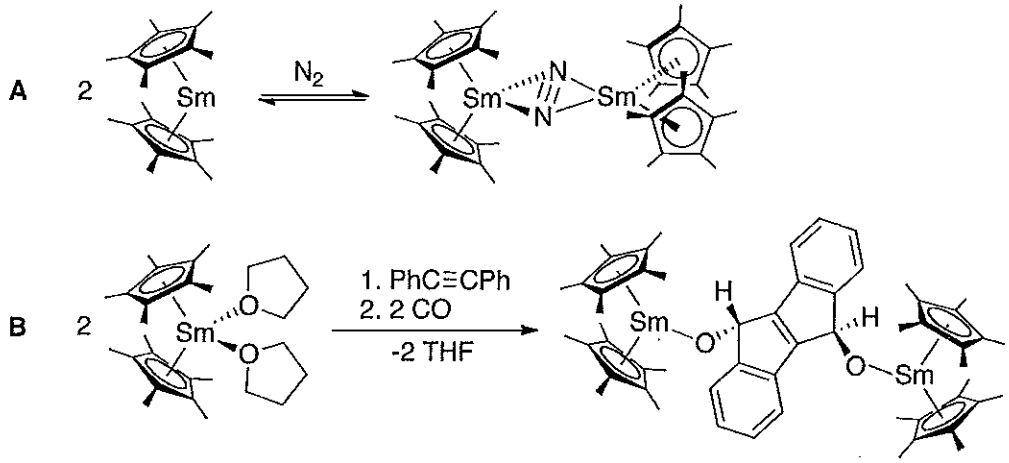

Scheme 1.3 Dinitrogen activation (**A**) and alkyne/CO activation (**B**) from Cp* supported Sm^{2+} compounds.

In contrast to the Cp analogues, trivalent derivatives of homoleptic lanthanide Cp* complexes could only be attained for the larger lanthanide metals, where Ln = Sm, La, Ce, Pr, Nd, and Gd.[20] This limitation is attributed to increased steric congestion about the metal centre imposed by the methyl groups of the Cp* rings. While remarkable chemistry arose from the homoleptic trivalent analogues, exploration of areas such as small molecule activation was restricted by the excessive ligand bulk, which generally prevents access to the metal centre. This dilemma paved the way for interest in heteroleptic systems of the form Cp^*_2LnR (R

= H, alkyl, aryl), where Cp* serves as an ancillary ligand. Notably, these compounds are also accessible for the smaller rare earth metals (Ln = Sc, Lu), which is of particular interest with regard to the scope of this thesis. The inclusion of Ln–R groups allows for rich reaction chemistry at the metal centre, while also providing a facile method to alter both the metal's steric and electronic environments. Incorporation of R functionalities also signified the departure from solely π-bonded lanthanide compounds to those including σ-bonds, priming the field for a wealth of new chemistry and reactivity.

Access to bis(pentamethylcyclopentadienyl) alkyl, aryl and hydride rare earth compounds can be readily achieved by reacting Cp^*_2LnX as its THF adduct with an appropriate organolithium or Grignard reagent (Scheme 1.4).

$$Cp^*_2LnX(THF) + MR \xrightarrow[-MX]{THF} [Cp^*_2LnR]_n$$

Ln = Sc, Lu; X = Halogen; M = Alkali or alkaline earth metal; R = H, alkyl, aryl; n = 1 - 2

Scheme 1.4 Synthesis of bis(Cp*) organolanthanide compounds.

Subsequent reactivity of the above compounds tends to be dictated by the size of the reagent due to the wedge opening imposed by the Cp* moieties. This has largely restricted reactivity to that involving small molecules, but has allowed for exploration of remarkable transformations including C–H bond activation, and olefin insertion, which are highly relevant to catalytic processes such as olefin polymerization (Scheme 1.5).[21-22]

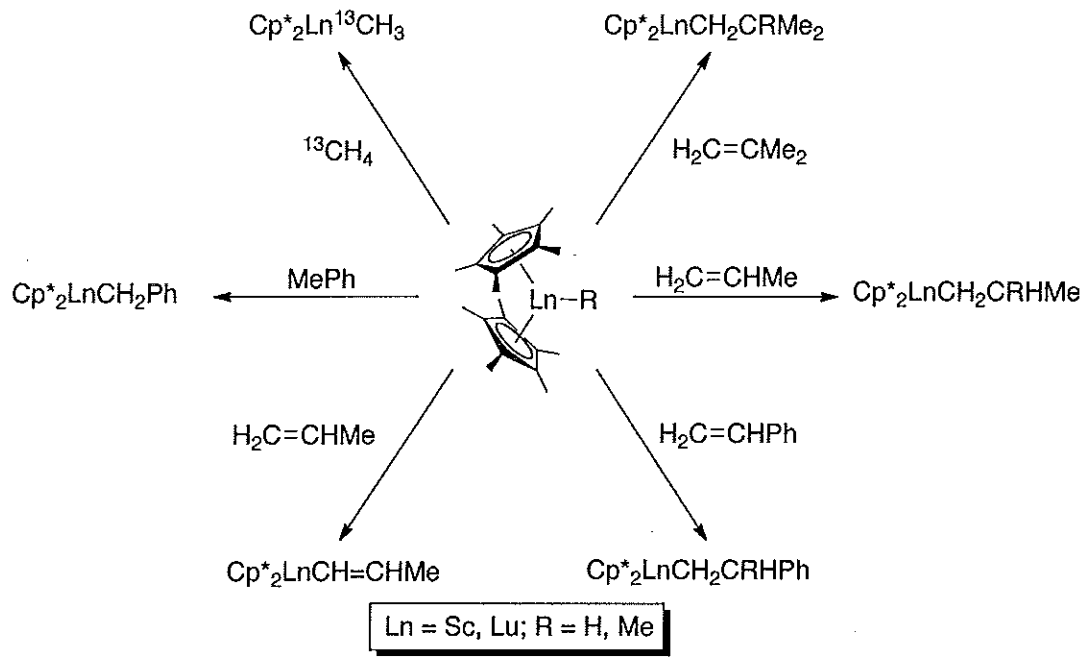

Scheme 1.5. Reaction chemistry of compounds Cp^*_2LnR in C–H bond activation and olefin insertion.

To influence the wedge opening and create a more reactive metal centre, the use of "tied back" carbocyclic scaffolds, which had been applied to both transition metal and actinide chemistry, became of interest (Figure 1.5).[23-24] These frameworks, which often utilize a $SiMe_2$ tether as a bridge between the carbocyclic rings (i.e. *ansa*-Cp), have been shown to reduce the Cp-metal-Cp angle by 10–20°, thus reducing steric congestion at the lanthanide centre.[25] This reduction allows for the incorporation of bulkier groups (*e.g.* $-CH(SiMe_3)_2$, $-NH(SiMe_3)_2$, C_3H_5) at the metal centre which was not possible in bis(Cp*) systems. In addition, enhanced reactivity and selectivity was observed with respect to olefin insertion.[25]

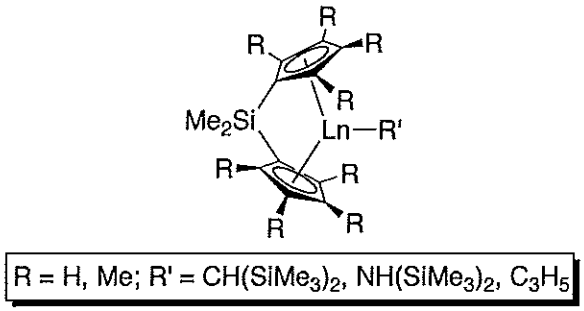

Figure 1.5 Ansa cyclopentadienyl based scaffold for supporting rare earth metals.

1.3.3 Ancillary Ligand Design

While Cp systems and derivatives thereof were influential with regard to establishing the synthesis and reactivity of stable organolanthanide compounds, limitations regarding their steric and electronic tunability hindered the possibility of future discoveries. In addition, numerous patents pertaining to Cp systems, their respective metal complexes, and subsequent reactivity makes them expensive to utilize for future synthetic exploration. These dilemmas motivated organolanthanide chemists to pursue alternative non-carbocyclic scaffolds. Most importantly, designer ancillary ligands that incorporated electron-donating atoms such as N, P or O were of interest for stabilizing the relatively electron poor rare earth centres. Additionally, scaffolds that could be readily sterically and electronically tuned to accommodate the requirements of the lanthanide metals became popularized. While the evolution of ancillary ligand design is important with respect to this thesis, it is an area that has been extensively reviewed over the years; as such, this is not intended to be a comprehensive review of organolanthanide

ligand design, but a rather judicious selection of examples most relevant to the contents of this thesis will be presented.

1.3.4 β-Diketiminate Scaffolds

One of the most influential ligands in the realm of organometallic transition metal and rare earth chemistry is the β-diketiminate, or "nacnac" ligand, which is the imine analogue of the isoelectronic "acac" ligand scaffold.[26] This framework can be modified at either the group bound to nitrogen (R'), or at the ligand backbone itself (R) by selecting the appropriate aniline and β-diketone during synthesis (Scheme 1.6).[27-29] The overall versatility of nacnac, in combination with strong nitrogen donors, has led to its popular use in rare earth chemistry. This has in turn yielded an array of nacnac supported organolanthanide compounds (Figure 1.6).[30-32] Significantly, many of these compounds have exhibited important catalytic activity for transformations such as ring-opening polymerization (ROP) of lactide and ε-caprolactone, and ethylene polymerization.[33-34]

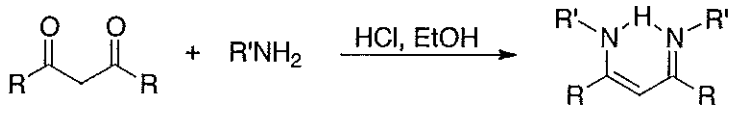

R = Ar = Alkyl or aryl; R' = Ph, Dipp, 3,5-^{t}BuC$_6$H$_3$, 2,4,6-^{i}PrC$_6$H$_2$, 3,5-(2,4,6-^{i}PrC$_6$H$_2$)C$_6$H$_3$

Scheme 1.6 Synthesis of β-diketiminate ligand.

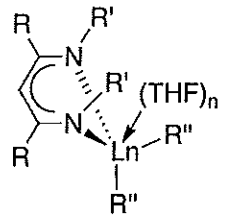

Ln = Lanthanide metal; R = Me, ^{t}Bu; R' = Aryl, Alkyl Ph; R'' = Alkyl; n = 0, 1

Figure 1.6. General structure of nacnac supported organolanthanide compounds.

Examples of thermally stable dialkyls that contain the highly desirable and reactive Ln–C bond are still scarce within the literature. This is due to unwanted decomposition pathways such as dimerization, ligand redistribution, C–H bond activation, and elimination reactions that have plagued the search for robust dialkyl nacnac lanthanide complexes.[35] To overcome these unwanted forms of reactivity, steric and electronic tuning at the nitrogen moiety in the nacnac framework has been performed, with the end goal being to enhance the saturation of the rare earth metal centre. Work performed by the Piers group incorporated bulky 2,6-diisopropylphenyl (Dipp) functionalities at nitrogen, yielding the first thermally stable organoscandium compounds (Figure 1.7).[36] In relation to the ligand backbone, the scandium atom lies out of the NCCCN plane significantly in each case (~0.815 – 1.25 Å), a feature that is attributed to the bulk of the Dipp groups interacting with the alkyl substituents on the metal centre.[36] To alleviate this steric clash, the Dipp moieties tend to be rotated such that they are almost perpendicular to the plane made by the ligand backbone. However, even with the rotation of the Dipp groups and deviation of the metal centre with respect to the NCCCN plane of the ligand backbone, intramolecular C–H bond activation of an isopropyl CH_3 of the

Dipp group and scandium occurs in solution to afford the asymmetric singly metalated species and loss of alkane (Scheme 1.7).[36] This process is most facile for derivatives that employ ^{t}Bu groups on the nacnac backbone as they enhance the steric congestion at scandium, a trait that is believed to promote metalation.[37]

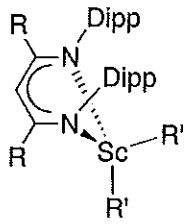

R = Me, ^{t}Bu; R' = CH_3, CH_2CH_3, CH_2Ph, $CH_2C(CH_3)_3$, $CH_2Si(CH_3)_3$

Figure 1.7. Novel family of nacnac supported scandium dialkyl compounds.

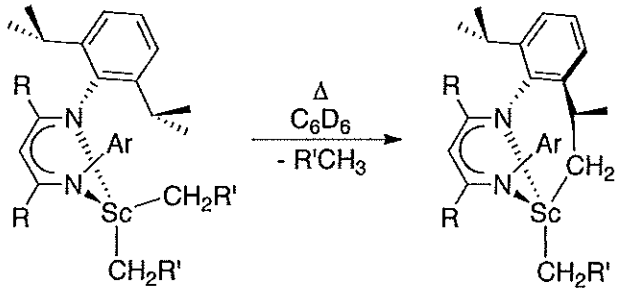

R = Me, ^{t}Bu; R' = H, $SiMe_3$; Ar = Dipp

Scheme 1.7 Intramolecular C–H bond activation in nacnac supported scandium dialkyl complex.

Utilizing the principle of "remote steric bulk", the inclusion of substantially bulkier aryl moieties lacking *ortho* substituents on nacnac was also investigated as a means of mitigating metalation.[38] The resulting ligand frameworks, whereby substitution of the N-aryl moieties is at the *meta* position, were found to support a series of scandium dialkyl compounds obtained *via* alkane metathesis (Figure 1.8).

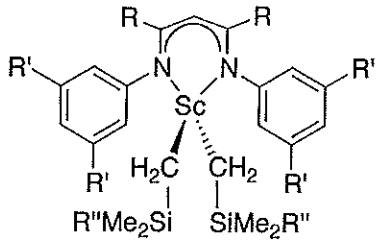

R = Me; R' = ^{t}Bu, 2,4,6-^{i}PrC$_6$H$_2$; R" = Me, Ph

Figure 1.8 Nacnac supported scandium dialkyl with enhanced steric bulk.

In an attempt to reduce unwanted metalation due to excessive steric bulk, Roesky *et al.* incorporated nitrogen-containing pendant amino groups that offer enhanced donor abilities to the metal centre (Figure 1.9).[39] While this scaffold readily supports base-free lanthanide dihalides,[39-40] only one dialkyl example, (nacnac)Tb(CH_2SiMe_3)$_2$, has been reported.[41]

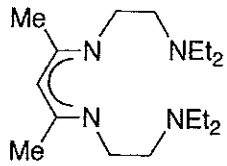

Figure 1.9. Nacnac framework with pendant amine donors.

Integrating ideas from both the Piers and Roesky groups, Chen *et al.* developed a hybrid nacnac ligand containing both the Dipp and nitrogen-containing pendant amine functionalities (Figure 1.10).[42] Providing the best of both worlds with regard to steric and electronic properties, this *NNN* tridentate ligand has been successfully used to synthesize an array of thermally stable dialkyl lanthanide complexes. High activity with respect to polymerization of ε-caprolactone was also noted, and is directly dependent on the length of the diethylamino tether.[42]

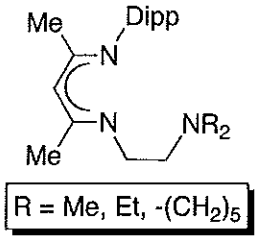

Figure 1.10. Tridentate *NNN* ligand for dialkyl lanthanide compounds.

Offering the proper steric and electronic environment for the rare earth metals with the aforementioned ligand system prompted the discovery of the first isolable and fully characterized terminal scandium imido complex (Figure 1.11).[43] The imide functionality, which is common in both transition metal and actinide chemistry, has shown promise in a variety of chemical transformations, such as hydroamination catalysis and group transfer reactions.[44] Due to the unique properties of the lanthanides presented in Section 1.1, it is anticipated that enhanced or unique reactivity of the imide bond may be realized. Elusiveness of Ln=N bonds within the literature, however, has hindered such developments. This disparity is believed to be attributed to poor orbital overlap,[45] a theory supported by previous attempts to form Ln=N bonds, which either yielded bimetallic-bridged compounds, multimetallic clusters, or compounds susceptible to C–H bond activation.[46] To date, the terminal scandium imido compounds prepared by Chen have demonstrated cycloaddition of small molecules, activation of elemental selenium and silanes, and imine catalyzed hydrosilation.[47-49]

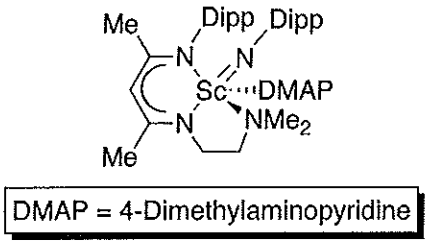

Figure 1.11 Isolable terminal scandium imide.

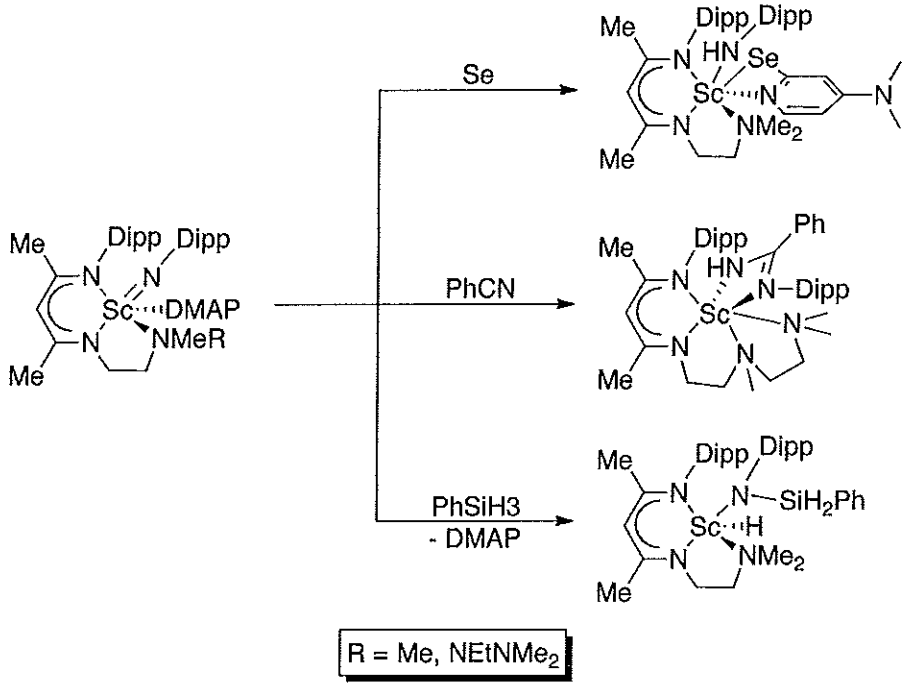

Scheme 1.8 Select reactivity of a terminal imido scandium complex.

1.3.5 Imine Containing Pincer Ligands

The hard, Lewis acidic properties of the lanthanides make hard donor atoms ideal candidates with regard to ligand design. Nitrogen is of particular interest as it can serve as either a charged or neutral donor towards a given metal centre. Previous work with transition metals has demonstrated that nitrogen donors in the

form of imines have been beneficial for promoting unique forms of reactivity. From a synthetic standpoint, the imine functionality is ideal as it can be readily installed on aromatic frameworks using a straightforward condensation reaction between an amine and an aryl-substituted ketone (Scheme 1.9). In addition, steric and electronic manipulations at the N–R site can be readily achieved by the appropriate choice of amine. In particular, anilines are of interest, as they are readily available and offer ease of tunability. The above properties suggested imines would be suitable candidates for organolanthanide chemistry.

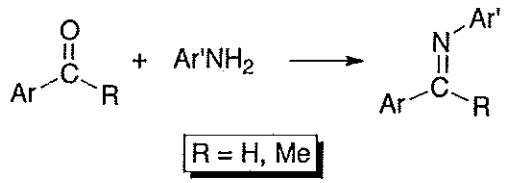

Scheme 1.9. Preparation of imine containing ligands *via* a Schiff base condensation reaction.

Another ligand of interest is the mixed NO donor salicylaldiminato scaffold originally utilized by Grubbs *et al.* for developing nickel-based catalysts for olefin polymerization (Scheme 1.10).[50] This asymmetric framework offers steric protection of the metal centre by employing sterically encumbering aromatic functionalities, in addition to the bulky *tert*-butyl moieties, which occupy the same plane as the ligand.[51-53] Reaction of two equivalents of the salicylaldiminato ligand with the desired lanthanide trialkyl generated the bis(ligand) lanthanide alkyl complexes (Scheme 1.10), where retention of THF is dependent on the steric demands of the ligand and size of the metal ion.[51-53] Careful modification of the reaction conditions allowed for isolation of the mono-ligand dialkyl organoyttrium

complex; however, these compounds are prone to ligand redistribution at elevated temperature, thus forming the bis(ligand) derivatives once more.[53]

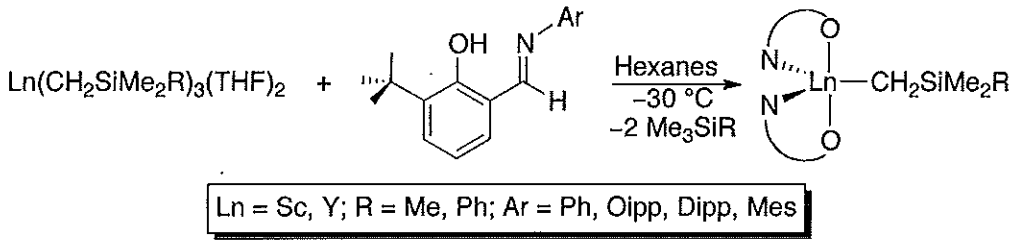

Scheme 1.10. Preparation of salicylaldiminato supported lanthanide complexes.

While thermally stable up to 60 °C, at elevated temperatures decomposition of the scandium and yttrium metal complexes occurs over a period of 3 days. Clean conversion of the bis(ligand) monoalkyl to the decomposition product (Ar = Ph, 2-$^{i}PrC_6H_4$ (Oipp)) occurs by rapid migration of the $-CH_2SiMe_2R$ moiety to the aldimine carbon (Scheme 1.11).[51] In contrast, bulkier analogues whereby Ar = Dipp and Mes have an intermediate C–H bond activation step, followed by the migration of the newly formed Ln–C bond to the aldimine, yielding either a 5 (Mes) or 6 (Dipp) membered ring (Scheme 1.12).[51-53] The resulting yttrium containing compounds where Ar = Dipp further decompose to an intractable mixture of products.[52-53]

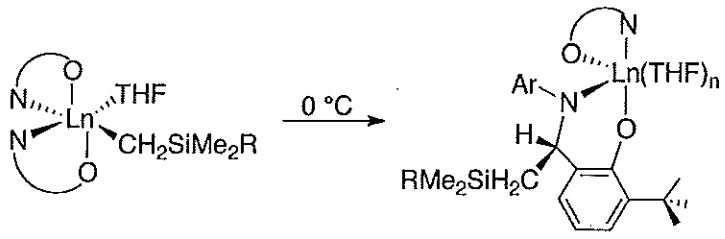

Scheme 1.11. Thermal decomposition pathway of rare earth complexes supported by less bulky derivatives of the salicylaldiminato ligand.

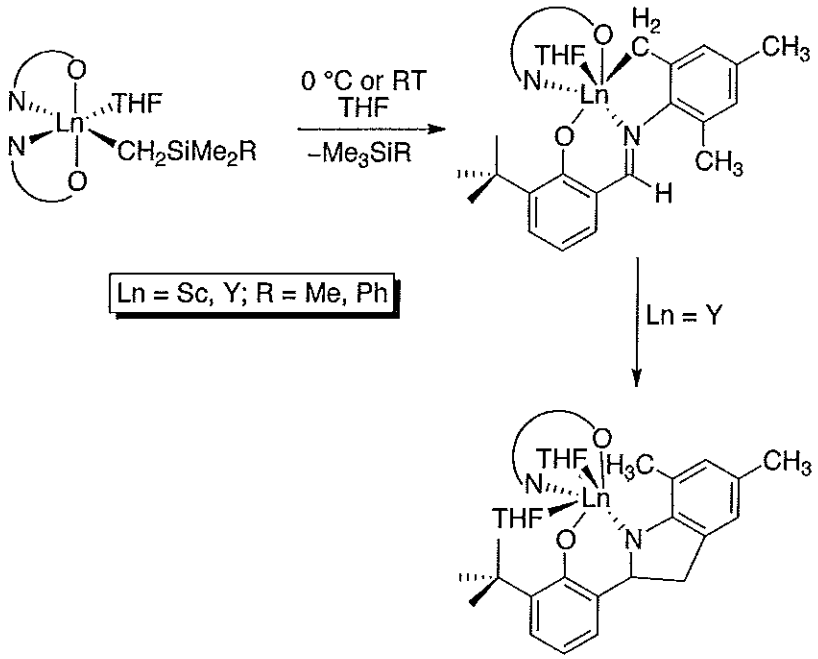

Scheme 1.12 Metalation of a bulkier salicylaldiminato ligand for supporting rare earth metals.

Decomposition of the above compounds is potentially attributed to a lack of sufficient electronic and steric saturation at the metal centre. To address this issue, similar ligand subsets that incorporate two bulky nitrogen-containing functionalities on a given aromatic group have been investigated.

Combining features from both the nacnac and salicylaldiminato frameworks led to the development of the novel monoanionic anilido-imine ligand (Figure 1.12).[54] Formation of an yttrium dialkyl compound can be achieved *via* two sequential salt metathesis reactions.[54] Retention of one THF molecule is observed both spectroscopically and through single-crystal X-ray diffraction, and is believed to enhance the thermal stability of the yttrium dialkyl as decomposition of the desired product does not occur at ambient conditions.[54] In addition, the presence of THF aids in stabilizing the yttrium cation which can be formed *via* the extraction of a

$-CH_2SiMe_2Ph$ group by $B(C_6F_5)_3$ (Scheme 1.13).[54] This cationic yttrium species exhibits indefinite stability when stored under an inert atmosphere at −20 °C, which is rare in comparison to other cationic organoyttrium compounds.[54-56]

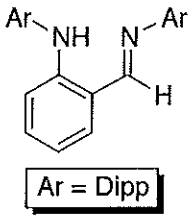

Figure 1.12. Mixed anilido-imine framework for supporting rare earth metal compounds.

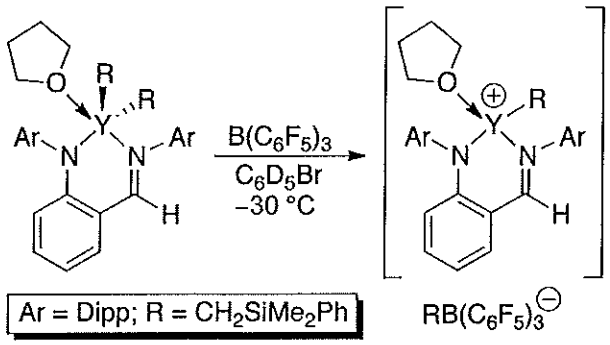

Scheme 1.13 Formation of an yttrium cation *via* alkyl extraction using $B(C_6F_5)_3$.

In addition to the benzylic anilido-imine scaffold, the pyridine-based analogue has also been synthesized (Figure 1.13).[57] This monoanionic tridentate pincer ligand offers a larger chelate angle compared to the benzene-based example, and is able to support an array of dialkyl scandium, lutetium, and yttrium compounds.[57-58] The increase in chelate angle appears to decrease the overall thermal stability of the resulting organometallic rare earth compounds, with the scandium and yttrium dialkyl congeners decomposing faster than the lutetium product, albeit all under ambient conditions.[58] In lieu of decomposition, the resulting dialkyl rare earth complexes are stable enough to probe potential catalytic

activity. Formation of the cationic rare earth species in the presence of borate-based cocatalysts yielded moderate ethylene polymerization activity.[57-58] This polymerization process is highly dependent on temperature, co-catalyst, and rare earth metal employed, where Sc containing compounds had greater activity than the heavier analogues.[58]

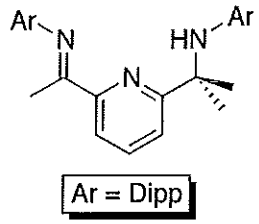

Figure 1.13. Pyridine based mixed anilido-amine ligand scaffold for rare earth metal complexation.

Originally used for transition metal chemistry,[59] bis(imine) pyrrolyl ligands (Figure 1.14) received attention for their potential to support rare earth compounds in the early 2000's.[60] With a high degree of tunability on both sides of the NNN tridentate pincer ligand, and enhanced electronic donation due to the presence of two imine groups, these ligands appeared to be ideal candidates for organometallic rare earth compounds. While a variety of stable dihalide rare earth complexes have indeed been synthesized with this ligand subset,[61-62] only one diamido example is known,[60] and no dialkyl examples are present in the literature.[63]

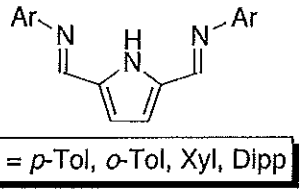

Figure 1.14. Bis(imine)pyrrolyl scaffold for organolanthanide chemistry.

1.3.6 Previous Work

Incorporating the concept of electron-donating nitrogen functionalities, the Hayes group developed a carbazole-based bis(phosphinimine) pincer ligand (Figure 1.15) for supporting organometallic rare earth metal complexes.[64] Advantages of this scaffold include modularity at both the phosphorus and nitrogen atoms of the phosphinimine moiety, allowing for simplified steric and electronic tuning with respect to the metal centre. In addition, the chemically robust phosphinimine functionality provides a diagnostic ^{31}P NMR shift for characterization purposes. Finally, the rigidity of the carbazole backbone aids in dictating the coordination geometry about the metal centre, ultimately limiting fluxional behaviour and hindering possible decomposition pathways.

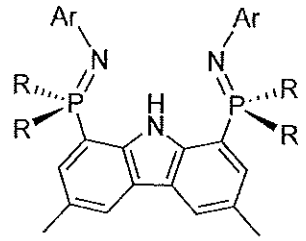

R	Ar	Compound
Ph	Ph	**1a**
Ph	Pipp (*p*-isopropylphenyl)	**1b**
Me	Pipp	**7**

Figure 1.15. First generation carbazole based *NNN* tridentate phosphinimine pincer ligand.

Lutetium dialkyl complexes were prepared by the alkane elimination reaction of $Lu(CH_2SiMe_3)_3(THF)_2$ with proteo ligands **1a** and **1b**. Notably, rapid thermal decomposition was observed at temperatures above 0 °C, whereby the metal undergoes two sequential intramolecular *ortho*-metalative alkane elimination reactions with the ligand P-phenyl rings. The final products of this transformation were determined to be the doubly cyclometalated species in which the ligand is

coordinated to the metal in a κ^5 bonding mode via three nitrogen atoms and two *ortho*-metalated P-phenyl rings (Scheme 1.14). The kinetic parameters of this intramolecular process were extensively studied using variable temperature NMR spectroscopy, whereby the activation parameters ($\Delta H^{\ddagger}$ = 80.5 kJ·mol^{-1} and $\Delta S^{\ddagger}$ = –34.5 J·K^{-1}·mol^{-1}) were determined to compliment previous examples involving intramolecular cyclometalation.[36,64-66]

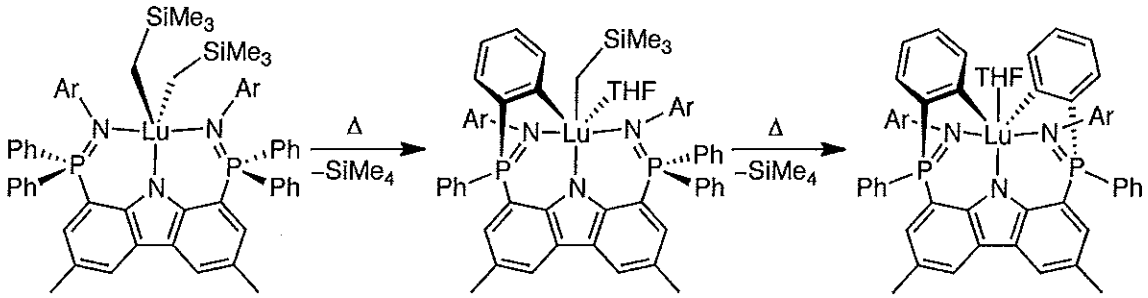

2 **3** **4**

Scheme 1.14 Cyclometalative decomposition pathway of a lutetium dialkyl (**1a** and **1b**).

The resulting Lu–aryl bonds were found to be moderately reactive as the doubly cyclometalated complexes could undergo acid-base reactions with protic reagents such as the iodide delivery reagent [Et_3NH]I and various anilines. For instance, reaction of **4** with one equivalent of 2,4,6-tri-*tert*-butylaniline, liberates one of the P-phenyl rings with generation of the mono(anilido) derivative **5** that still possesses one cyclometalated P-phenyl ring (Scheme 1.15). Interestingly, this mono(anilide) **5** was found to be susceptible to a thermally induced intramolecular rearrangement to a different structural isomer (**6**). This unusual transformation occurred via a metalation exchange reaction whereby intramolecular C–H bond

activation at the *ortho* position of the N-aryl ring occurs with concomitant metalacycle ring-opening of the cyclometalated P-phenyl ring.[67]

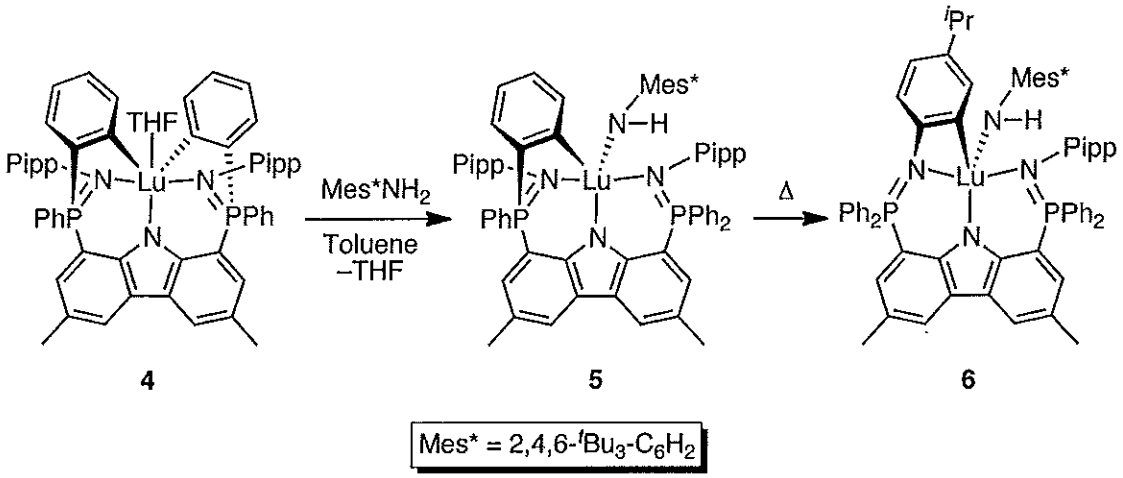

Scheme 1.15 Reactivity of **4** with Mes^*NH_2.

In attempts to circumvent unwanted metalative reactivity, functional groups with reduced peripheral steric bulk at the phosphorus atoms were considered. Of particular interest, the inclusion of dimethylphosphine moieties was examined (**7**).[68] Additional benefits of this functionality include improved overall ligand solubility in aliphatic solvents, as well as diagnostic $^2J_{HP}$ NMR coupling. However, upon reacting the proteo ligand **7** with $Lu(CH_2SiMe_3)_3(DMAP)_2$, the desired dialkyl was not obtained. Instead, the doubly metalated compound **8**, which formed with loss of two equivalents of tetramethylsilane, was observed spectroscopically (Scheme 1.16).[68] This cyclometalative process is believed to have similar activation parameters to the diphenylphosphine analogue, though it has yet to be studied in detail.[68]

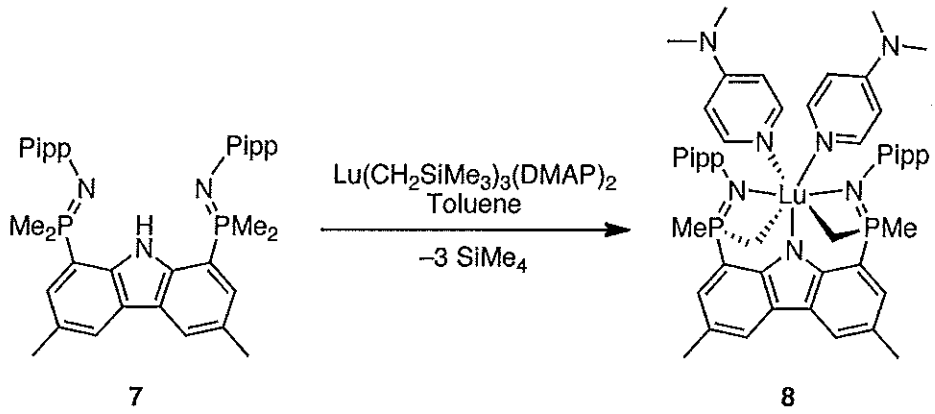

7 8

Scheme 1.16. Reactivity of **7** with $Lu(CH_2SiMe_3)_3(DMAP)_2$.

1.4 Project Goals

The reactivity of discrete, well-behaved organolanthanide compounds has the potential to rival that of current transition metal complexes due to their unique chemical and electronic properties described at the beginning of this chapter. Attaining these unprecedented states of reactivity, however, is highly dependent on providing the proper steric and electronic environment to the rare earth metal centre. Manipulation of both the steric and electronic properties can be readily achieved synthetically through the field of ligand design. As previously noted, many ancillaries have been methodically synthesized and their respective reactivity with the lanthanide metals extensively examined. In many examples, attempts to synthesize dialkyl rare earth compounds resulted in unwanted decomposition pathways, such as rearrangement and intramolecular C–H bond activation.

These combined efforts, in addition to many others not presented in the context of this thesis, have aided in the advancement of ligand design for rare earth

chemistry. Utilizing this knowledge, the intent of the work in this thesis was to design new, metalation-resistant frameworks for stabilizing rare earth metal compounds, and subsequently explore their small molecule reaction chemistry. Thus far, two carbazole-based monoanionic *NNN* scaffolds have been employed for the purposes of supporting organolanthanide compounds, with a focus on Sc and Lu. Each ligand subset exhibits a varying degree of modularity to meet the demands of rare earth chemistry. The first, which is presented in Chapter 2, is a continued effort within the Hayes lab of employing phosphinimine-containing pincer ligands for organolanthanide chemistry, where steric and electronic tuning was considered at the phosphorus atoms in an attempt to prevent the previously observed cyclometalative reactivity. The second ligand family, discussed in Chapter 3 within this thesis, aims at providing greater geometric rigidity with respect to the metal centre, while still maintaining sufficient steric protection and electron donation. In addition to the synthetic aspects of both ligands and their respective metal complexes, computational models will be presented as a complement to experimental results. At the beginning of each chapter, an overview of similar ligand systems will be presented to further familiarize the reader with the concepts pertinent to this body of work.

Chapter 2

Development and reactivity of bis(phosphinimine) pincer ligands containing constrained phosphines

2.1 Overview

Previous work within the Hayes lab has explored the development of a novel family of carbazole-based bis(phosphinimine) ancillaries that offer varying steric and electronic properties. It was found, however, that rare earth alkyl complexes of these scaffolds were prone to decomposition *via* intramolecular cyclometalative C–H bond activation.[69] As a complement to this previous work, a new carbazole-based bis(phosphinimine) pincer ligand has been devised, with the intent of developing an ancillary that is resistant to the process of intramolecular cyclometalation. This new scaffold integrates a novel geometrically constrained 5-membered phospholane ring into the ligand phosphinimine functionality. This geometric constraint was intended to add rigidity to the groups bound to phosphorus and thus, help to reduce the propensity of the ligand to undergo intramolecular cyclometalation reactivity at this

site. Furthermore, it was expected that incorporation of a phospholane ring into the ligand design would give a final ancillary with improved electron-donation abilities, relative to the previously reported iterations that contained phenyl rings bound to phosphorus. For these reasons, the new bis(phosphinimine) ligand presented in this chapter was anticipated to serve as an ideal candidate for supporting stable organolanthanide complexes.

2.2 Introduction to Phosphinimines

Presented below is a select sampling of phosphinimine ligands that have been instrumental to the development of rare earth organometallic chemistry. This review is not intended to be comprehensive, but to provide a sufficient background regarding phosphinimine ligands with different steric and electronic properties, and their subsequent reactivity with respect to organolanthanide compounds.

2.2.1 Phosphinimine-Containing Pincer Ligands

The introduction of phosphinimines as ligands for use in organometallic chemistry occurred in the late 1990's. Pivotal work reported by Stephan *et al.* demonstrated that simple phosphinimine systems exhibit steric and electronic properties similar to that of Cp when coordinated to titanium, while additionally offering higher degrees of tunability (Figure 2.1).[70] This concept was further applied to rare earth compounds, whereby a phosphoraniminato ligand ($[NPR_3]^-$) afforded Ln–N triple bond compounds with bonding motifs comparable to that seen with Cp,

as both ligands bear a single formal negative charge.[71] The above findings were exploited with respect to ligand design, in particular with regard to organo rare earth chemistry, leading to the development of a series of ligand subsets containing phosphinimine functionalities.

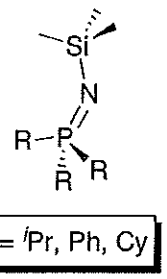

Figure 2.1 Generic phosphinimine framework.

Amalgamation of the β-diketimine scaffold and phosphinimine functionality led to the development of a class of bis(phosphinimino)methane ligands (Figure 2.2). While this ligand family has proven useful in both main group and transition metal chemistry, more recent work has explored the realm of rare earth metal complexation.[72-74] Notably, this scaffold has the unique ability to serve as either a neutral, monoanionic or dianionic ligand (Figure 2.2).[75-78]

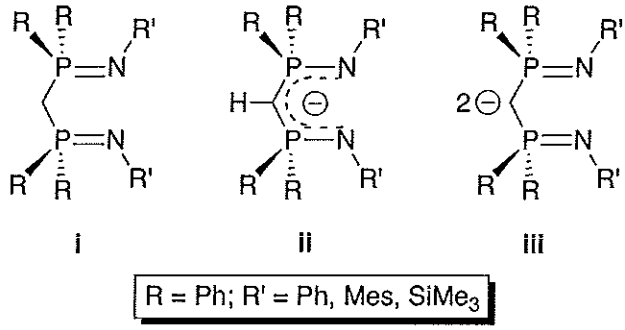

Figure 2.2 Bis(phosphinimino)methane ligands, where **i** is a neutral ligand, **ii** is a monoanionic ligand, and **iii** is a dianionic ligand.

In the presence of an appropriate base, deprotonation of the methylene backbone yields the monoanionic bis(phosphinimino)methanide ligand, whereby the resulting methine carbon can weakly coordinate to the metal centre, yielding a tridentate ligand that adopts a pseudo-boat shape conformation upon complexation (Figure 2.3, **i**). Alternatively, two sequential deprotonations yields the dianionic bis(phosphinimino)methanediide, in which the coordinating carbon exhibits carbene like chemistry in the presence of an appropriate metal, resulting in compounds containing M=C bonding motifs (Figure 2.3, **ii**).

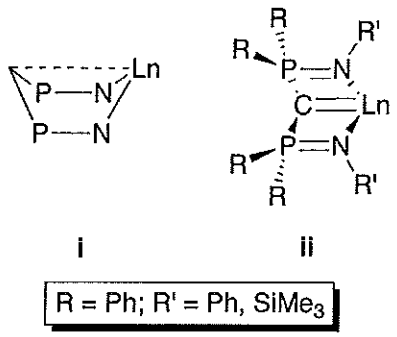

Figure 2.3 Bonding motifs of both the **i**) mono- and **ii**) dianionic variations of the bis(phosphinimino)methane ligand.

Bis(phosphinimino)methanide ligands had previously been popularized in transition metal chemistry for their catalytic cyclization potential.[73-74] It was not until the early 2000's, however, that their prospective rare earth chemistry was explored.[72-74] From a synthetic standpoint, the formation of lanthanide complexes supported by the bis(phosphinimino)methanide framework is achievable through three separate routes (Scheme 2.1), with the direct amine elimination pathway generally affording the highest synthetic yields.[79-80] Subsequent reactivity of the resultant bis(amido) lanthanide complexes indicate potential for catalysis in areas

such as hydrosilation, hydrosilation/hydroamination, and hydroamination/cyclization in relatively high yields. [79,81] In contrast, the dihalide lanthanide analogues supported by the monoanionic backbone were not found to be active catalysts, unless further functionalized to a bis(amido) complex.[82]

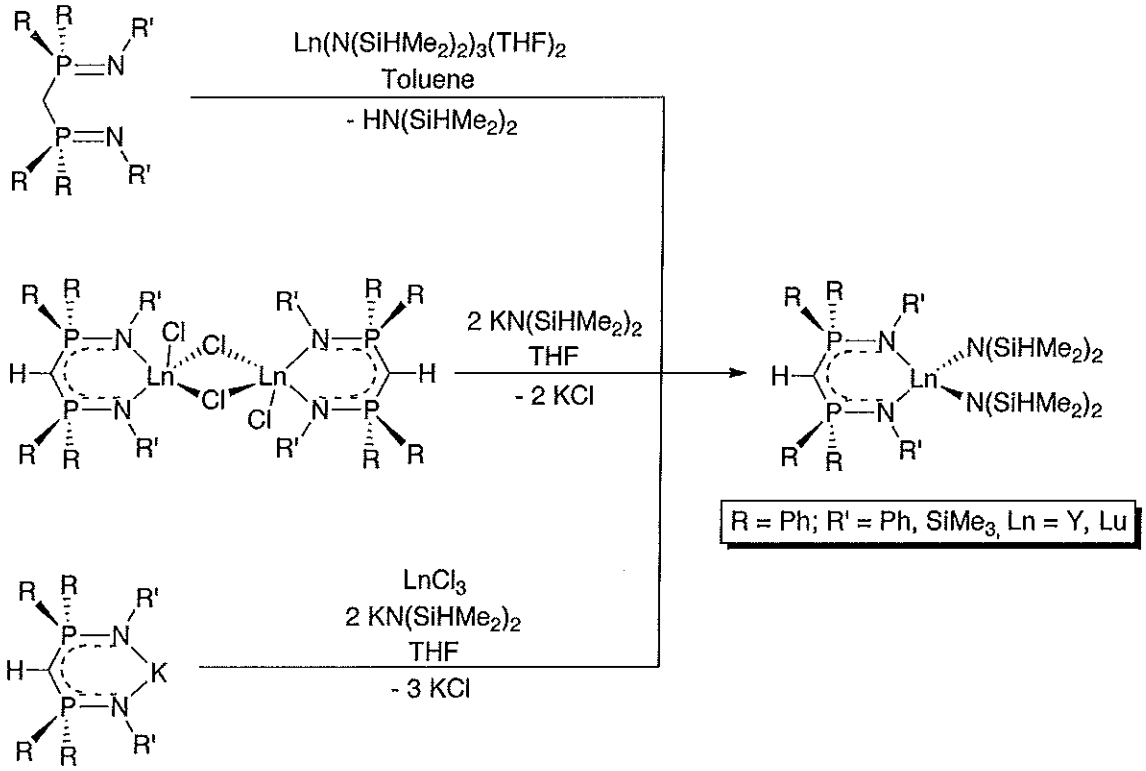

Scheme 2.1 Synthetic pathways used in the formation of bis(amido)lanthanide complexes supported by the bis(phosphinimino)methanide ligand.

While carbene complexes of transition metals are quite prevalent, and are integral with respect to chemical transformations such as olefin metathesis, Wittig reactions, and Fischer-Tropsch processes,[83] analogous carbene lanthanide compounds have been scarce in the literature until the past decade.[73] This paucity is attributed to energy discrepancies between the orbitals involved in bonding, yielding unstable and highly polarized bonding motifs. Providing the proper steric

and electronic environment within a ligand framework, however, can aid in enhancing the stability of the Ln=C bond. In particular, the bis(phosphinimino)methandiide has been influential in the discovery and development of lanthanide carbenes, with the first example being a samarium species reported in the year 2000.[84] Since then, additional lanthanide carbenes (Y, Er, Nd, and La) have been discovered.[85-88] While the bonding of carbenes is classically described as either Fischer- or Schrock-type in transition metal complexes, lanthanide carbenes are different in that the polarity of the Ln=C bond causes the electron density to reside primarily on the carbon atom. Therefore, it is more appropriate to refer to such functionalities as geminal dianions, though the term lanthanide carbene and alkylidene are used interchangeably in the literature and thus will be used in such context in this thesis.[89] Reactivity studies of the resulting Ln=C compounds have been conducted, and include, but are not limited to, insertions (*e.g.* migratory, nitriles), bond activation (CO, CF, CH), and bond formation (CC, CO).[90-94]

More recently, modifications to the bis(phosphinimino)methanide PCP scaffold were explored by replacing the methylene carbon with nitrogen, generating a PNP framework (Figure 2.4).[95] The proteo form of these bis(aryl) phosphazene compounds can be readily tuned at the *N*-aryl positions, allowing for steric and electronic control at the metal centre of a complex. All ligand variations reacted readily *via* alkane elimination with tris(alkyl) rare earth reagents, yielding well-behaved and solvent-free dialkyl compounds coordinated in an *NNN* tridentate fashion (Scheme 2.2). The Ln–CH_2SiMe$_3$ and Ln–CH_2SiMe_3 resonances appear as

singlets in the ^{1}H NMR spectra, suggesting fluxional behaviour on the NMR timescale in solution.

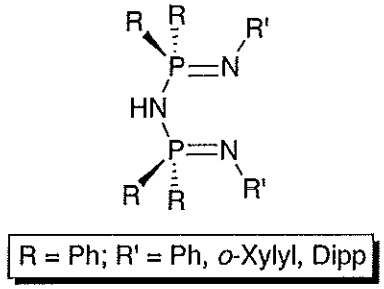

Figure 2.4 PNP backbone pincer ligand for rare earth metal complexation.

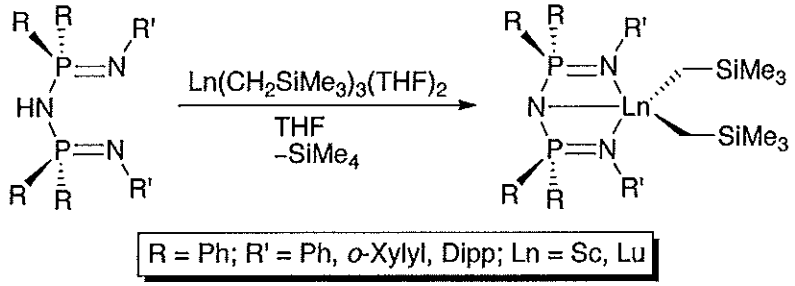

Scheme 2.2 Protonolysis reactivity of NPNPN ligand.

The ability of the resulting dialkyl compounds to mediate alkene polymerization was tested using a variety of olefins (*e.g.* isoprene and butadiene), but no activity was observed.[95]

Mono(phosphinimine) ligands have also been frequently used in organolanthanide chemistry.[96-98] In particular, derivatives of mixed phosphinimine-amine ligands have been of interest. One such example involves the incorporation of a single phosphine moiety into the nacnac framework (Figure 2.5).[99] This scaffold was appealing as it was expected to lower the electron density surrounding the rare earth metal centre while increasing overall steric congestion, ultimately yielding

organolanthanide complexes with enhanced thermal stability while maintaining their reactivity for various catalytic applications.[100-101] However, the phosphinimine-amine ligand can exist in two isomeric forms; the imino and amino tautomers (**i** and **ii**, respectively), whereby the imino tautomer is dominant.[99-101] This tautomerization results in additional synthetic difficulties, as protonolysis reactions can only occur with the amino tautomer. To alleviate this issue, a small excess of the organolanthanide starting material is required to enhance consumption of the amine ligand, allowing for facile formation of the desired dialkyl. Preparation of both the scandium and yttrium compounds was achieved, in which isolation revealed a solvent free scandium dialkyl, and the singly metalated yttrium complex (Scheme 2.3).[100-101] This difference in complex stability is attributed to the size of the ionic radii of the respective metals. In the +3 oxidation state, yttrium possesses a substantially larger ionic radius than scandium (0.900 Å vs. 0.745 Å, respectively),[102] and as such, resides farther outside of the binding pocket, resulting in reduced steric pressure. This lack of steric hindrance at the metal centre makes it more susceptible to cyclometalation.

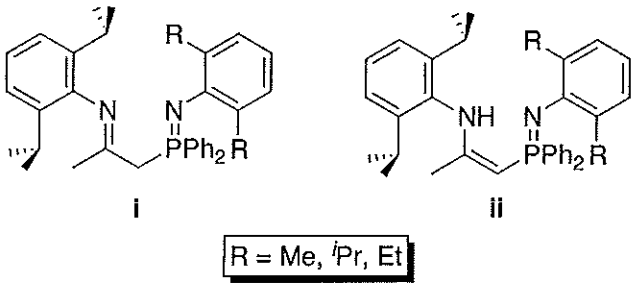

Figure 2.5 Imino isomer (**i**) and amino isomer (**ii**) of a mono(phosphinimine) ligand.

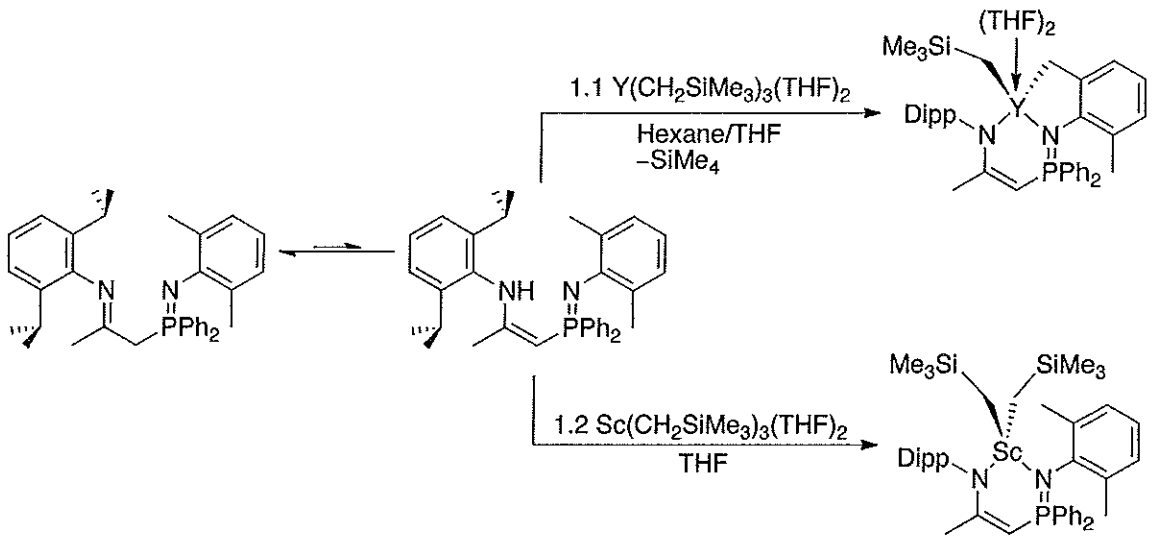

Scheme 2.3 Attempted synthesis of rare earth dialkyls from a mixed phosphinimino-amine ligand.

Systems similar to the scandium dialkyl have shown that a lack of solvent coordination can result in more reactive complexes.[103] Indeed, this was observed with the Lewis base free scandium dialkyl complex, where in the absence of an initiator, ethylene was successfully polymerized under ambient temperature conditions.

Bulkier mixed phosphinimine-anilido scaffolds have also been reported. Following the introduction of the aryl based phosphinimine-anilido ligand (Figure 2.6) into organotransition metal chemistry,[104] Cui and Piers utilized this promising framework for organolanthanide purposes.

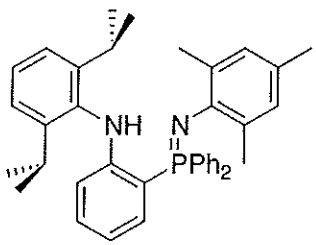

Figure 2.6 Mixed phosphinimine-anilido ligand system.

The resulting lanthanide dialkyl complexes proved to be susceptible to degradation *via* intramolecular cyclometalative C–H bond activation between the metal centre and *P*-phenyl ring (Scheme 2.4).[105]

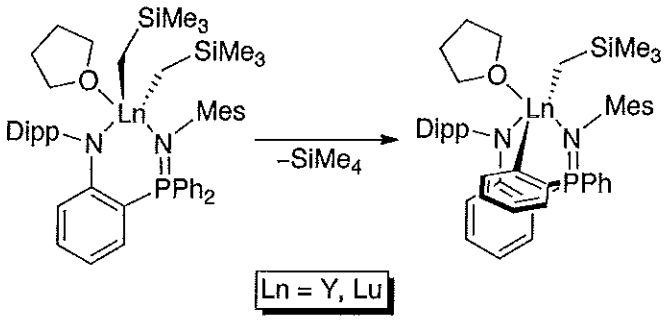

Scheme 2.4 Decomposition pathway of phosphinimine-anilido supported lanthanide dialkyl complex.

To mitigate this metalative behavior, a reduction in steric bulk was pursued. Replacement of the P-phenyl moieties with P-Me groups was explored, but upon formation of the scandium dialkyl, thermolysis *via* C-H bond activation of the methyl functionality occurs.[106]

2.3 Ligand Design

2.3.1 Properties of Phosphinimine Functionalities

As evident from the preceding literature overview, the organometallic chemistry of lanthanide metal complexes bearing phosphinimine-containing ligands has received a high degree of attention as of late. This may be in part due to their similarities, as well as differences, when compared to the highly influential imine based scaffolds. From an electronics standpoint, phosphinimines and imines exhibit

similar σ-donor properties, as determined by both synthetic and computational studies.[107-108] While these findings determined phosphinimines to be comparatively poorer π-acceptors, such a trait is negligible with respect to lanthanide chemistry, as the poor radial extension of the 4*f* orbitals severely hinders any participation of π-donation from the metal to the ligand.

Enhanced chemical robustness of the phosphinimine functionality in comparison to imines is of great appeal from a synthetic standpoint. Whereas the carbon-nitrogen double bond in imines is susceptible to nucleophilic attack at the carbon atom,[31] thus often preventing the formation of a desired organometallic species, the phosphorus-nitrogen double bond of phosphinimines are generally resistant to such reactivity.

An additional feature of phosphinimine moieties is that they offer electronic and steric tunability at both the phosphorus and nitrogen atoms. This allows for greater fine-tuning with respect to the metal centre; conversely, the diversity of imine ligands is solely dictated by the groups bound to nitrogen. Steric shielding of the metal centre can also be enhanced by phosphinimines, aiding in the prevention of unwanted side reactions.[109] Incorporation of phosphorus also introduces a useful characterization handle for NMR spectroscopy, as the ^{31}P nucleus is 100% abundant and $I = ½$.

2.3.2 Structural Features

When designing a novel ancillary ligand for organolanthanide chemistry, one must consider both the stability and potential reactivity of the desired complex.

From a stability perspective, providing a highly tunable steric and electronic framework is ideal for generating readily isolable organometallic rare earth compounds, as exemplified by previous literature examples. Therefore, including modularity at both the nitrogen and phosphorus atoms within the phosphinimine functionality allows for greater control of both steric and electronic saturation of the metal centre. This modularity is also advantageous from a reactivity perspective, as accessibility to the metal centre can be altered depending upon the requirements of a specific chemical transformation. Such capacity for fine-tuning should also aid in mitigating unwanted forms of reactivity, including Lewis base retention, ate complex formation, and ligand redistribution.[31]

In addition to a tunable framework, the overall charge of a ligand is important with regard to reaction chemistry. To assist in tight binding to the metal centre, a ligand that bears either a monoanionic or dianionic charge is desirable, resulting in either two or one metal valences available for additional reaction chemistry, respectively, as the lanthanides exist predominantly in the +3 oxidation state.

Incorporating the above properties and benefits previously stated regarding phosphinimines, a family of monoanionic 3,6-dimethylcarbazole-based pincer ligands bearing two flanking phosphinimine functionalities was developed in the Hayes laboratory for use in organo rare earth chemistry (Figure 2.7).

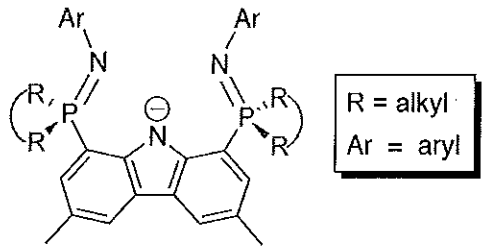

Figure 2.7 Proposed monoanionic pincer ligand scaffold.

Carbazole, which is a commercially available chemical feedstock, was employed as the ligand backbone because it imparts rigidity to the ligand framework, thus helping to alleviate undesirable reactivity between the supporting ligand and the metal centre. The acidic NH can also be readily deprotonated in the presence of either an appropriate base or tris(alkyl) lanthanide starting material; thus, this ligand serves as a versatile monoanionic ancillary ligand that offers ideal pincer geometry.

As presented in preceding examples, the phosphinimine groups at the 1 and 8 positions of carbazole can be readily tuned at both the N and P positions, allowing for a diverse ligand family. Based on previous work within the Hayes lab where *P*-phenyl metalation was observed,[64] constrained cyclic phosphine groups were chosen for this body of work. Such groups were anticipated to reduce the steric bulk at the metal centre, while geometrically hindering the probability of metalation from occurring due to their constrained nature. In particular, a fully saturated 5-membered phosphine ring, herein referred to as phospholane, was investigated (Figure 2.8, **i**). Similar phosphines, in particular the 6-membered fully saturated phosphorane ring (Figure 2.8, **ii**), were also considered. Ultimately, it was decided that a lack of geometric control due to conformational fluxionality of the

phosphorane ring presented itself as a more likely candidate for metalation, thus it was not pursued in this thesis.

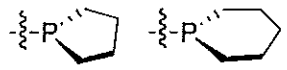

i ii

Figure 2.8 Phospholane (**i**) and phosphorane (**ii**).

The phospholane required for this work can be prepared *via* modified literature procedures (Section 2.3.1),[110] and was anticipated to provide sufficient steric saturation at the metal centre while enhancing electronic donation in comparison to previous scaffolds developed in the Hayes lab.

This generation of ligand maintained N-bound aryl groups as they provide sufficient steric bulk at the metal centre and can be readily installed under Staudinger reaction conditions. Furthermore, a variety of aryl azides can be readily synthesized according to literature procedures, allowing for facile fine-tuning of the ligand framework.

2.4 Ligand Synthesis

2.4.1 Preparation of Literature Procedures

For the purpose of installing phospholane rings into the ligand framework, the reagent 1-chlorophospholane was targeted. As previously mentioned, the 1-chlorophospholane can be synthesized from literature procedures, with the complete synthesis outlined in Scheme 2.5.[110] *In situ* formation of the Grignard

reagent 1,4-bis(bromomagensio)butane was achieved by reacting 2 equivalents of magnesium turnings with 1,4-dibromobutane and heating to reflux in ether (35 °C) for 3.5 hours. Subsequent reaction with diethylaminodichlorophosphine, which can either be purchased or prepared,[111] results in cyclization and formation of the 5-membered phospholane ring as 1-diethylaminophospholane. Further purification of the 1-diethylaminophospholane is required by means of distillation. Following distillation, the addition of dichlorophenylphosphine yields the 1-chlorophospholane. Purification of the 1-chlorophospholane was achieved *via* a short track distillation apparatus under dynamic vacuum at a temperature of 60 – 75 °C. Once isolated, the chlorophospholane was further utilized in the remaining ligand synthesis.

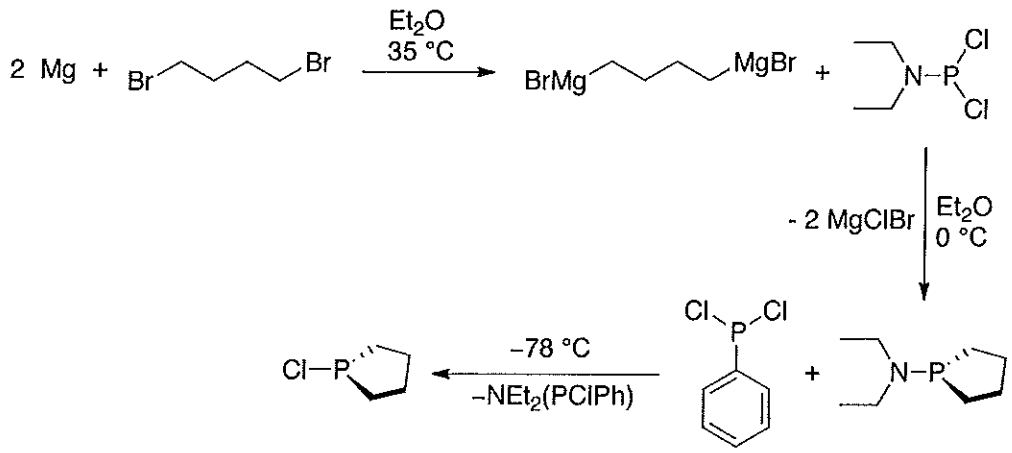

Scheme 2.5 Synthesis of 1-chlorophospholane.

To successfully install phosphinimine functionalities at the 1,8-positions of carbazole, the more active 3 and 6 sites must first be blocked. This is due to uncontrollable regioselectivity of carbazole with regards to electrophilic substitution reactions. Within the literature, two synthetically appealing options

which fulfill this requirement are known, bromination followed by methylation at the 3 and 6 positions (Scheme 2.6, **A**),[112] or Friedel-Crafts alkylation to yield the *t*-Bu derivative (Scheme 2.6, **B**).[113-114]

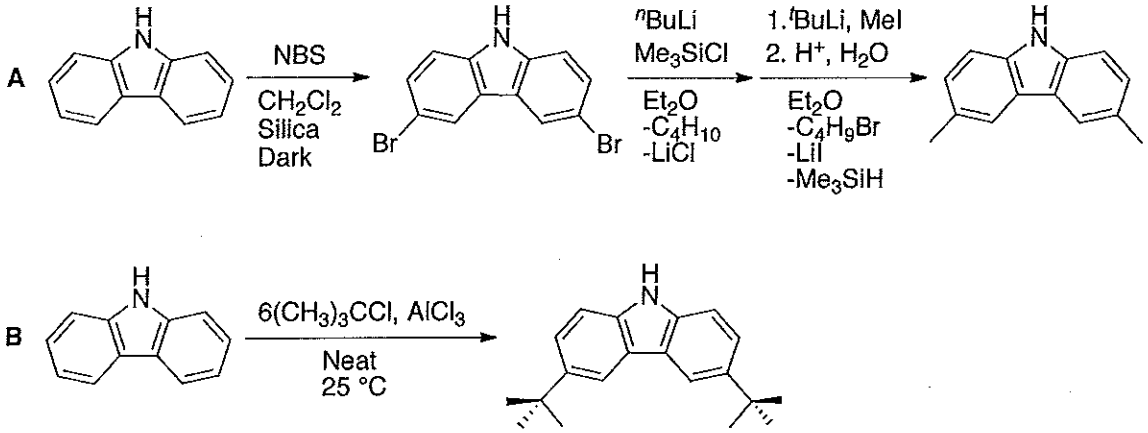

Scheme 2.6 Synthetic pathways for the **A**) methylation and **B**) Friedel-Crafts alkylation of carbazole.

Upon comparing the two options, route **A** was chosen due to the following rationale. Though additional synthetic steps are required for path **A**, an overall higher yield can be achieved (~90% for **A** vs. 47% for **B**).[112,114] This significant increase in yield also outweighs other factors, such as cost effectiveness regarding both materials and labour. The methyl groups also give rise to diagnostic signals in the ^{1}H NMR spectrum.

From the resultant 3,6-dimethyl-9H-carbazole, a second bromination can be performed using conditions similar to that employed for the first electrophilic substitution, yielding 1,8-dibromo-3,6-dimethyl-9H-carbazole (Scheme 2.7).[112] Before further derivatization, the NH of carbazole must be protected to prevent substitution at that site in future synthetic steps. Previous work in the Hayes lab demonstrated that installation of a *tert*-butoxycarbonyl (^{t}BOC) group by reacting

1,8-dibromo-3,6-dimethylcarbazole with di-*tert*-butyl-dicarbonate in the presence of catalytic 4-dimethylaminopyridine (DMAP), was a synthetically feasible approach to protect the NH group (Scheme 2.7).[64]

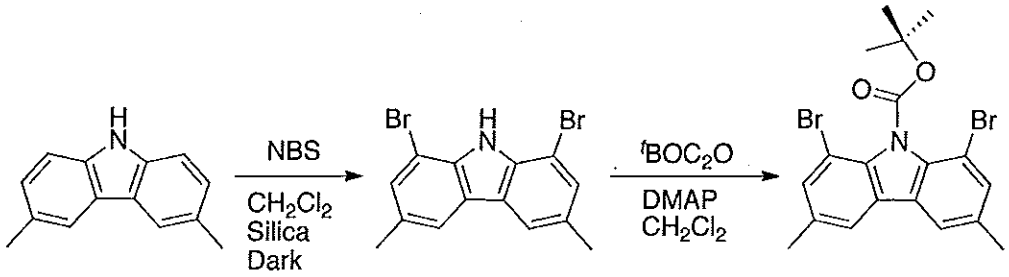

Scheme 2.7 Bromination and protection of 3,6-dimethylcarbazole.

2.4.2 Phospholane Installation

Following protection of the carbazole NH, a lithium-halogen exchange reaction was pursued to install the desired phosphine (PC_4H_8) (Scheme 2.8). In contrast to the synthesis of the previously reported diphenylphosphine derivative, a slight excess (2.2 equivalents) of ^{t}BuLi was added to the reaction mixture comprised of 1,8-dibromo-3,6-dimethyl-9-^{t}BOC-carbazolide dissolved in approximately equal amounts of tetrahydrofuran (THF) and diethyl ether (Et_2O). These modifications increased the nucleophilicity of the lithiation reagent, which was required to drive the reaction to completion. Upon generation of the protected bis(phospholane) (**9**), the BOC group was readily removed by heating the reaction mixture at 155 °C over a period of 3.5 hours, yielding the deprotected compound **10**.

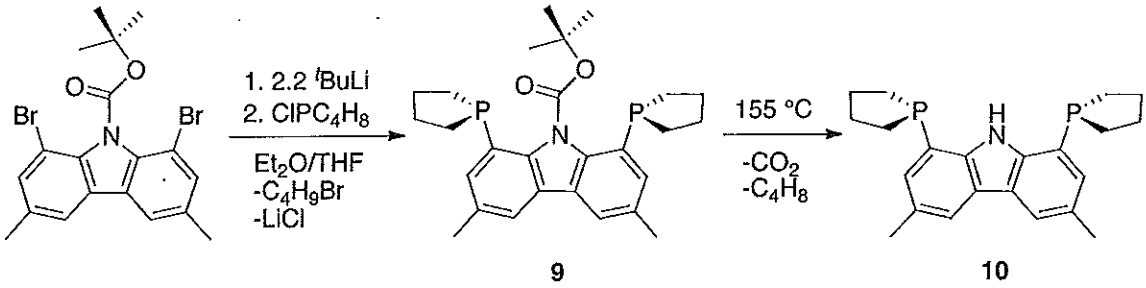

Scheme 2.8 Synthesis of bis(phospholane) (**10**).

Recrystallization of **10** from a concentrated pentane solution at ambient temperature over a period of two days yielded large yellow plates suitable for single crystal X-ray diffraction. The molecular structure of **10** is represented in Figure 2.9 and Figure 2.10 as thermal ellipsoid plots, with selected bond distances and angles presented in Table 2.1.

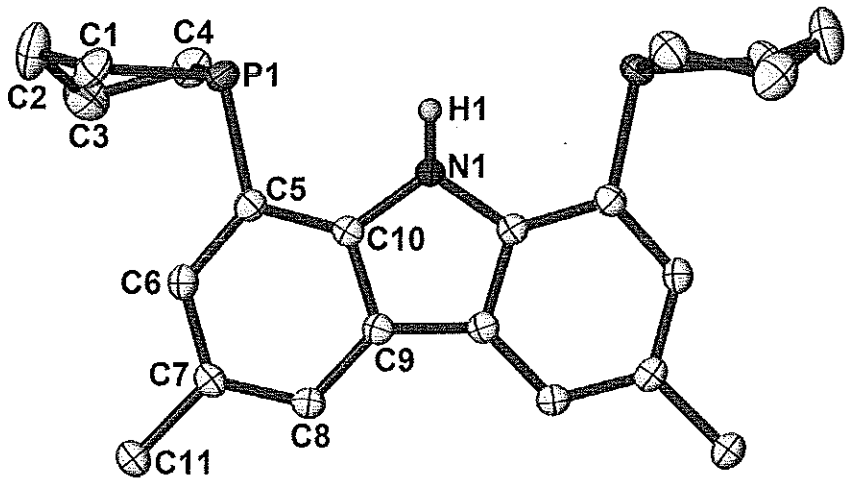

Figure 2.9 Thermal ellipsoid plot (50% probability) of bis(phospholane) **10**. All hydrogen atoms, except for H1, have been omitted for clarity.

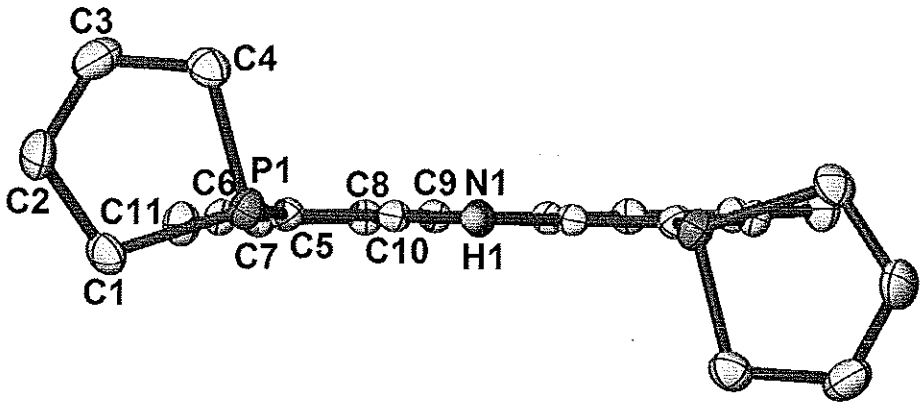

Figure 2.10 Top view of bis(phospholane) **10** represented with 50% probability ellipsoids. All hydrogen atoms, with the exception of H1, have been omitted for clarity.

Table 2.1. Selected bond lengths (Å), bond angles (°), and torsion angles (°) for compound **10**.

Bond Lengths (Å)		Bond Angles (°)		Torsion Angles (°)	
P_1–C_5	1.840(2)	C_5–P_1–C_4	101.26(8)	C_1–C_2–C_3–C_4	–45.6(2)
P_1–C_4	1.859(2)	C_5–P_1–C_1	104.15(8)	N_1 –C_{10} –C_5 –P_1	2.9(2)
P_1–C_1	1.864(2)	C_4–P_1–C_1	92.23(9)		
C_1–C_2	1.541(3)	C_2–C_1–P_1	107.2(1)		
C_2–C_3	1.517(3)	C_3–C_4–P_1	107.0(1)		
C_3–C_4	1.513(3)	C_3–C_2–C_1	108.6(2)		

Compound **10** crystallized in the orthorhombic space group, *Pbcn*. The molecule itself is highly symmetric, and exhibits crystallographic two-fold rotational symmetry in relation to N_1, which occupies the Wyckoff letter *c*. It is this two-fold symmetry that places the ring system of the phospholane moieties in opposite planes with respect to the carbazole scaffold (Figure 2.10). This loss of planarity is also expressed in the torsion angle N_1–C_{10}–C_5–P_1 (2.9(2)°, Table 2.1), and is marginally larger than that previously reported for **1b** (–0.4(7)°).[64] A slight increase in bond length between P_1–C_5 was also observed in comparing the bis(phospholane) to the analogous bis(diphenylphosphine) compound (P_1–$C_{carbazole}$ 1.795(5) and

1.786(5)), and is likely attributed to the added rigidity of the constrained rings creating greater steric repulsion between the phospholane and carbazole backbone. The carbazole framework appears to experience no distortion in the presence of the phospholane.

In addition, compound **10** was also thoroughly characterized by multinuclear NMR spectroscopy. In the $^{31}P\{^{1}H\}$ NMR spectrum, resonance of the phospholane groups attached to the 1 and 8 positions of carbazole appear at δ –35.6 (benzene-d_6). This value is significantly upfield from the free chlorophospholane, which is found at δ 126.4 (benzene-d_6). Due to fluxionality within the phospholane ring, in addition to extensive H–H and H–P coupling, the aliphatic region of the ^{1}H NMR spectrum corresponding to the CH_2 groups appears as multiple broad overlapping multiplets. This renders the phospholane protons difficult to discern from one another, and are therefore of limited diagnostic value.

2.4.3 Phosphinimine Formation

Reaction of the bis(phospholane) ligand **10** with *para*-isopropylphenyl (Pipp) azide in pentane at ambient temperature yielded the desired bis(phosphinimine) pincer ligand HL_1^{Pipp} (**11**) *via* a Staudinger reaction (Scheme 2.9). While there are a variety of aryl azides known, the *para*-isopropylphenyl azide was preferred in this instance for several reasons. First, the steric bulk of a Pipp ring is substantially less than other *N*-aryl rings utilized in similar work in the Hayes group (*e.g.* Mes, Dipp), and therefore this group was thought to be less likely to

participate in *N*-aryl cyclometalation. Secondly, the presence of the isopropyl moiety in the *para* position provides a diagnostic NMR resonance that is sensitive to metal complexation.

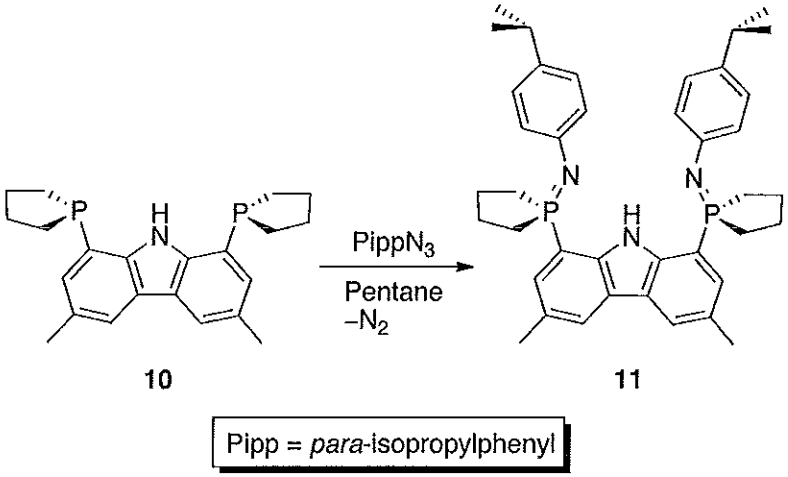

Scheme 2.9 Synthesis of $\mathbf{HL_1^{Pipp}}$ (**11**).

The resulting ligand exhibits a single resonance in the $^{31}P\{^1H\}$ NMR spectrum at δ 31.3 (benzene-d_6). Due to fluxionality in the phospholane rings, as well as complex short and long-range H–H and P–H coupling, the aliphatic region of the ^1H NMR spectrum corresponding to the phospholane groups is relatively uninformative. However, resonances in the ^1H NMR spectrum in benzene-d_6 from the Pipp methine (δ 2.78, sp), Pipp methyl (δ 1.22, d), carbazole methyl (δ 2.36) and carbazole NH (δ 12.55, s) are all particularly diagnostic for characterization.

In addition to identification by multinuclear NMR spectroscopy, compound **11** was structurally characterized by single-crystal X-ray diffraction. Colourless plate-like crystals of **11**·C_6H_6·C_5H_{12} were obtained from a concentrated solution of benzene layered with pentane at ambient temperature. Compound **11**·C_6H_6·C_5H_{12} crystallized in the space group *C*2/*c*, which belongs to a monoclinic crystal system.

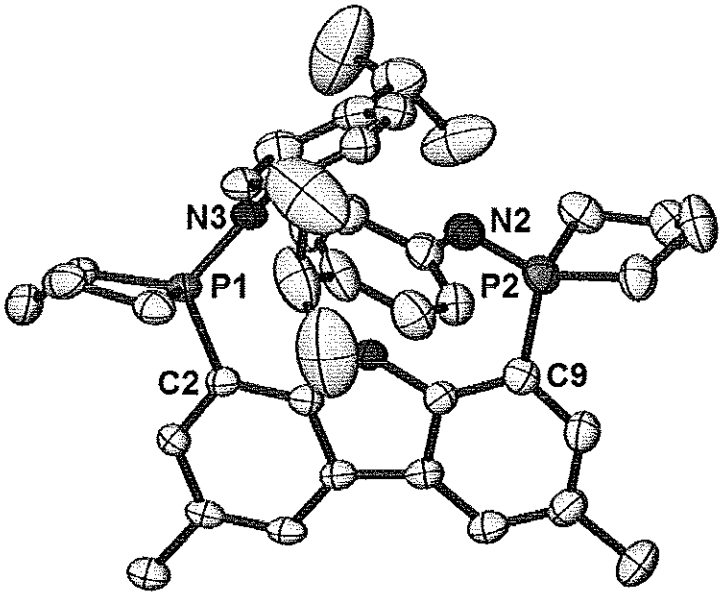

Figure 2.11 Thermal ellipsoid plot (50% probability) of **11** where hydrogen atoms have been omitted for clarity.

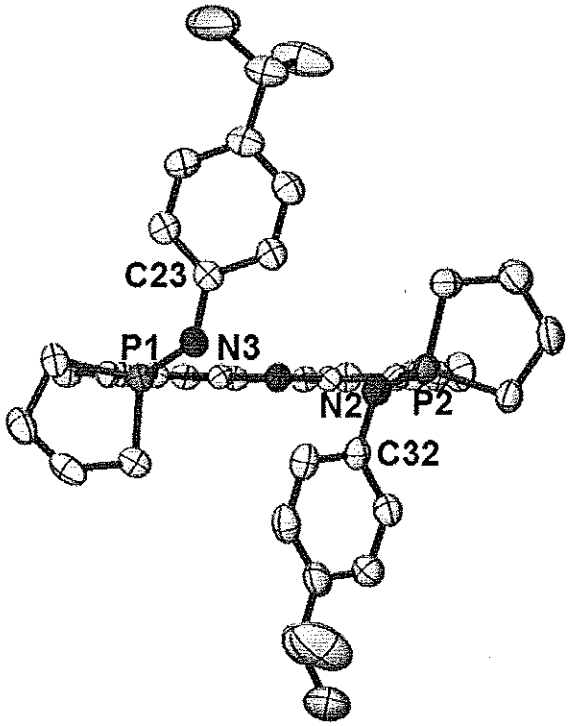

Figure 2.12 Molecular structure of **11** represented with 50% probability ellipsoids. Hydrogen atoms have been omitted for clarity.

As represented by the thermal ellipsoid plot in Figure 2.12, the *N*-aryl groups are arranged almost perpendicular with respect to the carbazole backbone. A similar arrangement was observed in the analogous bis(dimethylphosphinimine) scaffold **7**, but for the bis(diphenylphosphinimine) ligand **1**, a more planar conformation between carbazole and the *N*-aryl group was noted.[68] The orientation of the *N*-aryl ring to the aromatic plane of carbazole can be represented by the torsion angle between carbazole and the aryl moiety (C–P–N–C). With regards to the bis(diphenylphosphinimine) ligand **1**, this torsion angle is closer to 180° (170.0(4) and -177.7(4)),[64] whereas for HL_1^{Pipp} (**11**) and the bis(dimethylphosphinimine) **7**, this value is between 60 – 70°.[68] This discrepancy is attributed to crystal packing effects whereby the *N*-aryl group experiences a decrease in steric congestion in the presence of less bulky phosphines, allowing the molecules to pack more efficiently. While likely an artifact of crystal packing effects, this geometry could potentially result in increased steric congestion at the tridentate binding pocket.

The phosphinimine P–N bond lengths of **11** were measured to be 1.575(3) Å for P_1–N_3 and 1.572(3) Å for P_2–N_2, and are within the expected range of P–N double bonds for comparable ligand systems.[64,67-68,115] A distorted tetrahedral geometry about the phosphorus atoms was also noted. Of particular interest are the bond angles with respect to phosphorus within the phospholane rings (C_{18}–P_1–C_{15}, C_{19}–P_2–C_{22}) which were found to be quite similar at 95.73(17)° and 95.22(18)°, respectively. These angles suggest a highly constrained ring system that would ideally prevent the phospholane rings from interacting with the metal centre. In fact, these angles suggest an even greater strained cyclic phosphine than the

dioxophospholane derivative also developed in the Hayes lab, which displays bond angles of 96.37(6)° and 96.66(6)° for the analogous O–P–O bonds.[68]

Table 2.2. Selected bond lengths (Å), bond angles (°), and torsion angles (°) for compound **11**.

Bond Lengths (Å)		Bond Angles (°)		Torsion Angles (°)	
P_1–C_2	1.807(3)	C_2–P_1–N_3	112.30(14)	C_9–P_2–N_2–C_{32}	72.0(3)
P_2–C_9	1.808(3)	C_9–P_2–N_2	114.37(15)	C_2–P_1–N_3–C_{23}	61.4(3)
P_1–N_3	1.575(3)	C_{18}–P_1–C_{15}	95.73(17)	C_1–C_2–P_1–N_3	34.1(3)
P_2–N_2	1.572(3)	C_{19}–P_2–C_{22}	95.22(18)	C_8–C_9–P_2–N_2	23.2(3)

2.5 Metal Complexation

Proteo ligand **11** was readily reacted with trialkyl lanthanide reagents to generate the desired lanthanide dialkyl species. This complexation pathway, commonly referred to as alkane elimination/metathesis, is desirable as loss of a volatile alkane drives the reaction to completion and allows for facile purification of the desired metal complex. In the context of this thesis, the reagents $Ln(CH_2SiMe_3)_3(THF)_2$ (Ln = Sc; Lu) were utilized for comparative purposes with similar systems. Reactions were followed using NMR spectroscopy in benzene-d_6, upon which the evolution of one equivalent of $SiMe_4$ was indicative of metal complexation. Due to differences in thermal stability, metal complexation with both Sc and Lu will be discussed separately.

2.5.1 *In situ* Generation of $L_1^{Pipp}Lu(CH_2SiMe_3)_2$ (**12**)

The lutetium dialkyl complex **12** was successfully generated *in situ* as outlined in Scheme 2.10 and characterized using multinuclear NMR spectroscopy. Over time, it was noted that the resultant compound **12** was thermally unstable upon loss of a second equivalent of $SiMe_4$ observed in the ^1H NMR spectrum as well as additional resonances in the ^{31}P NMR spectrum. As such, isolation of **12** as an analytically pure solid was never achieved due to uncontrollable decomposition.

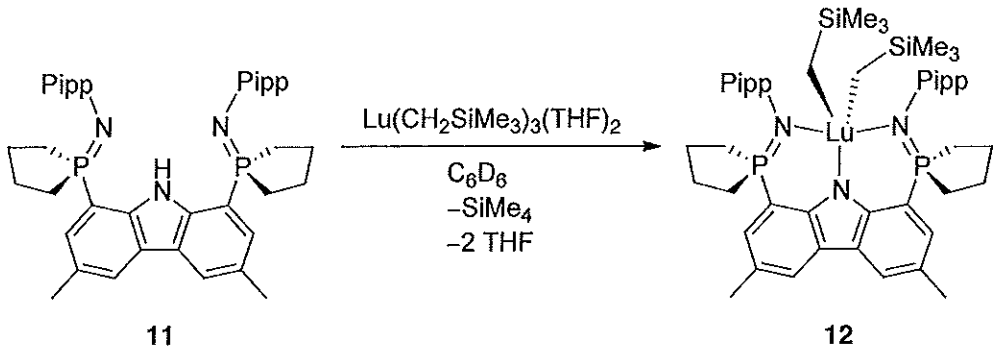

Scheme 2.10. Synthesis of $L_1^{Pipp}Lu(CH_2SiMe_3)_2$ (**12**).

Compound **12** exhibits a κ^3 coordination mode to lutetium through the nitrogen atoms. This is corroborated by the $^{31}P\{^1H\}$ NMR spectrum of **12**, whereby a single resonance at δ 54.6 is observed (benzene-d_6). A chemical shift change of over 20 ppm downfield was observed between the proteo ligand (δ 31.3, benzene-d_6) and the metal complex, demonstrating the sensitivity of the phosphinimine functionality to its chemical environment. The methylene groups bound to the metal appear as a single resonance in the ^1H NMR spectrum slightly upfield of δ 0 at δ –0.57 in deuterated benzene, indicating that both CH_2 groups are equivalent on the NMR time scale. Signals for the equivalent $Si(CH_3)_3$ groups were observed slightly

downfield from 0 ppm (δ 0.14, benzene-d_6). While two equivalents of THF were generated *in situ* in this reaction, the THF resonances observed in the ^{1}H NMR spectrum render it difficult to conlude that THF is coordinated to the metal centre (Table 2.3). However, attempts to remove the THF under vacuum resulted in complete decomposition as determined by both ^{31}P{^{1}H} and ^{1}H NMR analysis, though this could also be due to the inherent thermal sensitivity of the compound in question.

Table 2.3 ^{1}H NMR resonances of THF in different chemical environments in benzene-d_6.

Compound	Proton	Resonance (ppm)
THF[116]	CH_2	1.40
	CH_2O	3.57
$Lu(CH_2SiMe_3)_2(THF)_2$	CH_2	1.38
	CH_2O	3.97
12	CH_2	1.37
	CH_2O	3.54

2.5.2 Thermal Decomposition of ***12***

Under ambient conditions, compound **12** slowly decomposes to a compound of low symmetry, as evident by the appearance of two resonances of equal intensity in the ^{31}P{^{1}H} NMR spectrum (δ 55.9 and 53.1, benzene-d_6). In addition, the loss of one equivalent of $SiMe_4$ was observed at δ 0.00 in the ^{1}H NMR spectrum. Combined, the spectral evidence suggests an intramolecular C–H bond activation, resulting in the formation of a singly cyclometalated complex. This metalative process is postulated to take place between the *N*-aryl ring and lutetium metal centre, yielding the cyclometalated complex **13** shown in Scheme 2.11. While the development of a C_{ipso}–Lu bond is anticipated to appear at ~δ 200 in the ^{13}C NMR spectrum upon

metalation, P–C coupling and the thermal sensitivity of the decomposition product is believed to have hindered the observation of such a resonance. An alternative option to the *N*-aryl C–H bond activation is cyclometalation between the phospholane rings and lutetium. However, the ^{13}C NMR and DEPT–135 NMR spectra accounts for both unique CH_2 resonances that comprise the phospholane groups (δ 26.25, d, and δ 26.16, d), corroborating that metalation is likely occurring *via* the *ortho*-position of the Pipp functionality.

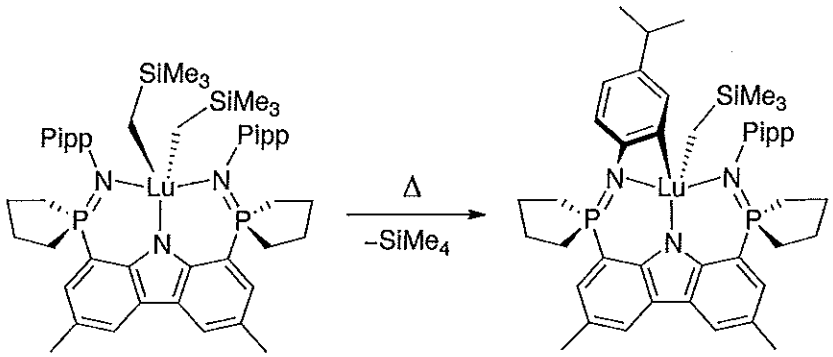

12 **13**

Scheme 2.11. Intramolecular C-H bond activation of $L_1^{Pipp}Lu(CH_2SiMe_3)_2$ (**12**) to form **13**.

Following decomposition to the singly metalated compound, further degradation to a series of unknown products was observed by spectroscopic analysis. Instability of the *N*-aryl metalated product made its full characterization extremely difficult, even at low temperatures, and isolation of a well-behaved solid was not achieved. The complicated nature of this mixture of decomposition products has precluded their identification.

2.5.3 *Kinetic Analysis of Ligand Metalation*

The decomposition pathway of $L_1^{Pipp}Lu(CH_2SiMe_3)_2$ (**12**) to **13** was followed quantitatively using $^{31}P\{^1H\}$ NMR spectroscopy, with samples prepared in toluene-d_8 at –78.5 °C and allowed to warm to the chosen temperature once inserted into the probe. As demonstrated in Figure 2.13, disappearance of the peak at δ 54.6 corresponding to compound **12** along with simultaneous emergence of two resonances of equal intensity at δ 55.9 and 53.1 attributed to the asymmetric complex **13** was observed at ambient temperature (295.3 K) over 10800 s.

In determining the order of the decomposition pathway, a total of 5 experiments were performed and followed at temperatures ranging from 273.0 – 313.0 K. The half-lives of reaction, as well as k_{obsvd} for each trial are reported in Table 2.4. Generation of a first order plot (Figure 2.14) with the obtained time and concentration data from these experiments revealed that the decomposition of $L_1^{Pipp}Lu(CH_2SiMe_3)_2$ (**12**) follows first order kinetics as indicated by the linearity of the resultant lines at different temperatures. This data allowed for the construction of an Eyring plot, shown in Figure 2.15. Activation parameters $\Delta H^{\ddagger}$ and $\Delta S^{\ddagger}$ were determined to be 74.50 ± 0.58 kJ·mol^{-1} and –58.13 ± 0.97 J·mol^{-1}·K^{-1}, respectively. The $\Delta H^{\ddagger}$ value is quite similar to that previously determined for the *N*-aryl cyclometalation of **1b** (73.52 kJ·mol^{-1}), supporting the notion of a similar decomposition pathway between the two compounds. In addition, these values correspond well with other examples of intramolecular C–H bond activation.[36,66]

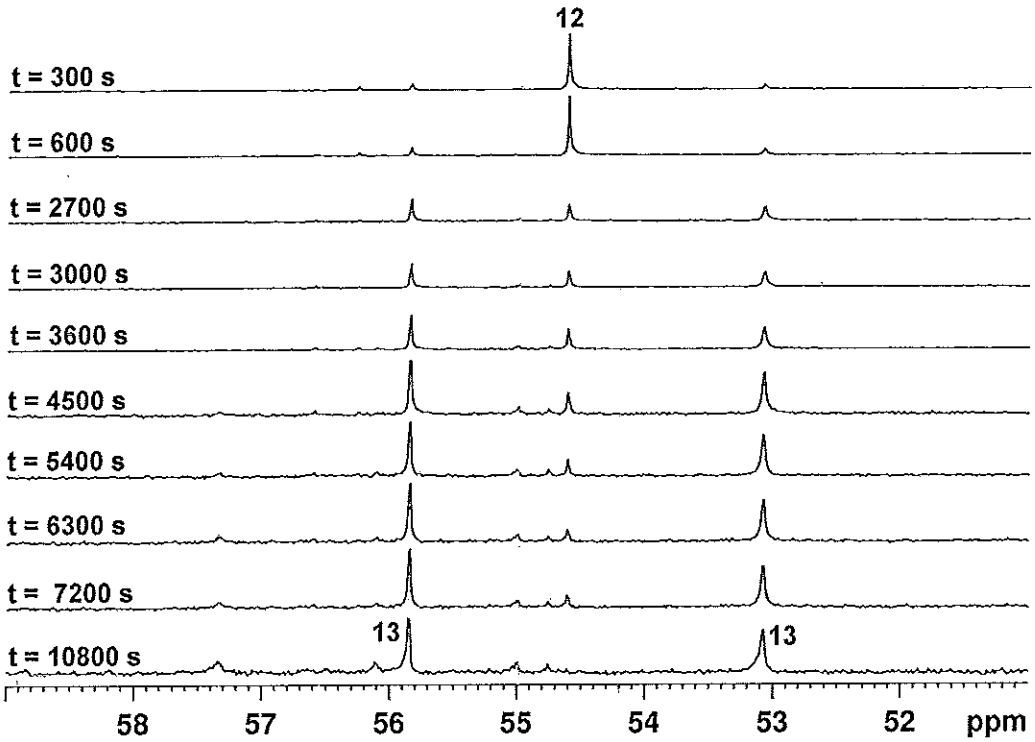

Figure 2.13 Stacked plot of $^{31}P\{^{1}H\}$ NMR spectra following the decomposition of **12** to **13** at 295.3 K from t = 300 s to t = 10800 s.

Table 2.4 k_{obsvd} and half-lives for the decomposition of **12** at different temperatures.

Temperature (K)	k_{obsvd} (s^{-1})	$t_{1/2}$ (h)
273.0	2.50×10^{-5}	7.70
283.0	8.80×10^{-5}	2.19
295.3	3.74×10^{-4}	0.51
303.0	9.63×10^{-4}	0.20
313.0	3.10×10^{-3}	0.062

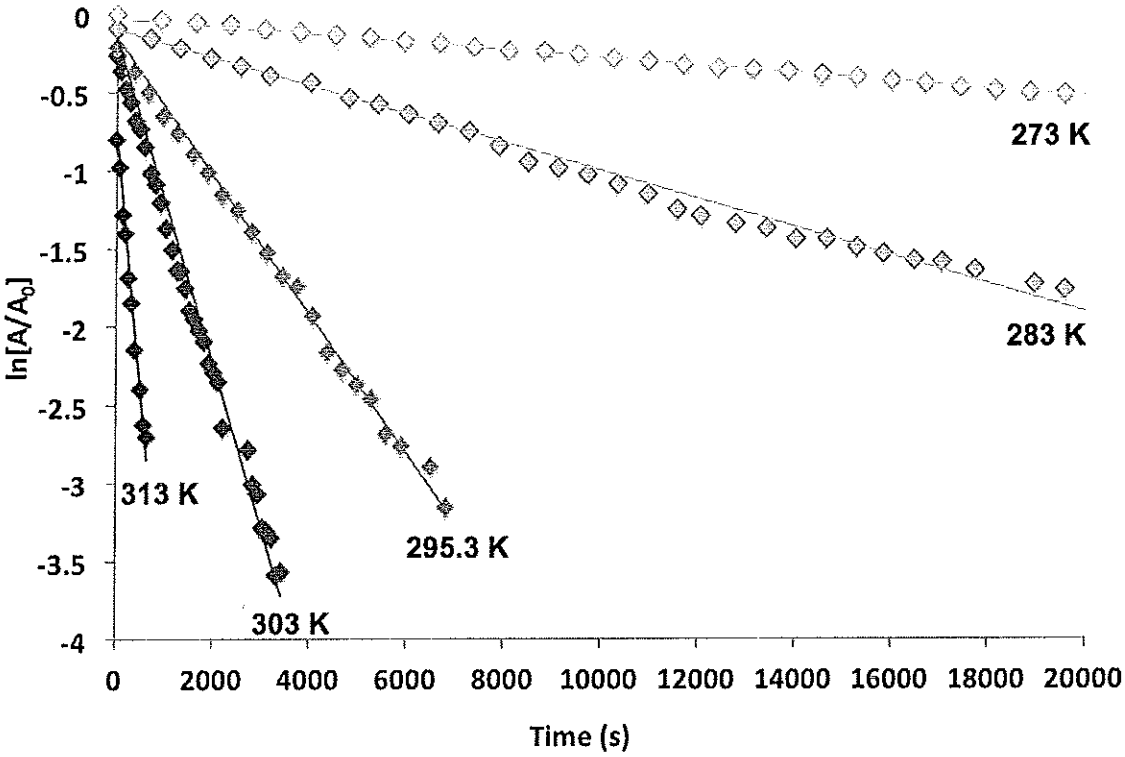

Figure 2.14 First order plots for the decomposition of **12** at temperatures from 273.0 K – 303.0 K.

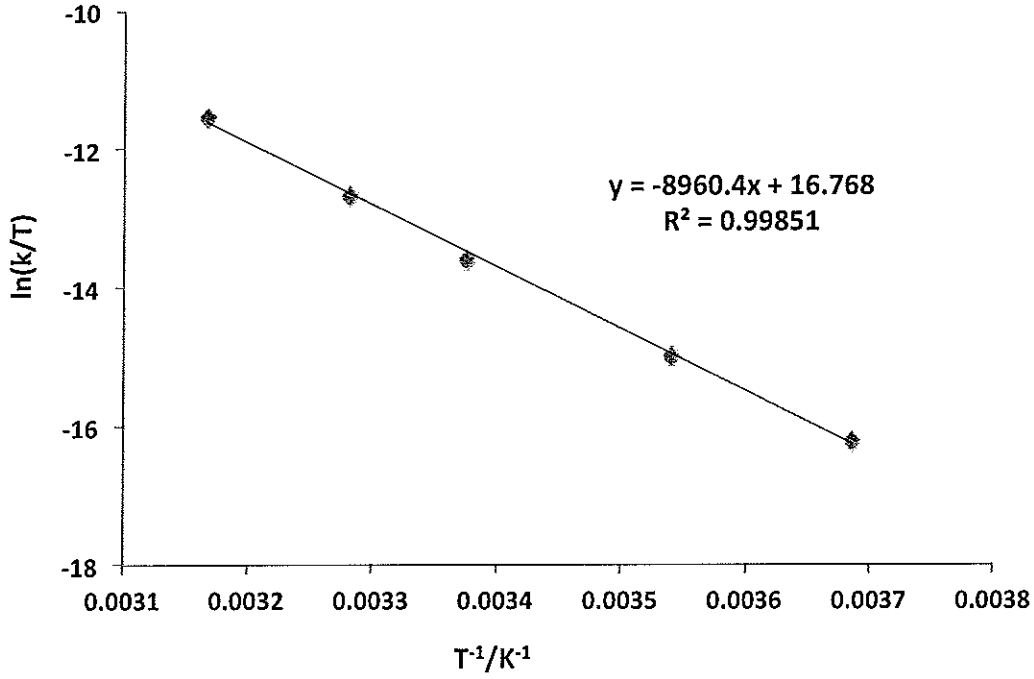

Figure 2.15 Eyring plot of the cyclometalation of **12**.

2.5.4 *In situ* Synthesis of $L_1^{Pipp}Sc(CH_2SiMe_3)_2$ (**14**)

Synthesis of $L_1^{Pipp}Sc(CH_2SiMe_3)_2$ (**14**) was achieved *in situ* upon reaction of $Sc(CH_2SiMe_3)_2(THF)_2$ with one equivalent of HL_1^{Pipp} (**11**) in benzene-d_6 at ambient temperature (Scheme 2.12). As found in the lutetium analogue, scandium is chelated in a symmetric κ^3 fashion, which is evident in the $^{31}P\{^1H\}$ NMR spectrum where one single resonance is detected at δ 55.0 (benzene-d_6). This bonding motif is also apparent in the ^1H NMR spectrum, as only one set of resonances are observed for both the ligand and metal protons. With respect to **14**, the scandium methylene moieties appear slightly downfield at δ –0.19. Again, THF resonates very closely to free THF, and thus it is reasonable to expect it to be weakly bound to Sc, if at all (Table 2.5). Isolation of **14** as a solid was attempted but it could not be obtained as an analytically pure material due to its thermal instability.

Table 2.5 Comparison of ^1H NMR THF resonances in different chemical environments in benzene-d_6.

Compound	Proton	Resonance (ppm)
THF[116]	CH_2	1.40
	CH_2O	3.57
$Sc(CH_2SiMe_3)_2(THF)_2$	CH_2	1.34
	CH_2O	4.04
14	CH_2	1.38
	CH_2O	3.58

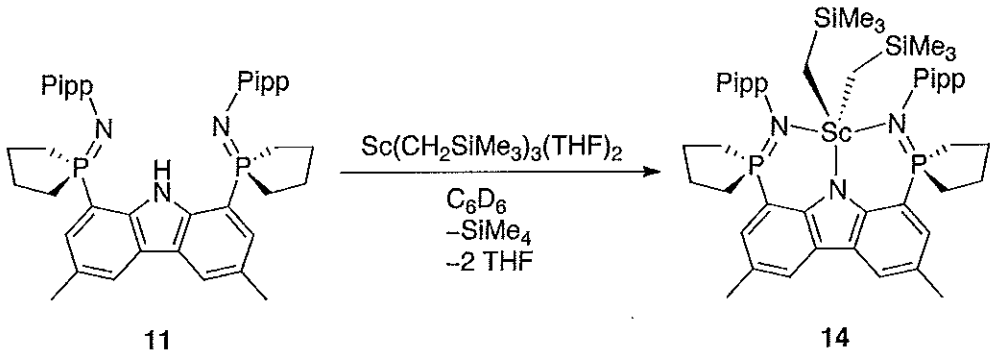

11 14

Scheme 2.12 Synthesis of $L_1^{Pipp}Sc(CH_2SiMe_3)_2$ (**14**).

*2.5.5 Thermal Decomposition of **14***

At ambient temperature, $L_1^{Pipp}Sc(CH_2SiMe_3)_2$ (**14**) slowly degrades. Evidence of this degradation was initially determined using $^{31}P\{^1H\}$ NMR spectroscopy. As shown in the stacked plot presented in Figure 2.16 presence of the dialkyl compound is indicated by the peak at δ 55.0 (benzene-d_6). Over time, the resonance at δ 55.0 slowly decreases in intensity as the simultaneous appearance of two new peaks at δ 53.0 and δ 56.1 are observed, suggesting the formation of a compound with low symmetry. Finally, disappearance of the resonances at δ 53.0 and δ 56.1 occurs with the concomitant emergence of a single resonance at δ 56.2, which is attributed to the formation of a new C_{2v} symmetric compound.

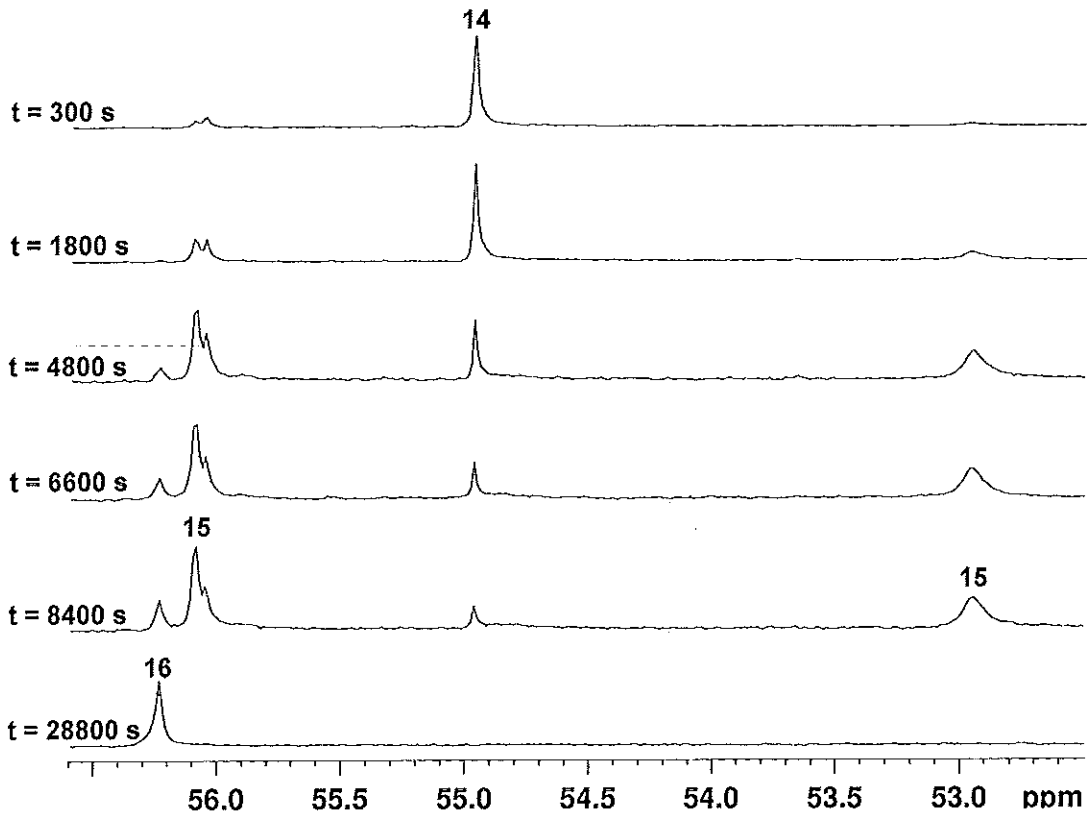

Figure 2.16 Stacked plot of the decomposition of **14** followed by $^{31}P\{^{1}H\}$ NMR spectroscopy at 294.2 K.

Though the $^{31}P\{^{1}H\}$ NMR spectral data does not provide significant structural information about the final decomposition product, analysis of ^{13}C NMR data has allowed for the unambiguous determination of a doubly metalated Sc complex (**16**), whereby cyclometalation occurs through the phospholane rings. In particular, DEPT NMR characterization techniques were instrumental as the CH_2 region corresponding to the phospholane groups was of significant interest. Figure 2.17 shows the DEPT–135 NMR spectrum of **16**, whereby the CH_2 moieties point down, and CH and CH_3 functionalities point up. Aside from THF at 25.60 ppm, the remaining CH_2 peaks correspond to the phospholane ring, in which there are a total

of three resonances. Ideally, if no metalation had occurred, a total of two CH_2 resonances would be present corresponding to the phospholane moieties, as found with the proteo ligand HL_1^{Pipp}. If metalation of only one phospholane group occurred, a spectrum with five unique CH_2 resonances in the aliphatic region would be expected. The presence of three doublets, however, corresponds to three unique CH_2 functionalities, which could only occur by cyclometalation of two CH_2 groups with each phospholane being singly cyclometalated. The calculated coupling constants of the remaining phospholane CH_2 groups correspond to expected values of one and two bond J_{CP} coupling ($^1J_{CP}$ = 43.85 Hz; $^2J_{CP}$ = 3.78 and 17.39 Hz), and are not significantly different from that observed in HL_1^{Pipp} ($^1J_{CP}$ = 64.26 Hz; $^2J_{CP}$ = 11.34 Hz).

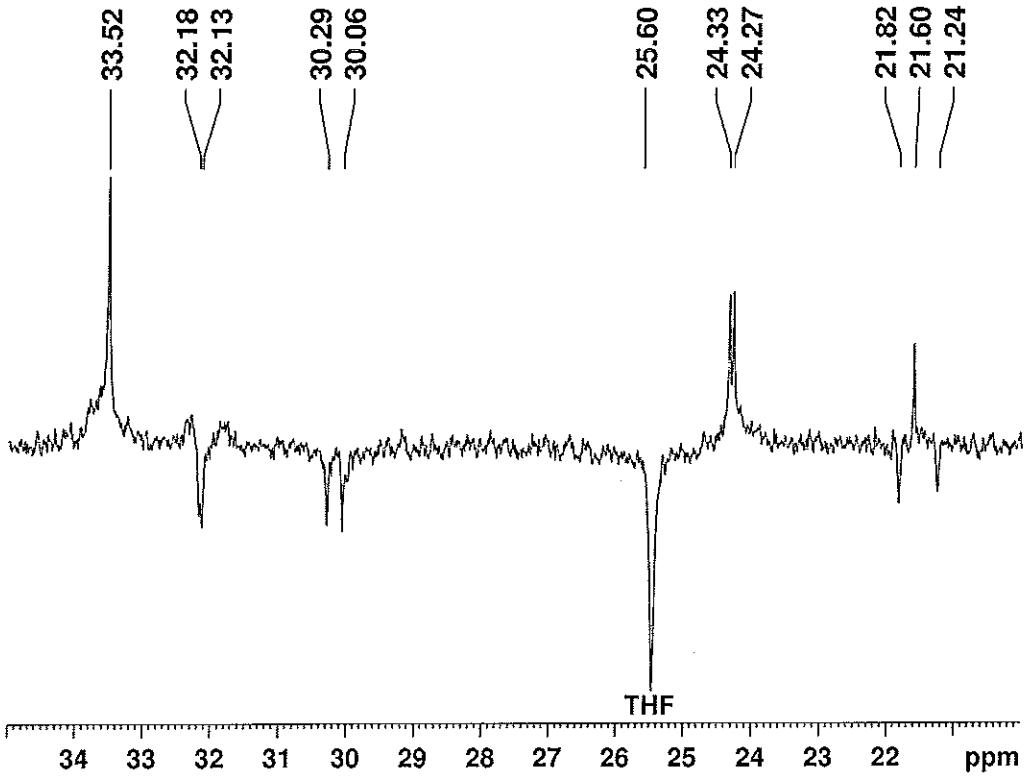

Figure 2.17 DEPT-135 NMR spectrum of **16**.

Presence of the Sc–CH group was a bit more elusive from an NMR characterization standpoint as scandium is a quadrupolar nucleus ($I = 7/2$), and can cause line broadening in the resonances of adjacent nuclei. In addition, the presence of $^1J_{CP}$ coupling decreases the overall intensity of such peaks. For these reasons, the Sc–CH was not readily observed in the DEPT–135 NMR spectrum. By employing DEPT–90 techniques, however, removal of an overlapping CH_2 functionality allowed for clear visualization of the metalated carbon, which resonates at δ 32.2 (Figure 2.18).

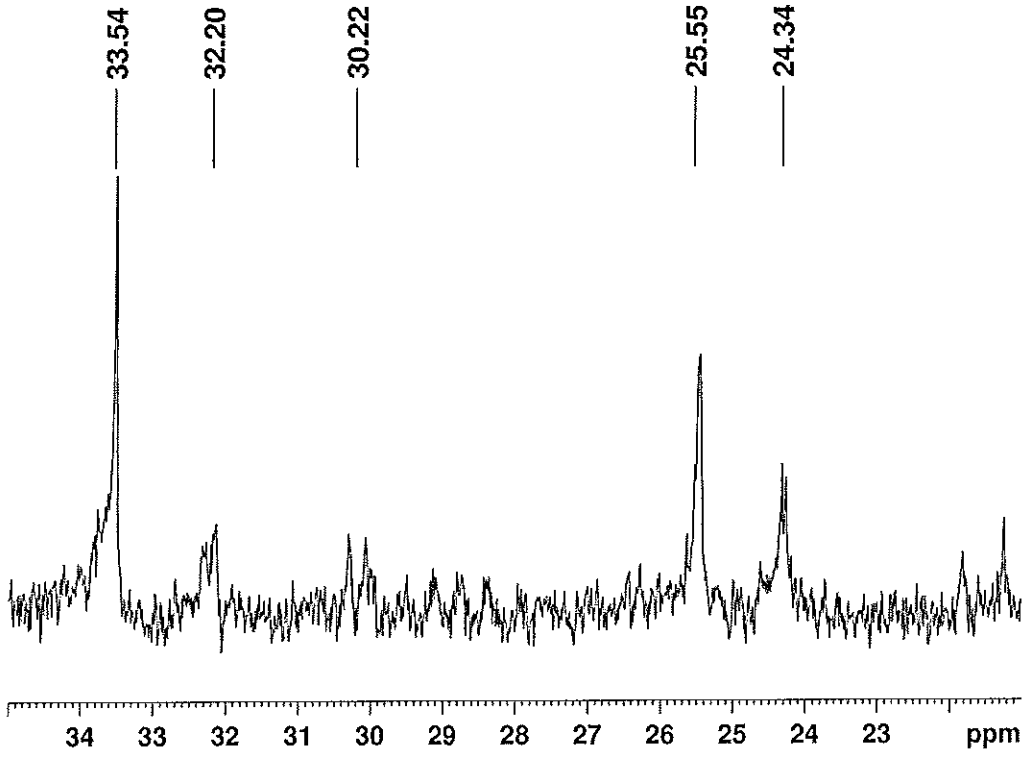

Figure 2.18 DEPT–90 NMR spectrum of **16**.

The formation of **16** is believed to occur by two sequential cyclometalative C–H bond activations of the phospholane rings (Scheme 2.13). Following synthesis of the dialkyl compound **14**, cyclometalation most likely proceeds *via* one

phospholane ring, indicated by compound **15** in Scheme 2.13. Evolution of this asymmetric compound is supported by $^{31}P\{^{1}H\}$ NMR data (Figure 2.16), whereby the two peaks previously discussed (δ 53.0 and δ 56.1) are representative of its existence. In addition, the ^{1}H NMR data also depicts a low symmetry compound, as well as the loss of additional $SiMe_4$. As the reaction proceeds, both the singly metalated and doubly metalated scandium compounds are present, making the kinetics of this process difficult to ascertain. However, it is of interest to note that the decomposition of **14** is slower than that observed for compounds **1a**, **1b**, and **12**, with complete loss of **14** observed only after 2.5 hours at 21.0 °C, and 100% conversion to **16** requiring over 6 hours. In comparison, **1a** and **1b** underwent full decomposition after 4 hours, and **12** after 3 hours under ambient conditions.

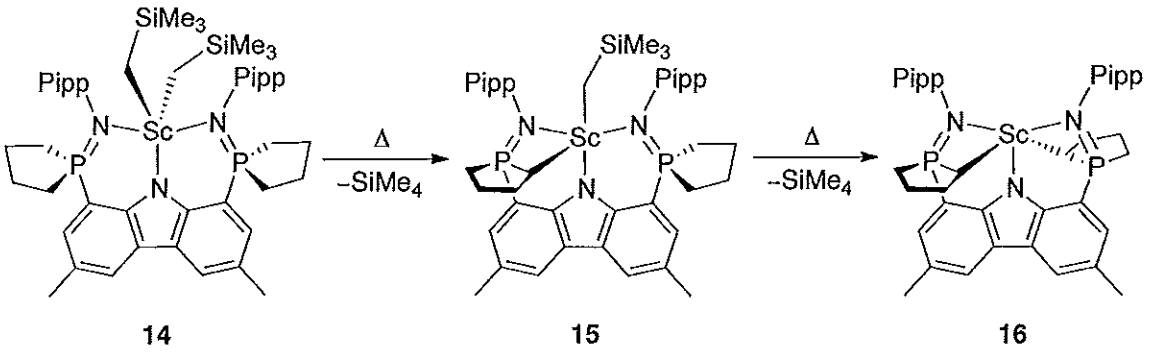

14 **15** **16**

Scheme 2.13 Decomposition of **14** through two sequential intramolecular metalative processes.

Attempts to isolate the doubly cyclometalated compound yielded a mixture of intractable products. For this reason, no further synthetic chemistry was conducted with compound **16**.

2.6 Computational Analysis of HL_1^{Pipp} and Associated Metal Complexes

The thermal instability of compounds **12** and **14** hindered the ability to successfully grow and isolate crystals suitable for X-ray diffraction. To gain structural insight with regard to the metal complexes and their respective decomposition products, computational chemistry was employed. As a means of determining method validity and ensuring accurate representation of the ligand geometry, the crystal structure of HL_1^{Pipp} (**11**) was optimized at the B3WP91/6-31G(d,p) level of theory. Select structural parameters of this optimized structure and those of the crystal structure are compared in Table 2.6, with the computationally determined structure presented in Figure 2.19. Some deviations in bond angles and torsion angles are evident, and may be reflective of the crystal packing environment present during determination of the solid state structure of **11**.

Table 2.6 Select bond lengths (Å) and angles (°) of the computationally and crystallographically determined structure of **11**.

Bond Lengths (Å)		Bond Angles (°)		Torsion Angles (°)	
Calculated Values					
P_1–C_2	1.824	C_2–P_1–N_3	114.78	C_9–P_2–N_2–C_{32}	72.7
P_2–C_9	1.827	C_9–P_2–N_2	114.33	C_2–P_1–N_3–C_{23}	68.1
P_1–N_3	1.595	C_{18}–P_1–C_{15}	95.61	C_1–C_2–P_1–N_3	30.8
P_2–N_2	1.594	C_{19}–P_2–C_{22}	95.91	C_8–C_9–P_2–N_2	28.5
Crystallographic Values					
P_1–C_2	1.807(3)	C_2–P_1–N_3	112.30(14)	C_9–P_2–N_2–C_{32}	72.0(3)
P_2–C_9	1.808(3)	C_9–P_2–N_2	114.37(15)	C_2–P_1–N_3–C_{23}	61.4(3)
P_1–N_3	1.575(3)	C_{18}–P_1–C_{15}	95.73(17)	C_1–C_2–P_1–N_3	34.1(3)
P_2–N_2	1.572(3)	C_{19}–P_2–C_{22}	95.22(18)	C_8–C_9–P_2–N_2	23.2(3)

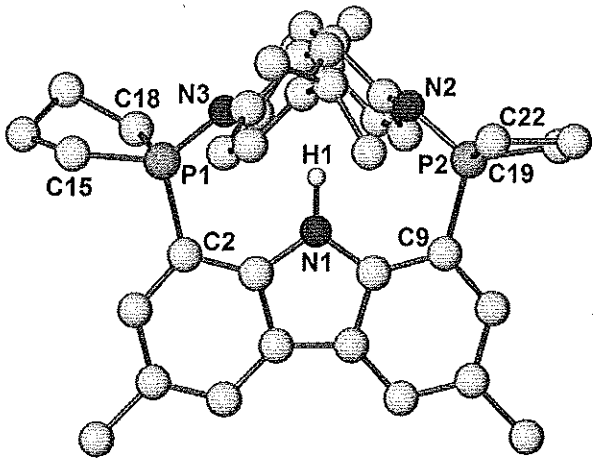

Figure 2.19 Computationally optimized structure of **11** using B3WP91/6-31G(d,p).

2.6.1 Computational Analysis of $L_1^{Pipp}Lu(CH_2SiMe_3)_2$ (12) and $L_1^{Pipp}Sc(CH_2SiMe_3)_2$ (14)

Due to the synthetic environment utilized for the *in situ* generation of compounds **12** and **14**, these experimental conditions had to be reflected within the calculation parameters for examining the rare earth complexes. This was achieved by performing all calculations in implicit solvent (benzene, $\varepsilon = 2.2706$) by employing the IEF-PCM formalism.[117] In addition, the presence of two equivalents of THF had to be accounted for. With the level of interaction between THF and the metal centre unclear, three scenarios were considered during the geometry optimizations of **12** and **14** to determine the role THF has with regards to the chemical system: **a**) two free THF molecules, **b**) one THF molecule coordinated to the metal centre, one free, and **c**) two THF molecules coordinated to the metal centre. These THF molecules were explicitly added to the computational model and allowed to freely optimize.

For both the geometry optimization and frequency calculations, the ligand framework, THF molecules, and Ln-alkyl groups were treated at the B3WP91/6-31G(d,p) level of theory. Alternatively, the lanthanide atom was optimized with their quasi-relativistic Stuttgart-Dresden effective core potential, ECP60MWB (Lu) and ECP10MDF (Sc), and its respective basis set to take into account the presence of the *f* orbitals.[118]

The resultant molecular structures for compound **12** with two THF molecules are represented in Figure 2.20, Figure 2.21, and Figure 2.22. In each case, the Lu atom deviates from the centre of the binding pocket, and adopts a distorted square pyramidal geometry without THF coordination, and a distorted octahedral geometry with coordination of THF. Most interestingly, attempts to optimize L_1^{Pipp} $Lu(CH_2SiMe_3)_2(THF)_2$ with two coordinated THF molecules was unsuccessful, as only one THF is observed within proximity of the metal centre (Figure 2.22). This is likely attributed to steric contributions of the ligand (**11**).

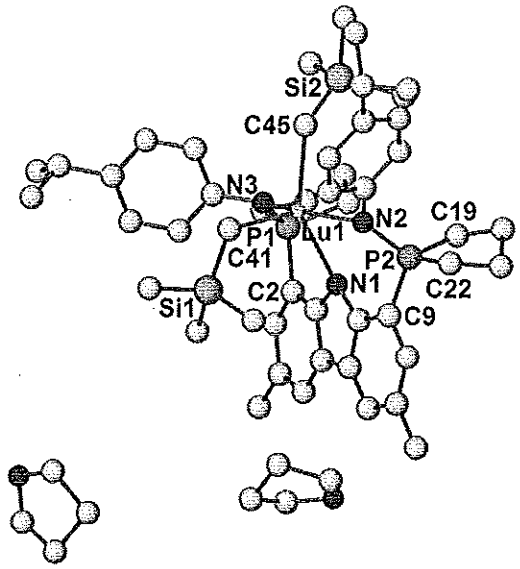

Figure 2.20 Molecular representation of $L_1^{Pipp}Lu(CH_2SiMe_3)_2$ (**12a**) with two free THF molecules. H atoms have been omitted for clarity.

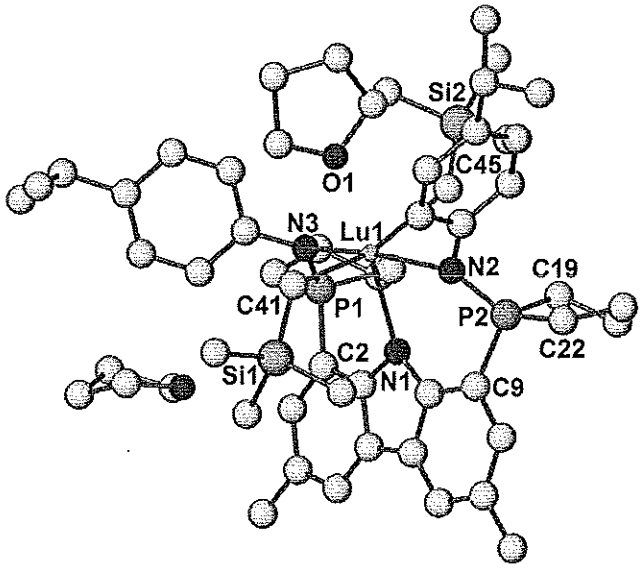

Figure 2.21 Molecular representation of $L_1^{Pipp}Lu(CH_2SiMe_3)_2$ (**12b**) with one coordinated and one free THF molecule. H atoms have been omitted for clarity.

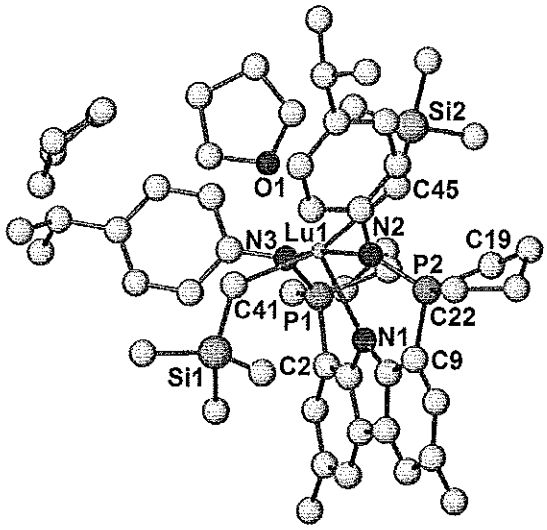

Figure 2.22 Molecular representation of $L_1^{Dipp}Lu(CH_2SiMe_3)_2$ (**12c**), whereby the starting approximation included two coordinated THF molecules. H atoms have been omitted for clarity.

Relative energies of the three options can be found in Table 2.7, and were obtained from single-point calculations performed at the B3WP91/6-311G+(2d,p) level of theory for C, H, N, Si, and O atoms, and include zero-point vibrational energy (ZPVE) corrections. Due to the complex nature of the basis sets employed, the ZPVE could not accurately be scaled. The Lu atom was again treated with its appropriate basis set and ECP60MWB pseudopotential. Three structures were analyzed, in which all are to be considered a local minima. As such, more structures may exist, but of the three analyzed, **12a** has the lowest energy profile, and is therefore the most stable conformation. In comparing **12a** with **12b** and **12c**, this added stability most likely stems from the fact that THF does not interact with the metal centre. In fact, in comparing the structures of **12b** and **12c**, it appears that the greater the interaction of the THF molecules, the higher the energy of the resultant complex.

This could be a result of steric crowding at the metal centre, forcing the metal to attain an energetically unfavorable geometry. Presented earlier in Section 2.4.1, the level of THF coordination, if any, was debated. The geometry optimized structure of **12a**, however, suggests that THF indeed is not coordinated.

Table 2.7 Relative energies of the different geometry optimizations for compound **12**.

Complex	Relative Energy (kJ•mol^{-1})
12a	0.000
12b	9.098
12c	20.614

Select bond lengths, angles, and torsion angles for **12a** are presented in Table 2.8. The Lu_1–N bond lengths are slightly longer than those found for the similar ligand system, **2b** (N_1–Lu_1: 2.343(6) Å; N_2–Lu_1: 2.293(6) Å; N_3–Lu_1: 2.285(6) Å).[64] This increase in bond length could be attributed to reduced steric pressure at lutetium due to the phospholane rings. In comparison to the crystal structure of proteo ligand **12**, an increase in torsion angles is noted, suggesting flexibility in the ligand scaffold to accommodate the lutetium dialkyl.

Table 2.8 Select bond lengths (Å) and angles (°) of the computationally determined molecular structure of **12a**.

Bond Lengths (Å)		Bond Angles (°)		Torsion Angles (°)	
N_1–Lu_1	2.548	C_2–P_1–N_3	112.87	C_1–C_2–P_1–N_3	–54.2
N_2–Lu_1	2.400	C_9–P_2–N_2	109.80	C_8–C_9–P_2–N_2	53.8
N_3–Lu_1	2.393	N_1–Lu_1–C_{41}	114.64	C_2–P_1–N_3–C_{23}	–94.0
C_2–P_1	1.793	C_{41}–Lu_1–C_{45}	101.66	C_9–P_2–N_2–C_{32}	144.2
C_9–P_2	1.794	N_1–Lu_1–C_{45}	143.69		
Lu_1–C_{41}	2.363	N_2–Lu_1–N_3	156.16		
Lu_1–C_{45}	2.399				

Similar results were obtained for the computational analysis of **14**, with the optimized molecular structures presented in Figure 2.23, Figure 2.24, and Figure 2.25 below. The geometries obtained with and without the presence of THF in the metal coordination sphere are strikingly different, as both **14b** and **14c** adopt an octahedral geometry, whereas **14a** conforms to a distorted trigonal bipyramidal geometry. As observed in the lutetium analogue **12**, attempts to optimize a structure of **14** with two coordinated THF atoms was not successful, as only one molecule of THF is within the coordination sphere of **14c**. This is likely again an artifact of the steric pressure imposed by the ligand framework.

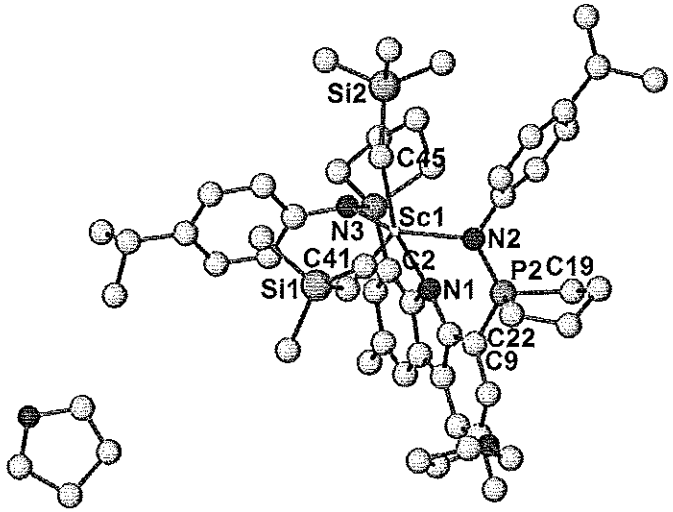

Figure 2.23 Molecular representation of $L_1^{Dipp}Sc(CH_2SiMe_3)_2$ (**14a**) with two free THF molecules. H atoms have been omitted for clarity.

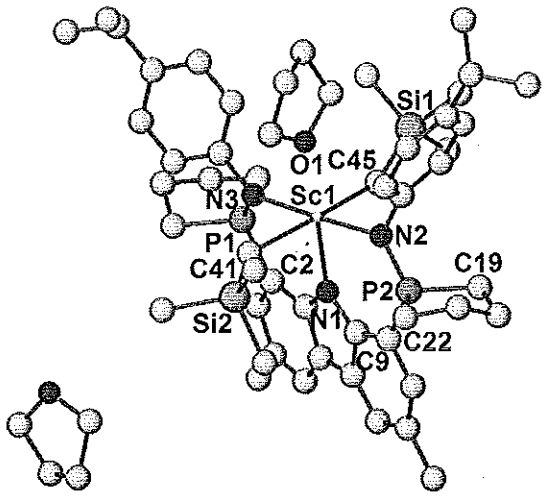

Figure 2.24 Molecular representation of $L_1^{Pipp}Sc(CH_2SiMe_3)_2$ (**14b**) with one coordinated and one free THF molecule. H atoms have been omitted for clarity.

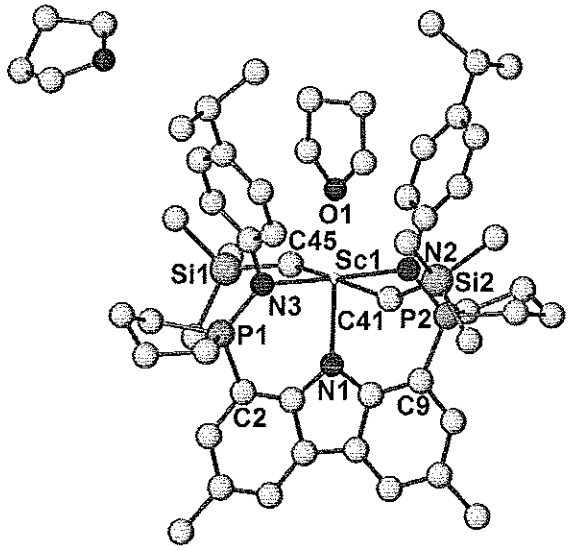

Figure 2.25 Molecular representation of $L_1^{Pipp}Sc(CH_2SiMe_3)_2$ (**14c**), whereby the starting. approximation included two coordinated THF molecules. H atoms have been omitted for clarity.

Relative energies were determined in the same manner described for **12**, aside from the change in pseudopotential (ECP10MDF) and basis set that correspond to scandium. These values, which are presented in Table 2.9, conclude

that again, the lowest energy complex is that which is not coordinated to THF (**14a**). This finding coincides with that observed spectroscopically.

Table 2.9 Relative energies of the different geometry optimizations of compound **14**.

Complex	Relative Energy ($kJ \cdot mol^{-1}$)
14a	0.000
14b	42.071
14c	38.625

Select bond lengths and angles for **14a** are displayed in Table 2.10. As expected, the Sc–N and Sc–C bond lengths are shorter than that observed for lutetium, and is due to the smaller ionic radius of scandium (Sc = 0.745 Å; Lu = 0.861 Å).[102] These values for Sc–N and Sc–C bond lengths also correspond to those found in the literature.[53,58] In comparing the ligand structures of **12a** and **14a**, no significant deviations are observed. The largest structural difference is noted at the metal centre, where **12a** adopts a distorted square pyramidal geometry in contrast to the trigonal bipyramidal geometry observed for **14a**. Such a drastic change in geometry can again be contributed to the differences in ionic radii between scandium and lutetium. As the ionic radius of scandium is smaller, increased steric pressure from the ligand scaffold occurs. This forces one of the $SiMe_3$ groups to become situated directly above the binding pocket.

Table 2.10 Select bond lengths (Å) and angles (°) of the computationally determined molecular structure of **14a**.

Bond Lengths (Å)		Bond Angles (°)		Torsion Angles (°)	
N_1–Sc_1	2.376	C_2–P_1–N_3	112.26	C_1–C_2–P_1–N_3	–44.3
N_2–Sc_1	2.243	C_9–P_2–N_2	111.56	C_8–C_9–P_2–N_2	28.9
N_3–Sc_1	2.257	N_1–Sc_1–C_{41}	95.59	C_2–P_1–N_3–C_{23}	–82.6
C_2–P_1	1.792	C_{41}–Sc_1–C_{45}	104.92	C_9–P_2–N_2–C_{32}	–163.6
C_9–P_2	1.789	N_1–Sc_1–C_{45}	159.48		
Sc_1–C_{41}	2.212	N_2–Sc_1–N_3	147.40		
Sc_1–C_{45}	2.247				

2.7 Conclusions

The synthesis and characterization of a new pincer ligand containing phospholane rings has been achieved and its protonolysis reactivity explored. Unfortunately, inclusion of the phospholane moieties in an attempt to prevent undesirable metalative reactivity was not successful. For both of the investigated dialkyl rare earth compounds, cyclometalation was observed, though at a slower rate in comparison to the previously studied diphenylphosphine systems. This suggests greater stability of the resulting dialkyl compounds, and is most likely attributed to enhanced electron donation to the metal centre in the presence of the phospholanes. Most interestingly, intramolecular C–H bond activation of **12** and **14** occurs *via* two different proton sources, the *N*-aryl ring and phospholane, respectively. Differences in ionic radii between lutetium and scandium are believed to contribute to this difference. Thermal instability of the rare earth dialkyl complexes prevented solid-state characterization, but elucidation of their presence, structure, and their respective decomposition products was achieved using

multinuclear NMR spectroscopy and computational chemistry techniques. Computational analysis revealed that THF does not interact with the Lu or Sc atom in the complexes $L_1^{Pipp}Lu(CH_2SiMe_3)_2$ and $L_1^{Pipp}Sc(CH_2SiMe_3)_2$, whereby THF coordination in fact results in a higher energy complex for both compounds.

Chapter 3

Beyond Phosphinimines: The Incorporation of Pyrazole Functionalities

3.1 Overview

As mentioned in Chapter 1, the hard, Lewis acidic nature of the lanthanide metals often require hard, electron-donating atoms for stabilization. Satisfaction of these conditions has been heavily pursued through the incorporation of nitrogen containing moieties. Presented in Chapter 2 was a bis(phosphinimine)carbazole ancillary (**11**) designed to meet these requirements. However, the steric bulk of **11** resulted in thermal decomposition *via* intramolecular C–H bond activation of the dialkyl lanthanide complexes supported by this framework. To circumvent this undesirable reactivity and synthesize organometallic lanthanide complexes with enhanced thermal stability, ligand systems with reduced steric bulk were pursued. Of particular interest to this chapter are constrained, or cyclic nitrogen containing functionalities, as they should allow greater geometrical control with respect to the

metal centre while reducing steric crowding. In addition, the extreme rigidity of the N-heterocyclic functional groups is expected to render them less likely to participate in intramolecular cyclometalation.

Reviewed below are select literature examples of N-heterocyclic containing pincer ligands employed in both transition metal and organolanthanide chemistry. The objective of this review is to provide rationale to the reader for the evolution of a new breed of ligand, and the focus of this chapter: 1,8-bis(3,5-dimethyl-pyrazolyl)-3,6-dimethyl-carbazole (CzPzMe).

3.1.1 N-Heterocyclic Containing Ligands

Oxazoline containing pincer ligands have been influential in the development of transition metal chemistry. Namely, their tunability at the 2-position has allowed for the development of chiral ligands, an important feature for enantioselective catalytic processes. The oxazoline imine nitrogen renders the ligand useful for use with an array of metals as it provides electron donation through the nitrogen lone pair in addition to modest chemical hardness. These properties, in combination with the success of oxazoline-containing ligands in transition metal chemistry, has witnessed the adaptation of oxazoline-based scaffolds to organolanthanide chemistry.[119]

With respect to organometallic rare earth chemistry, the pybox (pyridine-bis(oxazoline)) ligand has been used extensively since the early 2000's.[119-127] As shown in Figure 3.1, pybox is a neutral scaffold that offers electron donation *via* both the pyridine and imine nitrogen atoms. In addition, the overall ligand is

extremely rigid, which can help to prevent undesirable intramolecular reactivity and fluxional behavior by providing a controlled coordination environment. Notably, this ligand does not enforce ideal geometries around the metal centre; due to a lack of steric saturation, lanthanide complexes of the pybox ligand with unusually high coordination numbers (e.g. 7-9) are often observed.[119] These coordination numbers are typically facilitated by the chelation of two pybox ligands in κ^3 coordination modes, as well as by retention of Lewis bases as ligands (Figure 3.2).[120-123]

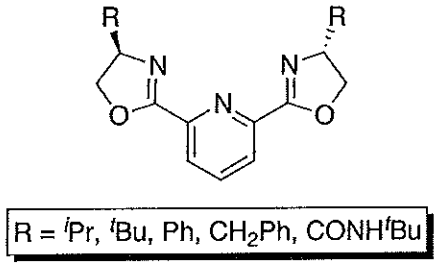

Figure 3.1 Generic pybox ligand scaffold.

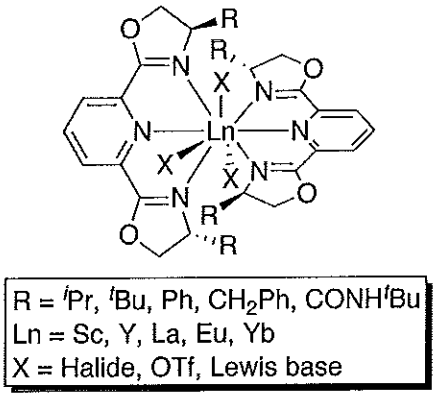

Figure 3.2 Pybox supported rare earth dimer.

High coordinate metal complexes of the pybox ligand have been found to exhibit useful small molecule reactivity. For example, enantioselective processes

such as silylcyanation of aldehydes boasts yields up to 98% with an enantiomeric excess (ee) of 91% (Scheme 3.1).[120-121]

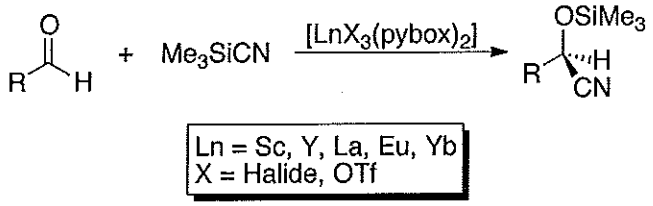

Scheme 3.1 Generic silylcyanation of an aldehyde catalyzed by a pybox supported Ln complex.

Similar in structure to the previously discussed β-diketiminate ligand is the bis(oxazolinyl)methane (BoxH) ligand (Figure 3.3, **A**), whereby two oxazoline rings are bridged by either a CH_2, CMe_2, or CHMe linker. Of particular value are derivatives containing either CH_2 or CHMe functionalities, as they can be readily deprotonated to generate the corresponding monoanionic ligand (Box^-) (Figure 3.3, **B**) that exhibits a comparable binding motif to that of nacnac.[119]

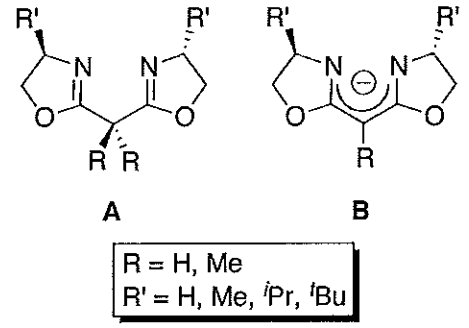

Figure 3.3 Bis(oxazolinyl)methane ligand (**A**) and monoanionic bis(oxazolinato)methane ligand (**B**).

While organolanthanide complexes supported by the neutral bis(oxazoline) ligand have seldom been observed, the monoanionic derivative has proven useful for supporting an array of lanthanide compounds. Work performed by both Marks

and Anwander demonstrated that alkane/amine elimination between the protonated bis(oxazolinyl)methane ligand and tris(alkyl/amine)lanthanide complexes yields well-behaved lanthanide dialkyl/amido species supported by the Box ligand (Scheme 3.2).[128-129] The resultant lanthanide complexes exhibit a distorted tetrahedral geometry at the metal centre, with no Lewis base retention observed.

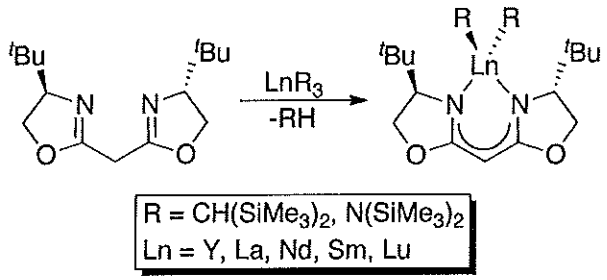

Scheme 3.2 Reactivity of BoxH ligand with tris(alkyl/amido)lanthanide compounds.

Enantioselective hydroamination of aminoalkenes was investigated using the aforementioned lanthanide diamide compounds (Scheme 3.3). The formation of chiral heterocycles was achieved, with conversions greater than 98% and ee's of up to 67%, with specific results dependent on the lanthanide metal employed.[128]

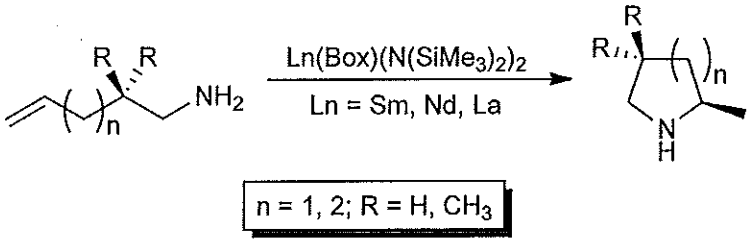

Scheme 3.3 Hydroamination of aminoalkenes *via* a Box supported lanthanide catalyst.

In more recent work, Berg *et al.* employed a carbazole based bis(oxazoline)carbazolide system for supporting the rare earths.[130] This

monoanionic ligand, which was originally introduced by the Nakada group for supporting Cr^{2+} catalysts used in C–C bond formation,[131] resulted in the synthesis of 5-coordinate lanthanide dialkyl complexes. The polymerization activity of these compounds on substrates including ethylene, isoprene, and 2,3-dimethylbutadiene were examined, but little to no activity was observed.[130]

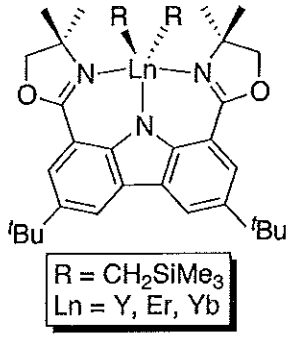

Figure 3.4 Carbazole based bis(oxazoline) supported lanthanide complexes.

Due to the fact that chiral oxazoline rings are relatively facile to prepare, they are of particular interest for use in ligand systems that support metal complexes for use in asymmetric catalysis. For applications other than asymmetric catalysis, a popular alternative to oxazoline-based ligands is pyrazole-containing frameworks. Pyrazole, in contrast to oxazoline, contains two electron-rich nitrogen atoms, allowing for enhanced electron donation upon metal chelation. Additionally, pyrazole rings are aromatic and planar, which can influence the steric environment around a metal centre. Of pyrazole containing ligands within the literature, the most influential class to date with respect to lanthanide chemistry is the hydrotris(pyrazolyl)borate ligands, commonly referred to as scorpionate or Tp (Figure 3.5), which first made an appearance in *f* element chemistry over 40 years ago.[132-136] Originally developed by Trofimenko,[136] scorpionate ligands are ideal for

lanthanide chemistry due to the ease of tunability at both the 3 and 5 positions of pyrazole. Such variability allows for greater control over metal coordination while maintaining proper steric and electronic saturation to prevent unwanted reactivity.[132]

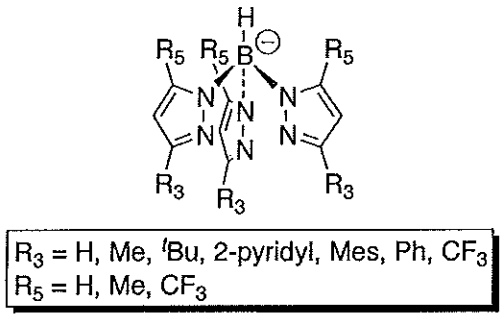

Figure 3.5 Generic scorpionate (Tp) ligand.

Formation of lanthanide dihalide complexes can be readily achieved *via* salt metathesis routes (Scheme 3.4), in which tris and bis Tp analogues are most prevalent, yielding lanthanide complexes with extremely high coordination numbers.[132,137] The coordination environment is reflective of the flexibility within the ligand scaffold, thus reducing control of the geometry at the lanthanide. Attempts to prepare mono Tp derivatives have been investigated, though ligand redistribution is often observed due to lack of steric saturation at the metal centre. Incorporation of bulky substituents at R_3 appears to alleviate the formation of poly-Tp compounds.[138] In addition, increased steric bulk allows for an alternate synthetic pathway, protonolysis, which generates lanthanide dialkyl compounds (Scheme 3.5).[139]

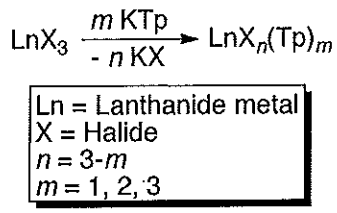

Scheme 3.4 Synthesis of LnTp complexes *via* salt metathesis.

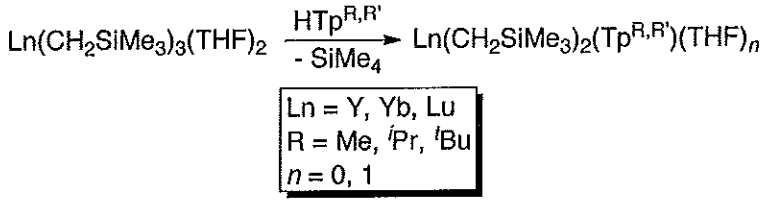

Scheme 3.5 Preparation of Tp Ln complexes *via* protonolysis.

Systems containing pyrazole that demonstrate enhanced ligand rigidity have been recently explored, but explicitly in transition metal chemistry. Most notable is the di(2-pyrazolyl-aryl)amine ligand, which exhibits a tridentate bonding motif that coordinates the metal centre in a κ^3 fashion (Figure 3.6).[140-142] Tunability at the 3-position on pyrazole (denoted R, Figure 3.6) has been shown to have a noticeable inductive effect on rhodium(III), whereby greater electron richness at Rh was directly correlated to increasing donor capacity of R (H < Me < ^{i}Pr).[142] Rates of oxidative addition, however, showed opposite effects, in which increasing steric bulk decreased overall rate of reaction of the rhodium(III) compounds.[142]

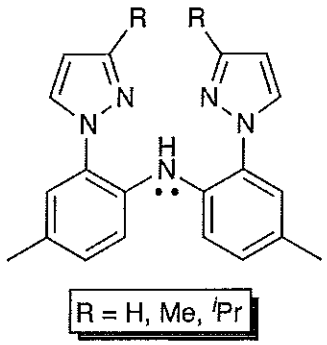

Figure 3.6 Structure of the di(2-pyrazolyl-aryl)amine ligand.

3.2 Ligand Design

3.2.1 Structural Features

Maintaining the ideology of a tridentate nitrogenous binding motif presented in Chapter 2, a carbazole based ancillary bearing pyrazole functionalities at the 1,8-positions was pursued (CzPz) (Figure 3.7). Carbazole, as previously discussed, is extremely rigid, as are the pyrazole rings. Combined, the two are anticipated to greatly decrease fluxional ligand behavior, with only minimal rotation of the C–N bond expected as it has fewer degrees of freedom compared to the phosphinimine ligand **11**. In addition, this rigidity will allow for greater control of the coordination geometry at the metal centre. From an electronic standpoint, the pyrazole and carbazole nitrogen atoms will offer substantial electron donation to the relatively Lewis acidic lanthanide centre. The amount of electronic donation can readily be tailored to meet the respective metal's needs by modifying the functional group at the 3-position on pyrazole, denoted as R in Figure 3.7. Previous work with transition

metals has shown that increasing the donor capacity at this position on pyrazole results in heightened electron richness at the metal centre.[142]

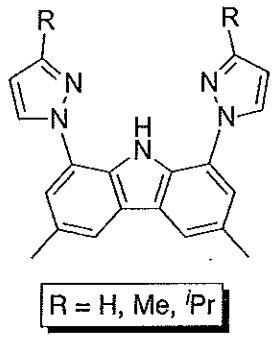

Figure 3.7 Proposed CzPz ligand for organolanthanide chemistry.

Compared to the phosphinimine ligand (**11**), the pyrazole groups offer less steric saturation. In particular, a reduction in steric bulk out of the carbazole plane is to be expected. This reduction may be beneficial, as it is expected to reduce the propensity for intramolecular C–H bond activation previously observed for ligands **1** and **11** by making it difficult to obtain the 4-centred transition state required for σ-bond metathesis. In addition, there is a reduced number of C–H bonds available for metalation. However, it may not provide sufficient steric saturation to avoid problems such as dimerization.

3.2.2 Ligand Synthesis

In comparison to the preparation of **11**, which consists of 7 synthetic steps, CzPz can be prepared in a mere 4 steps from commercially available starting materials. Of these steps, the first 3 for both syntheses are identical, a feature that is beneficial from efficiency and practicality standpoints. Therefore, starting from the

chemical precursor 1,8-dibromo-3,6-dimethyl-9H-carbazole, the CzPz ligand can be generated by installation of pyrazole rings at the 1,8-positions of dimethylcarbazole by an Ullman coupling reaction. This work specifically describes the preparation of a CzPz ligand whereby the pyrazole rings are substituted at the 3-position with methyl groups (CzPzMe). It is important to note that this synthetic approach, however, can be readily extended to other pyrazole systems. Thus, the preparation of CzPzMe was achieved by the Ullmann coupling reaction of 1,8-dibromo-3,6-dimethyl-9H-carbazole with commercially available 3-methylpyrazole to yield compound **17** (Scheme 3.6) as a yellow powder in 13.50% yield.

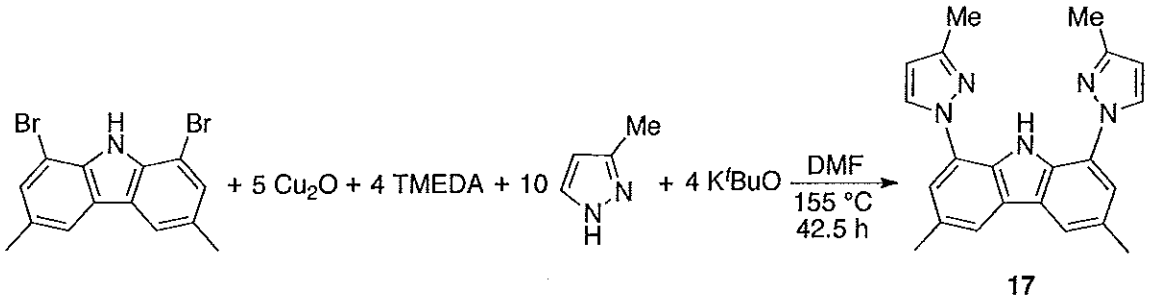

17

Scheme 3.6 Synthesis of **17** using an Ullmann coupling reaction.

Ullmann coupling reactions are copper catalyzed transformations that often require harsh thermal conditions, and are classically employed for the formation of C–C bonds between two aryl compounds. The mechanism of this process is still debated, but two popular arguments, the radical mechanism and aryl-copper intermediate mechanism, have been predominant within the literature.[143-145] For the formation of C–N bonds, even less is known regarding the reaction mechanism, and the mechanism is believed to be dependent on reaction conditions.[146] However, it is speculated that a concerted oxidative addition,[147-148] or radical mechanism[149] is

a plausible dominant pathway. To date, research regarding Ullman coupling reactions is still being pursued to gain further understanding of the mechanistic processes, as well as to enhance the reaction's overall efficiency.[145-149]

A variety of reaction conditions were tested in the synthesis of compound **17**, with those presented in Scheme 3.6 providing the cleanest conversion to the desired ligand. A mechanism supporting the rationale outlined below is provided in Scheme 3.7. In choosing the catalyst, copper(I) oxide was utilized because copper(I) salts have been shown to provide the highest reaction rates in Ullmann coupling reactions.[145] The use of catalytic copper(I) bromide was also investigated, as regeneration of CuBr is anticipated to accompany formation of the C–N bond. However, the reaction did not proceed cleanly in the presence of CuBr, as minimal product (**17**), starting material, and additional side reactants were all present within the reaction mixture. Notably, Cu_2O is not regenerated in the reaction and must therefore be used in stoichiometric quantities. In fact, an excess of Cu_2O was used to drive the reaction to completion, forming compound **17**. For the coupling reaction to take place, the presence of base is required for deprotonation, yielding the Cu–N intermediate. Based on similar systems within the literature, both K_2CO_3 and K^{t}BuO are frequently used, and their effects on reactivity are dependent on the substrate.[150-151] As such, both bases were tested in the synthesis of **17**, with the stronger of the two bases (K^{t}BuO) resulting in cleaner conversion to the desired ligand. The presence of tetramethylethylenediamine (TMEDA) in the reaction mixture is required to ligate the resultant copper nitrogen species upon formation.

Finally, dimethylformamide (DMF) was employed as the solvent as it has a high boiling point (153 °C) and easily dissolves the inorganic salts Cu_2O and K^tBuO.[151]

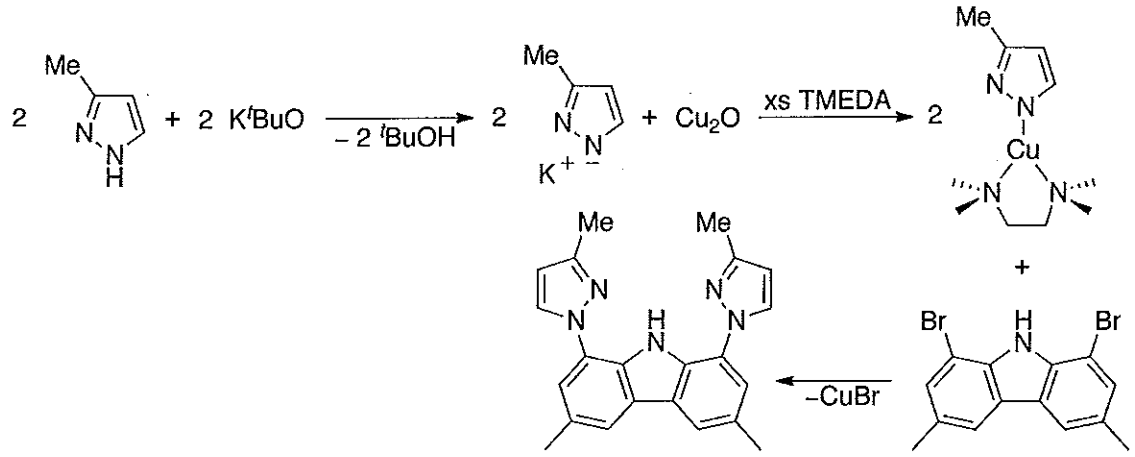

Scheme 3.7 Proposed synthetic pathway for the generation of **17** using an Ullmann coupling reaction.

Due to the conditions of the Ullmann coupling reaction, copper salts are a substantial byproduct of the synthesis. Isolation of **17** from these copper salts is therefore critical for subsequent chemistry, and can be achieved *via* numerous methods. Initial attempts involved separation by flash silica column chromatography using a 1:1 eluant of hexanes:ethyl acetate. This method resulted in pure product, but overall poor yields. In addition, attempts to increase yields required additional eluent, which caused copper salts to travel through the column and contaminate the final product. Compound **17** can also be purified using sublimation at 170 °C under dynamic vacuum. However, at these extreme temperatures, loss of pyrazole was noted spectroscopically, and again poor yields were obtained. Instead, ligation of the copper salts in the presence of a saturated ammonium chloride solution proved to be the most efficient method of purification.

Following an aqueous work up with $NH_4Cl_{(aq)}$, compound **17** can again be reconstituted in a 1:1 ratio of hexanes:ethyl acetate and filtered through silica.

Upon isolation of ligand **17**, characterization by multinuclear NMR spectroscopy was performed. In the ^1H NMR spectrum, the diagnostic pyrazole protons appear as doublets at δ 8.03 and 6.34 ppm, with $^3J_{HH}$ = 2.4 Hz. The resonances of the pyrazole methyl and carbazole methyl moieties appear at δ 2.59 and 2.55, respectively, as determined by 2D heteronuclear HSQC experiments.

Single crystals of **17** were obtained from a concentrated ethyl acetate solution at ambient temperature. The resulting yellow plates crystallized in the orthorhombic space group *Pbca*, with 8 molecules occupying the unit cell. Residual electron density is evident in the final crystal structure (sum of peak/hole density > 1), and can be located in close proximity to the carbazole-methyl group. This residual electron density may be attributed to poor crystal quality. Nonetheless, the final structure, represented in Figure 3.8, unambiguously supports the connectivity of compound **17**. The molecular structure of compound **17** shows that in the solid state the pyrazole functionalities lay within the same plane as the carbazole backbone, resulting in the desired decrease of peripheral steric bulk at the NH binding pocket. This planarity also reinforces the high symmetry of the scaffold.

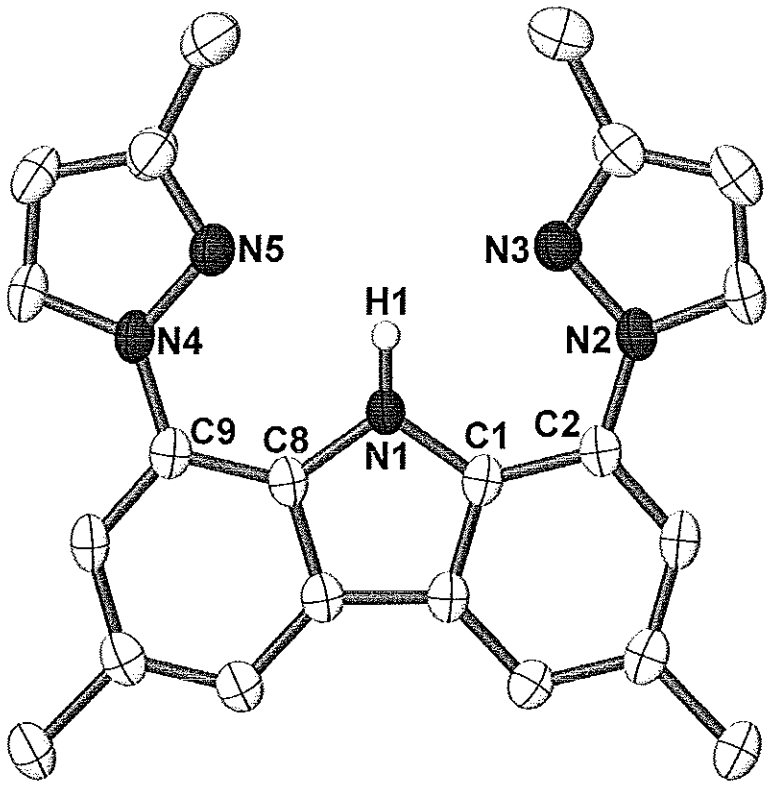

Figure 3.8 Molecular structure of ligand **17** represented by 50% probability thermal ellipsoids. Hydrogen atoms, excluding H1, have been omitted for clarity.

Select bond lengths and angles of **17** are presented in Table 3.1. As represented by the torsion angles for C_1–C_2–N_2–N_3 and C_8–C_9–N_4–N_5, the pyrazole moieties and carbazole deviate somewhat from coplanarity (–6.6(4)° and –10.5(4)°, respectively). The chelate angle represented by C_2–N_2–N_3 (120.8(3)°) and C_9–N_4–N_5 (120.6(3)°) is also significantly larger than the comparable C–P–N angle found in the phosphinimine system **11** (by ~16-19°) (see Table 2.2). This increase in chelate angle is attributed to the geometry and rigidity imposed by the pyrazole rings. An increase of this magnitude was expected to aid in reducing steric pressure at the metal centre, hopefully preventing unwanted intramolecular cyclometalation from occurring.

Table 3.1 Select bond lengths (Å) and angles (°) of HL_2^{Me} (**17**).

Bond Lengths (Å)		Bond Angles (°)		Torsion Angles (°)	
N_2–C_2	1.416(4)	C_2–N_2–N_3	120.8(3)	C_1–C_2–N_2–N_3	–6.6(4)
N_4–C_9	1.415(4)	C_9–N_4–N_5	120.6(3)	C_8–C_9–N_4–N_5	–10.5(5)
N_4–N_5	1.372(4)	C_1–C_2–N_2	120.8(3)	C_2–N_2–N_3–C_{15}	178.3(3)
N_2–N_3	1.367(4)	C_8–C_9–N_4	121.1(3)	C_9–N_4–N_5–C_{19}	179.3(3)

3.3 Metal complexation

To serve as a direct comparison to previous work performed in this thesis, as well as the Hayes group, the formation of dialkyl lanthanide compounds *via* alkane metathesis between HL_2^{Me} and $Ln(CH_2SiMe_3)_3(THF)_2$ (Ln = Sc, Lu, Y) was pursued. This consistency allowed for thorough analysis of the changes the new ligand system has on the desired dialkyl species.

3.3.1 Synthesis of $L_2^{Me}Lu(CH_2SiMe_3)_2$ (18)

Formation of $L_2^{Me}Lu(CH_2SiMe_3)_2$ (**18**) was achieved by the facile alkane elimination reaction of HL_2^{Me} with $Lu(CH_2SiMe_3)_3(THF)_2$ (Scheme 3.8).

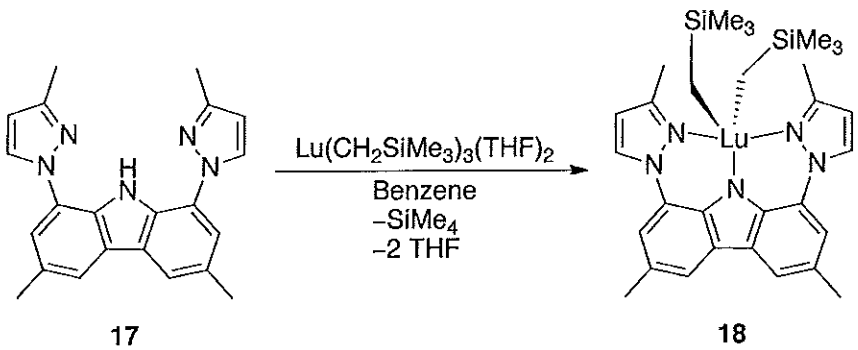

Scheme 3.8 Synthesis of $L_2^{Me}Lu(CH_2SiMe_3)_2$ (**18**).

Complex **18** has proven to be thermally stable at ambient temperature in both the solid and solution states. Even more significantly, heating a benzene-d_6 solution of **18** to 75 °C for a period of 24 hours resulted in no decomposition observed spectroscopically. However, when left at this temperature over a more extended period of time (72 hours), complete decomposition of **18** was noted. Comparable carbazole systems **2** and **12** would have exhibited significant decomposition after this extended time period, even at ambient conditions. Therefore, such stability was a remarkable achievement.

In addition to enhanced thermal stability, complex **18** can be isolated as a base-free, orange solid (yield: 73.7%). Removal of benzene under vacuum to isolate the expected dialkyl complex resulted in the loss of THF from the reaction mixture, demonstrating that THF coordination is not required for the stability of **18**. This is in stark contrast to that observed for $L_1^{Pipp}Lu(CH_2SiMe_3)_2$, where removal of the solvent and residual THF prompted rapid decomposition.

Compound **18** was fully characterized using multinuclear NMR spectroscopy in benzene-d_6. Remarkably, upon metal complexation the methyl moieties for both the pyrazole and carbazole functionalities shift from almost overlapping singlets (δ 2.59 and 2.55, respectively), to δ 2.76 and 2.41, respectively. The Lu methylene groups appear as a singlet at δ –0.30, which is in close proximity to the $Si(CH_3)_3$ resonance at δ –0.23.

*3.3.2 Synthesis of $L_2^{Me}Sc(CH_2SiMe_3)_2$ (**19**)*

Similar to the synthesis presented for **18**, the scandium analogue was prepared by reacting a 1:1 ratio of HL_2^{Me} with $Sc(CH_2SiMe_3)_3(THF)_2$ (Scheme 3.9) in benzene at ambient temperature for 5 minutes. The formation of **19** was observed immediately when the reaction was followed *in situ* by NMR spectroscopy. Again, it was noted that the methyl group signals of both the pyrazole and carbazole shift drastically upon metal complexation, appearing as singlets at δ 2.85 and 2.41 in benzene-d_6, respectively. In comparison to $L_2^{Me}Lu(CH_2SiMe_3)_2$, the metal-methylene resonance appears significantly downfield, resonating at δ 0.35, a difference of almost 1 ppm. The $Si(CH_3)_3$ resonance is less affected, appearing at δ −0.34 in benzene-d_6.

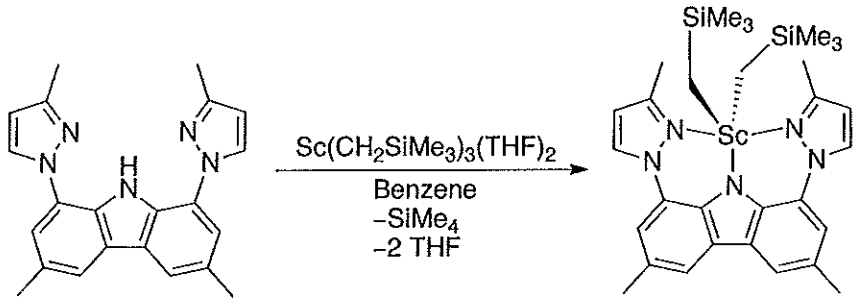

17 **19**

Scheme 3.9 Formation of **19** *via* alkane elimination.

As observed with the lutetium analogue, compound **19** was readily isolated as a base-free orange solid in high yield (86.70%) In addition, the THF-free compound also exhibits prolonged thermal stability at ambient temperature, where no decomposition was noted in either the solid or solution state after 60 hours. Even at elevated temperatures (75 °C) compound **19** remained pure after a period of 24 hours.

3.3.1 *In situ* Formation of $L_2^{Me}Y(CH_2SiMe_3)_2$ (**20**)

In accordance to the preparation of the Sc and Lu complexes of the CzPzMe ligand (**18** and **19**, respectively), an yttrium dialkyl complex was prepared by the alkane elimination reaction of HL_2^{Me} with $Y(CH_2SiMe_3)_3(THF)_2$. When this transformation was monitored *in situ* by ^1H NMR spectroscopy in benzene-d_6, the reaction proceeded as expected to generate compound **20** ($L_2^{Me}Y(CH_2SiMe_3)_2$), with concomitant loss of one equivalent of $SiMe_4$ (Scheme 3.10). Due to the nuclear spin and abundance of yttrium (^{89}Y = 100% abundant, I = ½), diagnostic coupling between yttrium and the methylene carbon and hydrogen atoms of the $-CH_2SiMe_3$ group were readily observed spectroscopically. In the ^1H NMR spectrum (benzene-d_6) of **20**, the Y–CH_2 resonance appeared as a doublet at δ −0.14 ($^2J_{HY}$ = 2.7 Hz), which is only slightly downfield from the $SiMe_3$ signal at δ −0.18. Likewise, in the $^{13}C\{^1H\}$ NMR spectrum (benzene-d_6) of **20**, the methylene carbon appeared as a doublet at δ 35.8 ($^1J_{CY}$ = 38.6 Hz). The observed coupling constants between yttrium and the alkyl methylene hydrogen and carbon nuclei are comparable to others reported in the literature.[53,90,101,152]

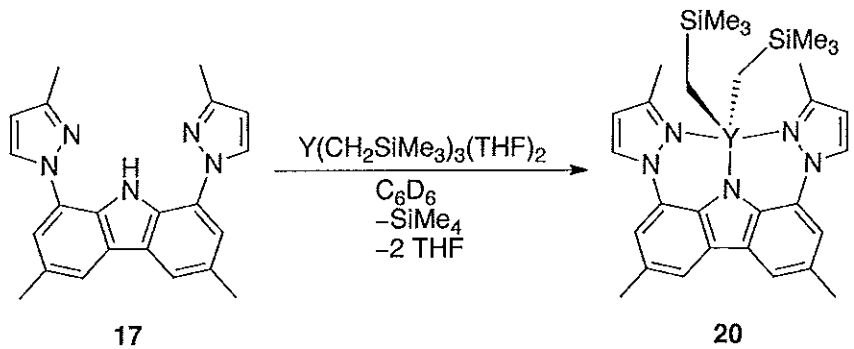

17 **20**

Scheme 3.10 *In situ* formation of **20**.

The stability of the CzPzMe yttrium dialkyl complex was monitored by ^{1}H NMR spectroscopy over a period of 48 hours. Notably, after the first 24 hours at ambient temperature, no significant decomposition of the complex was evident spectroscopically. However, a small amount of yellow precipitate was noticed at this time. After 48 hours at ambient temperature, a substantial amount of precipitate was observed in the reaction vessel, and spectroscopic analysis indicated no evidence that the initial metal complex **20** remained in solution. While chemical conversion of **20** is not ideal, the slow rate for this unknown transformation should still allow for rich metal chemistry to be explored upon *in situ* formation of the dialkyl.

In an attempt to enhance the stability of $L_2^{Me}Y(CH_2SiMe_3)_2$, the reaction was repeated in tetrahydrofuran-d_8 and monitored *in situ*. It was expected that in the presence of an excess of tetrahydrofuran-d_8, the Lewis basic solvent would coordinatively saturate, and therefore, stabilize the complex. Unfortunately, the addition of tetrahydrofuran-d_8 only increased the rate of decomposition, with complete decomposition observed in 4 hours at ambient temperature.

This difference in stability between compounds **18**, **19**, and **20** is most likely attributed to the size of the metal centre. Yttrium in the +3 oxidation state possesses a larger ionic radius than the respective scandium or lutetium cations (Y = 0.900 Å; Sc = 0.745 Å; Lu = 0.861 Å).[102] As such, the CzPzMe ligand may not be sufficiently sterically demanding to prevent all unwanted side reactions from occurring in solution. Using this principle, plausible undesirable reaction pathways for **20** might include dimerization, which in turn would explain the observed decrease in

solubility. An option for possibly preventing this reactivity is to increase the steric bulk of the ligand, in particular at the 3-position on pyrazole. Incorporation of a more sterically cumbersome functionality, such as *iso*propyl (CzPz^{i}Pr), *tert*-butyl (CzPz^{t}Bu), or phenyl (CzPzPh), might generate a better framework for Y.

3.4 Computational Analysis of HL_2^{Me} and Associated Metal Complexes

While the Sc, Lu and Y metal complexes discussed above were fully characterized by multinuclear NMR spectroscopy, a lack of crystallinity of the compounds precluded their structural determination by single-crystal X-ray diffraction techniques. Therefore, as an alternative method, a computational analysis was performed in order to aid structural understanding of these metal species.

3.4.1 Computational Analysis of HL_2^{Me} (17)

Starting from the crystal structure of HL_2^{Me}, a geometry optimization was performed at the B3WP91/6-31G(d,p) level of theory, as per literature precedent.[153-157] Structural parameters of the optimized and crystallographic molecules were compared to determine the efficiency of the level of theory and basis set, with select bond lengths and angles of the computationally derived structure (Figure 3.9) presented in Table 3.2.

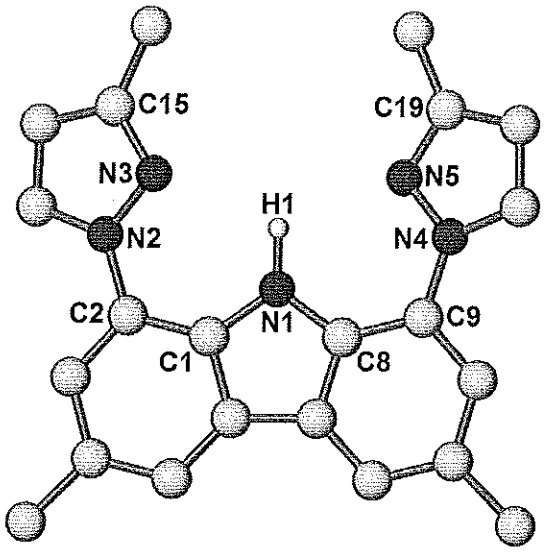

Figure 3.9 Molecular representation of HL_2^{Me} from computational geometry optimization at the B3WP91/6-31G(d,p) level of theory. Hydrogen atoms, excluding H_1, have been omitted for clarity.

Table 3.2 Select bond lengths (Å) and angles (°) from the geometry optimized structure of H L_2^{Me}.

Bond Lengths (Å)		Bond Angles (°)		Torsion Angles (°)	
Calculated Values					
N_2–C_2	1.413	C_2–N_2–N_3	120.52	C_1–C_2–N_2–N_3	–21.7
N_4–C_9	1.413	C_9–N_4–N_5	120.52	C_8–C_9–N_4–N_5	–21.7
N_4–N_5	1.354	C_1–C_2–N_2	121.24	C_2–N_2–N_3–C_{15}	–178.8
N_2–N_3	1.354	C_8–C_9–N_4	121.24	C_9–N_4–N_5–C_{19}	–178.8
Crystallographic Values					
N_2–C_2	1.416(4)	C_2–N_2–N_3	120.8(3)	C_1–C_2–N_2–N_3	–6.6(4)
N_4–C_9	1.415(4)	C_9–N_4–N_5	120.6(3)	C_8–C_9–N_4–N_5	–10.5(5)
N_4–N_5	1.372(4)	C_1–C_2–N_2	120.8(3)	C_2–N_2–N_3–C_{15}	178.3(3)
N_2–N_3	1.367(4)	C_8–C_9–N_4	121.1(3)	C_9–N_4–N_5–C_{19}	179.3(3)

As apparent from Table 3.2, the bond lengths and angles between the computationally determined ligand and solid-state structure are in good agreement. The only significant deviation is within the torsion angles of C_1–C_2–N_2–N_3 and C_8–C_9–N_4–N_5. This difference can be attributed to the calculations being performed in

solution, allowing for greater ligand fluxionality, and is therefore not as representative of structure obtained in the solid state.

*3.4.2 Computational Investigation of **18**, **19**, and **20***

Using the geometrically optimized structure of HL_2^{Me}, the metal complexes $L_2^{Me}Ln(CH_2SiMe_3)_2$ (Ln = Sc, Lu, Y) were generated by replacing H_1 with the respective Ln atom, whereby the resulting N–Ln bond distance was determined from the van der Waals radii. The alkyl groups were manually added using the Gaussian Gaussview software suite. The final optimized structures of **18**, **19**, and **20** are shown in Figure 3.10, Figure 3.11, and Figure 3.12, respectively. In each case, the atoms C, H, and N were optimized at the B3WP91/6-31G(d,p) level of theory, and the lanthanide atom was treated with the appropriate basis set and Stuttgart-Dresden effective core pseudopotential (ECP), that takes into account relativistic effects arising from the presence of the *f* orbitals.[118,158] Frequency calculations were performed at the same level of theory to ensure that an energy minima had been achieved on the potential energy surface.

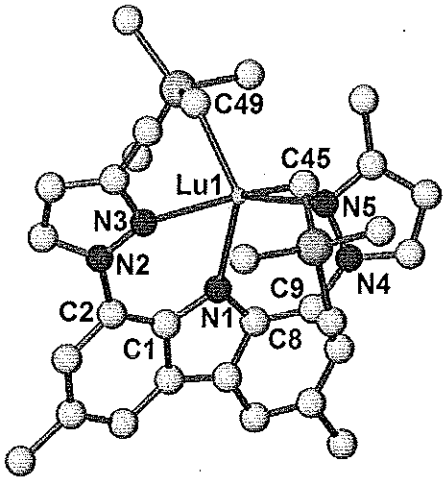

Figure 3.10 Geometry optimized structure of $L_2^{Me}Lu(CH_2SiMe_3)_2$ performed at the B3WP91/6-31G(d,p) level of theory.

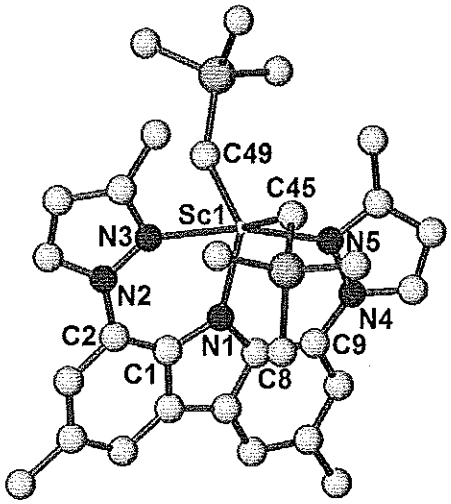

Figure 3.11 Molecular representation of $L_2^{Me}Sc(CH_2SiMe_3)_2$ from geometry optimization using B3WP91/6-31G(d,p).

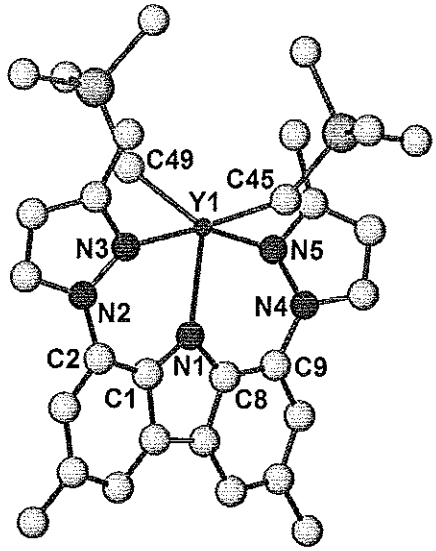

Figure 3.12 Molecular representation of $L_2^{Me}Y(CH_2SiMe_3)_2$ from geometry optimization using B3WP91/6-31G(d,p).

Presented in Table 3.3 are select bond lengths and angles for $L_2^{Me}Lu(CH_2SiMe_3)_2$. The geometry about the metal centre can be described as distorted trigonal bipyramidal, with C_{49} and C_{45} of the alkyl groups and N_1 of the carbazole backbone occupying the equatorial plane. The Lu-alkyl bond lengths are substantially similar at 2.388 Å (Lu_1–C_{45}) and 2.340 Å (Lu_1–C_{49}), and coincide well with values in the literature.[115] At 2.305 Å, the N_1–Lu_1 length is comparable to other Lu-ligated systems. Between the remaining nitrogenous bases (N_3–Lu_1: 2.440 Å; N_5–Lu_1: 2.440 Å), an increase in bond length was noted. An increase of this nature can potentially be explained by the increase in chelation angle induced by the strained geometry of the pyrazole groups, resulting in less steric interaction with the lutetium centre.

Metal complexation results in a slight distortion of the C_2–N_2–N_3–C_{15} and C_9–N_4–N_5–C_{19} torsion angles (–171.02 and –171.14°, respectively), which are reflective

of the planarity of pyrazole with respect to carbazole. This deviation is likely necessary for the ligand to accommodate the large lutetium centre. Conversely, the scandium analogue **19** exhibits torsion angles that closely resemble those in the computational structure of proteo ligand HL_2^{Me}, a fact that is attributed to the smaller ionic radius of scandium (Table 3.4).

Table 3.3 Bond lengths (Å) and angles (°) from the computationally determined molecular structure of **18**.

Bond Lengths (Å)		Bond Angles (°)		Torsion Angles (°)	
N_1–Lu_1	2.295	C_2–N_2–N_3	123.29	C_1–C_2–N_2–N_3	–31.7
N_3–Lu_1	2.440	C_9–N_4–N_5	123.29	C_8–C_9–N_4–N_5	–31.7
N_5–Lu_1	2.440	N_1–Lu_1–C_{45}	122.11	C_2–N_2–N_3–C_{15}	–170.5
C_2–N_2	1.423	C_{45}–Lu_1–C_{49}	115.78	C_9–N_4–N_5–C_{19}	–170.5
C_9–N_4	1.423	N_1–Lu_1–C_{49}	122.12		
Lu_1–C_{45}	2.380	N_3–Lu_1–N_5	159.94		
Lu_1–C_{49}	2.380				

Table 3.4 Select bond lengths (Å) and angles (°) of the computationally derived molecular structure of **19**.

Bond Lengths (Å)		Bond Angles (°)		Torsion Angles (°)	
N_1–Sc_1	2.142	C_2–N_2–N_3	123.31	C_1–C_2–N_2–N_3	–20.7
N_3–Sc_1	2.300	C_9–N_4–N_5	123.40	C_8–C_9–N_4–N_5	–23.4
N_5–Sc_1	2.311	N_1–Sc_1–C_{45}	120.70	C_2–N_2–N_3–C_{15}	–177.1
C_2–N_2	1.420	C_{45}–Sc_1–C_{49}	127.52	C_9–N_4–N_5–C_{19}	–175.4
C_9–N_4	1.420	N_1–Sc_1–C_{49}	111.77		
Sc_1–C_{45}	2.238	N_3–Sc_1–N_5	167.07		
Sc_1–C_{49}	2.236				

Also related to the smaller ionic radius of scandium are the calculated Sc_1–N and Sc_1–C bond lengths. These values coincide well with others reported in the literature, again with N_1 binding scandium more tightly than N_3 or N_5.[53,58] Again, a distorted trigonal bipyramidal geometry is displayed at the metal centre, in which the N_1–Sc_1–C_{49} presents the largest deviation from 120° (111.77°). In addition, the –

$SiMe_3$ moiety bound to C_{49} points upward and away from the carbazole backbone, which might coincide with the reduced N_1–Sc_1–C_{49} bond angle.

Table 3.5 Select bond lengths (Å) and angles (°) of the computationally derived molecular structure of **20**.

Bond Lengths (Å)		Bond Angles (°)		Torsion Angles (°)	
N_1–Y_1	2.313	C_2–N_2–N_3	122.94	C_1–C_2–N_2–N_3	–32.3
N_3–Y_1	2.455	C_9–N_4–N_5	123.28	C_8–C_9–N_4–N_5	–30.3
N_5–Y_1	2.457	N_1–Y_1–C_{45}	111.51	C_2–N_2–N_3–C_{15}	–170.6
C_2–N_2	1.423	C_{45}–Y_1–C_{49}	134.85	C_9–N_4–N_5–C_{19}	–170.9
C_9–N_4	1.424	N_1–Y_1–C_{49}	113.60		
Y_1–C_{45}	2.400	N_3–Y_1–N_5	159.00		
Y_1–C_{49}	2.409				

In contrast to both compounds **18** and **19**, both the –$SiMe_3$ functionalities of **20** point upwards and away from the ligand framework. This different conformation appears to have no noticeable effect on the Y_1–C bond lengths (2.400 and 2.409 Å, Table 3.5), which agree well with literature values. Increase in the C_{45}–Y_1–C_{49} bond angle compared to **18** and **19** is apparent however, which may provide greater accessibility to the yttrium centre. This steric void above yttrium might contribute to the decomposition of $L_2^{Me}Y(CH_2SiMe_3)_2$.

Though Y^{+3} has a larger ionic radius than Lu^{+3} (0.900 Å vs. 0.861 Å, respectively),[102] no significant change in the ligand torsion angles representative of the planarity between pyrazole and carbazole (Table 3.5) was observed. These similarities in ligand structure might be correlated to the widening of the C_{45}–Y_1–C_{49} angle, thus reducing steric pressure at the metal.

3.4.3 Probing Steric Bulk: Investigating Alternative CzPz Ancillaries

To gain further insight into the CzPz ligand scaffold and future metal complexes, alternative generations of ligand, namely CzPz^{i}Pr, CzPz^{t}Bu, and CzPzPh were investigated computationally. Through each generation, an increase of steric bulk was introduced into the system. The effects of an ever-increasing steric environment on dialkyl complexes of lutetium, scandium, and yttrium were examined computationally.

As in the previous calculations performed on CzPzMe and the respective metal complexes, all calculations were performed at the B3WP91/6-31G(d,p) level of theory. In the case of the metal complexes, the lanthanide centre was separately treated with the appropriate basis set and pseudopotential to account for the effective core pseudopotentials attributed to the *f* orbitals.

Starting with the crystal structure of **17**, the alternative functional groups (*iso*propyl, *tert*-butyl, and phenyl) were added in manually using the Gaussian software drawing suite. The geometry of the resultant ligands was allowed to freely optimize in benzene, yielding the computationally determined structures presented in Figure 3.13, Figure 3.14, and Figure 3.15. As is evident from the torsion angles presented in Table 3.6, the largest deviation of the pyrazole groups with respect to carbazole was observed with CzPzPh. Remarkably, only one of the pyrazole functionalities lays significantly out of the ligand plane (C_1–C_2–N_2–N_3: -48.1°) for CzPzPh, whereas the second pyrazole remains relatively planar (C_8–C_9–N_4–N_5: 15.5°). In addition, both pyrazole groups occupy the same plane with respect to the

carbazole backbone. The conformation of CzPzPh is similar to that observed for **1**, suggesting similar steric bulk between the two ligands. In the case of CzPz^{t}Bu, both pyrazole moieties rotate the same amount (C_1–C_2–N_2–N_3 and C_8–C_9–N_4–N_5: -35.7°), a value ~14° larger than that observed in the computationally determined CzPzMe. Finally, the computational model of CzPz^{i}Pr appears to be substantially similar to that found for CzPzMe. This is attributed to the methyl moieties on the *iso*propyl functionality pointing outwards of the binding pocket, reducing steric clash.

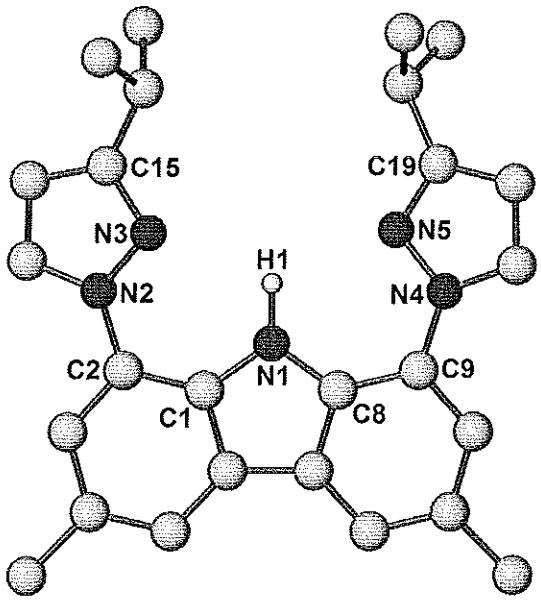

Figure 3.13 Computationally calculated molecular structure of CzPz^{i}Pr. Optimization was performed at the B3WP91/6-31G(d,p) level of theory.

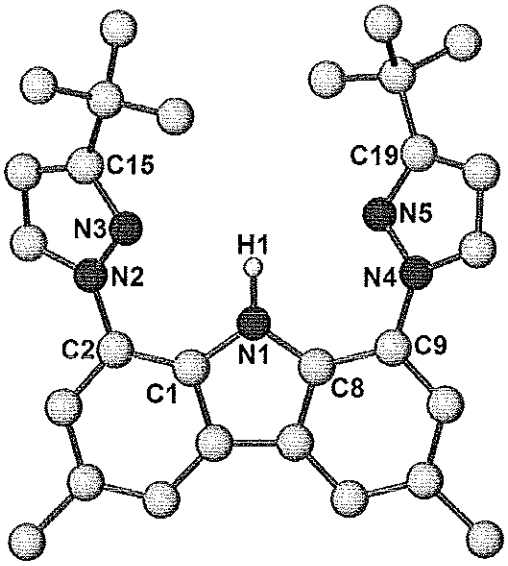

Figure 3.14 Computationally calculated molecular structure of CzPz^{t}Bu. Optimization was performed at the B3WP91/6-31G(d,p) level of theory.

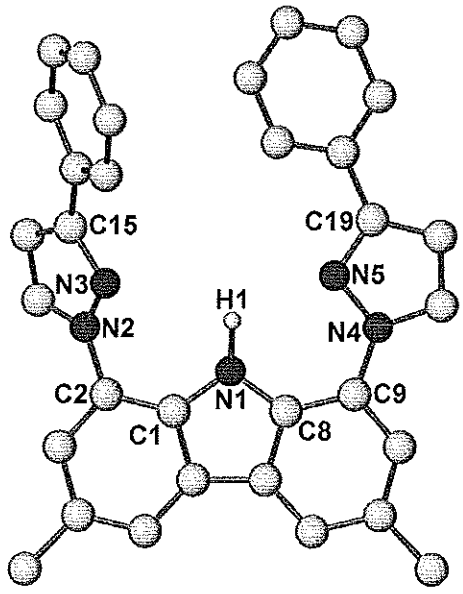

Figure 3.15 Computationally calculated molecular structure of CzPzPh. Optimization was performed at the B3WP91/6-31G(d,p) level of theory.

Table 3.6 Select bond lengths (Å) and angles (°) for the computationally determined structures of CzPz^{i}Pr, CzPz^{t}Bu, and CzPzPh.

Bond Lengths (Å)		Bond Angles (°)		Torsion Angles (°)	
		CzPz^{i}Pr			
N_2–C_2	1.413	C_2–N_2–N_3	120.64	C_1–C_2–N_2–N_3	–20.9
N_4–C_9	1.413	C_9–N_4–N_5	120.64	C_8–C_9–N_4–N_5	–20.9
N_4–N_5	1.356	C_1–C_2–N_2	121.42	C_2–N_2–N_3–C_{15}	–178.7
N_2–N_3	1.356	C_8–C_9–N_4	121.42	C_9–N_4–N_5–C_{19}	–178.7
		CzPz^{t}Bu			
N_2–C_2	1.413	C_2–N_2–N_3	120.60	C_1–C_2–N_2–N_3	–35.7
N_4–C_9	1.413	C_9–N_4–N_5	120.60	C_8–C_9–N_4–N_5	–35.7
N_4–N_5	1.356	C_1–C_2–N_2	121.45	C_2–N_2–N_3–C_{15}	–174.6
N_2–N_3	1.356	C_8–C_9–N_4	121.45	C_9–N_4–N_5–C_{19}	–174.6
		CzPzPh			
N_2–C_2	1.416	C_2–N_2–N_3	120.61	C_1–C_2–N_2–N_3	–48.1
N_4–C_9	1.413	C_9–N_4–N_5	121.07	C_8–C_9–N_4–N_5	15.5
N_4–N_5	1.349	C_1–C_2–N_2	121.64	C_2–N_2–N_3–C_{15}	–173.3
N_2–N_3	1.352	C_8–C_9–N_4	121.69	C_9–N_4–N_5–C_{19}	–177.9

3.4.4 Metal Complexes of Bulkier CzPz Analogues

Shown in Figure 3.16, Figure 3.17, and Figure 3.18 are the molecular structures of the lutetium, scandium, and yttrium dialkyls of CzPz^{i}Pr, respectively.

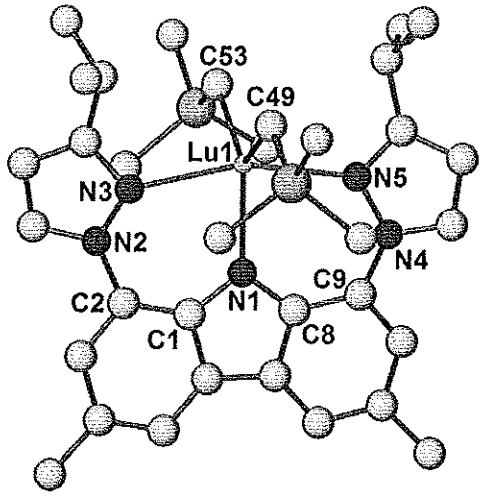

Figure 3.16 Molecular representation of $CzPz^{i}PrLu(CH_2SiMe_3)_2$ from geometry optimization using B3WP91/6-31G(d,p).

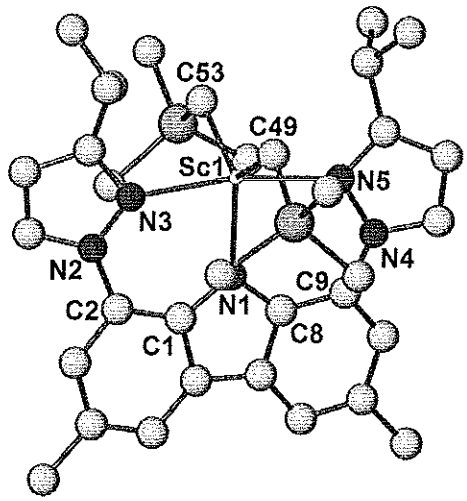

Figure 3.17 Molecular representation of $CzPz^{i}PrSc(CH_2SiMe_3)_2$ from geometry optimization using B3WP91/6-31G(d,p).

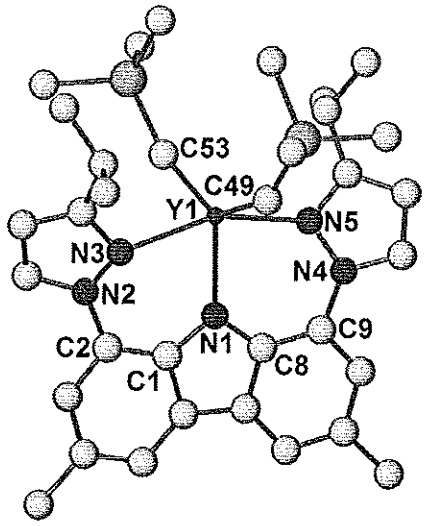

Figure 3.18 Molecular representation of CzPz^{i}PrY(CH_2SiMe_3)$_2$ from geometry optimization using B3WP91/6-31G(d,p).

Bond lengths and angles for the CzPz^{i}Pr rare earth complexes can be found in Table 3.7. The values presented in Table 3.7 are not substantially different from those determined for the 3-methylpyrazole lanthanide analogues. The most significant change in the ligand framework was observed in the torsion angles for C_1–C_2–N_2–N_3 and C_8–C_9–N_4–N_5. With respect to lutetium, these torsion angles decrease slightly from $L_2^{Me}Lu(CH_2SiMe_3)_2$ (–32.2° and –31.8°). Alternatively, an increase in torsion angle was noted for the scandium (**19**: –20.7° and –23.4°) and yttrium (**20**: –32.3° and –30.3°) complexes.

Notably, the presence of the *iso*propyl groups forces the $SiMe_3$ functionalities to adopt a more linear conformation. This is likely due to enhanced steric and electronic pressure from the *iso*propyl moieties.

Table 3.7 Select bond lengths (Å) and angles (°) for computationally derived CzPz^{i}Pr lanthanide complexes.

Bond Lengths (Å)		Bond Angles (°)		Torsion Angles (°)	
CzPz^{i}PrLu(CH$_2$SiMe$_3$)$_2$					
N_1–Lu_1	2.281	C_2–N_2–N_3	124.29	C_1–C_2–N_2–N_3	–29.6
N_3–Lu_1	2.446	C_9–N_4–N_5	124.29	C_8–C_9–N_4–N_5	–29.6
N_5–Lu_1	2.449	N_1–Lu_1–C_{49}	121.35	C_2–N_2–N_3–C_{15}	–173.0
C_2–N_2	1.424	C_{49}–Lu_1–C_{53}	117.27	C_9–N_4–N_5–C_{19}	–173.0
C_9–N_4	1.424	N_1–Lu_1–C_{53}	121.38		
Lu_1–C_{49}	2.380				
Lu_1–C_{53}	2.380				
CzPz^{i}PrSc(CH$_2$SiMe$_3$)$_2$					
N_1–Sc_1	2.127	C_2–N_2–N_3	124.04	C_1–C_2–N_2–N_3	–23.9
N_3–Sc_1	2.328	C_9–N_4–N_5	124.04	C_8–C_9–N_4–N_5	–23.9
N_5–Sc_1	2.328	N_1–Sc_1–C_{49}	118.85	C_2–N_2–N_3–C_{15}	–174.6
C_2–N_2	1.421	C_{49}–Sc_1–C_{53}	122.28	C_9–N_4–N_5–C_{19}	–174.6
C_9–N_4	1.421	N_1–Sc_1–C_{53}	118.87		
Sc_1–C_{49}	2.239				
Sc_1–C_{53}	2.239				
CzPz^{i}PrY(CH$_2$SiMe$_3$)$_2$					
N_1–Y_1	2.300	C_2–N_2–N_3	122.42	C_1–C_2–N_2–N_3	–35.3
N_3–Y_1	2.488	C_9–N_4–N_5	122.42	C_8–C_9–N_4–N_5	–35.2
N_5–Y_1	2.488	N_1–Y_1–C_{49}	111.64	C_2–N_2–N_3–C_{15}	–165.7
C_2–N_2	1.425	C_{49}–Y_1–C_{53}	136.73	C_9–N_4–N_5–C_{19}	–165.7
C_9–N_4	1.425	N_1–Y_1–C_{53}	111.63		
Y_1–C_{49}	2.404				
Y_1–C_{53}	2.404				

Incorporation of the *tert*-butyl functionalities appears to have more of a significant impact on the bond length and angle parameters of a metal complex. In particular, a significant increase in the torsion angles C_1–C_2–N_2–N_3 and C_8–C_9–N_4–N_5 is apparent (CzPz^{t}BuLu(CH$_2$SiMe$_3$)$_2$: –36.2°, –36.1°; CzPz^{t}BuSc(CH$_2$SiMe$_3$)$_2$: –32.5°, –39.0°; CzPz^{t}BuY(CH$_2$SiMe$_3$)$_2$: –38.3°, –39.1°, Table 3.8). In addition, the C–Ln–C bond angle drastically increases, which is likely an effect of the increased steric bulk above the metal centre, forcing the alkyl groups to become more planar (C–Ln–C–Si

torsion angle = ~180°). This increase can be easily visualized in Figure 3.19, Figure 3.20, and Figure 3.21.

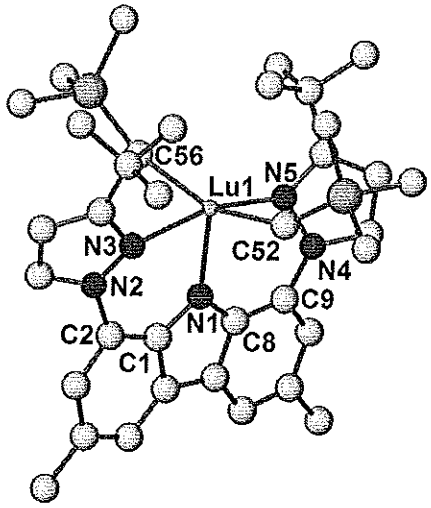

Figure 3.19 Computationally determined structure of CzPz^{t}BuLu(CH_2SiMe_3)$_2$ from geometry optimization using B3WP91/6-31G(d,p).

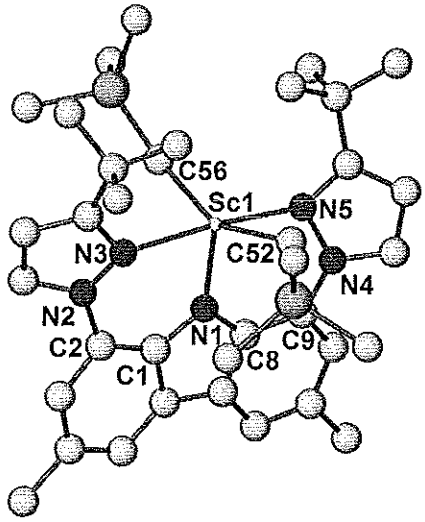

Figure 3.20 Computationally determined structure of CzPz^{t}BuSc(CH_2SiMe_3)$_2$ from geometry optimization using B3WP91/6-31G(d,p).

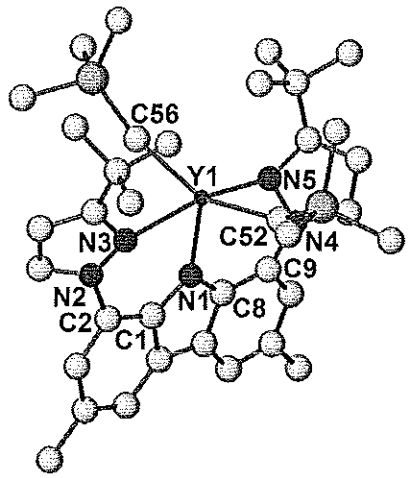

Figure 3.21 Computationally determined structure of CzPz^{t}BuY(CH_2SiMe_3)$_2$ from geometry optimization using B3WP91/6-31G(d,p).

Table 3.8 Select bond lengths (Å) and angles (°) of the computationally determined CzPz^{t}Bu metal complexes.

Bond Lengths (Å)		Bond Angles (°)		Torsion Angles (°)	
CzPz^{t}BuLu(CH_2SiMe_3)$_2$					
N_1–Lu_1	2.243	C_2–N_2–N_3	124.15	C_1–C_2–N_2–N_3	–36.2
N_3–Lu_1	2.485	C_9–N_4–N_5	124.16	C_8–C_9–N_4–N_5	–36.1
N_5–Lu_1	2.489	N_1–Lu_1–C_{52}	100.96	C_2–N_2–N_3–C_{15}	–167.7
C_2–N_2	1.425	C_{52}–Lu_1–C_{56}	158.09	C_9–N_4–N_5–C_{19}	–167.8
C_9–N_4	1.425	N_1–Lu_1–C_{56}	100.95		
Lu_1–C_{52}	2.402				
Lu_1–C_{56}	2.402				
CzPz^{t}BuSc(CH_2SiMe_3)$_2$					
N_1–Sc_1	2.096	C_2–N_2–N_3	124.58	C_1–C_2–N_2–N_3	–32.5
N_3–Sc_1	2.389	C_9–N_4–N_5	123.99	C_8–C_9–N_4–N_5	–39.0
N_5–Sc_1	2.463	N_1–Sc_1–C_{52}	104.33	C_2–N_2–N_3–C_{15}	–169.0
C_2–N_2	1.422	C_{52}–Sc_1–C_{56}	150.90	C_9–N_4–N_5–C_{19}	–168.6
C_9–N_4	1.421	N_1–Sc_1–C_{56}	102.57		
Sc_1–C_{52}	2.267				
Sc_1–C_{56}	2.253				
CzPz^{t}BuY(CH_2SiMe_3)$_2$					
N_1–Y_1	2.283	C_2–N_2–N_3	124.60	C_1–C_2–N_2–N_3	–38.3
N_3–Y_1	2.517	C_9–N_4–N_5	124.43	C_8–C_9–N_4–N_5	–39.1
N_5–Y_1	2.535	N_1–Y_1–C_{52}	101.66	C_2–N_2–N_3–C_{15}	–169.5
C_2–N_2	1.424	C_{52}–Y_1–C_{56}	156.00	C_9–N_4–N_5–C_{19}	–169.4
C_9–N_4	1.424	N_1–Y_1–C_{56}	100.98		
Y_1–C_{52}	2.435				
Y_1–C_{56}	2.428				

Finally, addition of the phenyl moieties resulted in the most significant structural changes out of all of the CzPz derivatives analyzed. Compared to the original calculated structure of CzPzPh, the pyrazole moieties still occupy the same plane with respect to the carbazole backbone even upon metal complexation. The torsion angles that define this plane (C_1–C_2–N_2–N_3 and C_8–C_9–N_4–N_5) also exhibit a significant increase (Lu: –43.7°, 44.3°; Sc: –37.7°, 41.5°; Y: –42.8°, 46.6°). This in turn forces the lanthanide centre to lay outside of the carbazole plane, yielding a geometry at the metal somewhere between trigonal bipyramidal and square pyramidal. The C_{56}–Ln–C_{60} angle is substantially larger (Lu: 151.16°; Sc: 154.90°; Y: 153.56°) than those observed in the CzPzMe complexes, and is likely a direct consequence of the bulkier phenyl rings. The added steric bulk of the phenyl rings also results in the lanthanide-alkyl groups pointing upwards and away from the ligand scaffold, a trend that had only been observed in the yttrium complexes.

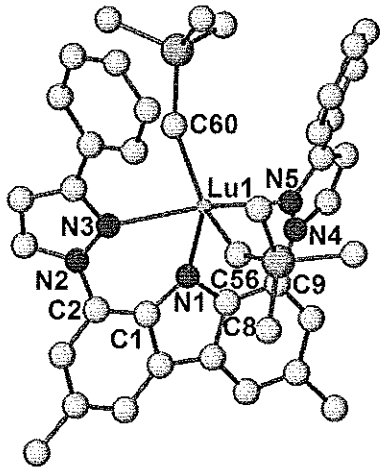

Figure 3.22 Molecular structure of CzPzPhLu(CH_2SiMe_3)$_2$ from geometry optimization using B3WP91/6-31G(d,p).

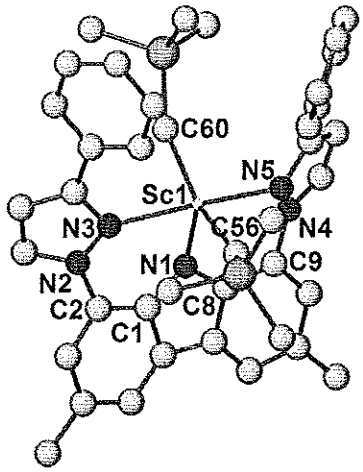

Figure 3.23 Molecular structure of CzPzPhSc(CH_2SiMe_3)$_2$ from geometry optimization using B3WP91/6-31G(d,p).

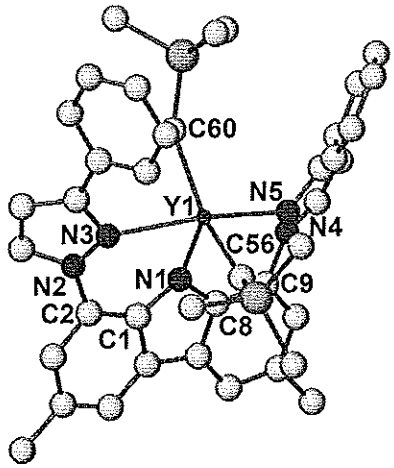

Figure 3.24 Molecular structure of CzPzPhY(CH_2SiMe_3)$_2$ from geometry optimization using B3WP91/6-31G(d,p).

Table 3.9 Select bond lengths (Å) and angles (°) of the computationally determined CzPzPh metal complexes.

Bond Lengths (Å)		Bond Angles (°)		Torsion Angles (°)	
CzPzPhLu(CH_2SiMe_3)$_2$					
N_1–Lu_1	2.277	C_2–N_2–N_3	123.45	C_1–C_2–N_2–N_3	–43.7
N_3–Lu_1	2.491	C_9–N_4–N_5	123.02	C_8–C_9–N_4–N_5	44.3
N_5–Lu_1	2.478	N_1–Lu_1–C_{56}	100.65	C_2–N_2–N_3–C_{15}	–170.3
C_2–N_2	1.421	C_{56}–Lu_1–C_{60}	151.16	C_9–N_4–N_5–C_{19}	167.0
C_9–N_4	1.421	N_1–Lu_1–C_{60}	107.93		
Lu_1–C_{56}	2.385				
Lu_1–C_{60}	2.373				
CzPzPhSc(CH_2SiMe_3)$_2$					
N_1–Sc_1	2.122	C_2–N_2–N_3	123.70	C_1–C_2–N_2–N_3	–37.7
N_3–Sc_1	2.360	C_9–N_4–N_5	122.95	C_8–C_9–N_4–N_5	41.5
N_5–Sc_1	2.376	N_1–Sc_1–C_{56}	99.56	C_2–N_2–N_3–C_{15}	–172.4
C_2–N_2	1.419	C_{56}–Sc_1–C_{60}	154.90	C_9–N_4–N_5–C_{19}	166.8
C_9–N_4	1.421	N_1–Sc_1–C_{60}	105.53		
Sc_1–C_{56}	2.250				
Sc_1–C_{60}	2.228				
CzPzPhY(CH_2SiMe_3)$_2$					
N_1–Y_1	2.309	C_2–N_2–N_3	123.35	C_1–C_2–N_2–N_3	–42.8
N_3–Y_1	2.511	C_9–N_4–N_5	122.86	C_8–C_9–N_4–N_5	46.6
N_5–Y_1	2.520	N_1–Y_1–C_{56}	99.68	C_2–N_2–N_3–C_{15}	–171.2
C_2–N_2	1.420	C_{56}–Y_1–C_{60}	153.56	C_9–N_4–N_5–C_{19}	166.2
C_9–N_4	1.422	N_1–Y_1–C_{60}	106.46		
Y_1–C_{56}	2.415				
Y_1–C_{60}	2.406				

3.5 Reactivity of CzPzMe Lanthanide Complexes

Preliminary experiments involving the reactivity of $L_2^{Me}Lu(CH_2SiMe_3)_2$ and $L_2^{Me}Sc(CH_2SiMe_3)_2$ have been conducted to gain insight regarding their chemical potential.

3.5.1 *Reactivity of* $L_2^{Me}Lu(CH_2SiMe_3)_2$ (**18**)

In the pursuit of forming a terminal lanthanide-imido complex, the reaction of **18** with various anilines was explored *via* NMR scale scoping reactions. Reaction of one equivalent of **18** with Mes*NH_2 at 50 °C for 14 hours resulted in the formation of mixed alkyl/amido lanthanide compound **21** (Scheme 3.11), as indicated by ^1H and ^{13}C NMR spectroscopy. As expected, a broad NH signal indicative of an anilido functionality was observed at δ 3.45 (benzene-d_6). The lutetium alkyl groups shifted slightly downfield ($Si(CH_3)_3$: δ −0.19; Lu–CH_2: δ −0.21), but no other significant changes compared to those observed for **18** were noted.

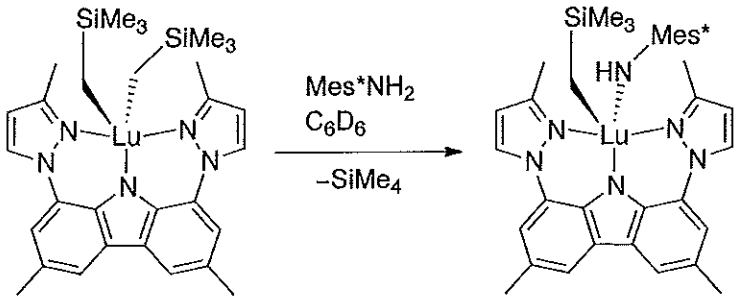

18 **21**

Scheme 3.11 *In situ* synthesis of **21**.

To promote conversion to the desired imido compound, and thus loss of additional alkane, the temperature of the reaction mixture was gently increased to 65 °C. After 2.5 hours and no observable change, the temperature was increased again, this time to 100 °C, and the reaction mixture was heated for an additional 12 hours. When no transformation was observed, a stoichiometric equivalent of DMAP was added to the reaction mixture, as this has been previously reported to be successful.[43] Under these conditions, no immediate reaction was observed. The NMR

tube and its contents were again gently heated to 75 °C, but after 48 hours still no conversion was observed. While no reaction was evident, these experiments attest to the thermal stability of CzPzMe supported rare earth metal compounds, which is a significant accomplishment within the field.

Utilizing a substrate of the same steric bulk, the reactivity of **18** with 2,4,6-tri-*tert*-butylphenylphosphine was explored. Again, under ambient conditions, no transformation occurred. To promote conversion, the mixture was heated to 50 °C for 21 hours, with no change observed. Following a temperature increase to 75 °C over 24 hours, still no reaction was detected. Finally, after a total time of 72 hours at 75 °C, complete decomposition of **18** occurred, with only resonances attributed to tri-*tert*-butylphenylphosphine present in the ^{1}H NMR spectrum. This lack of reactivity in the presence of a phosphine is attributed to the relative basicity of the phosphine and amine functionalities. Amines have a relatively higher basicity in comparison to phosphines, making them a more suitable candidate for reactivity with an acidic metal centre. Therefore, to facilitate this type of transformation, a phosphine of less steric bulk may be of interest.

*3.5.2 Reactivity of $L_2^{Me}Sc(CH_2SiMe_3)_2$ (**19**)*

As a direct comparison to the reactivity observed with **18**, $L_2^{Me}Sc(CH_2SiMe_3)_2$ (**19**) was reacted with one stoichiometric equivalent of Mes^*NH_2 (Scheme 3.12). Upon heating the reaction mixture to 50 °C over 24 hours, no transformation was observed. This is likely a consequence of the smaller ionic radius of scandium in

comparison to lutetium (Sc = 0.745 Å vs. Lu = 0.861 Å),[102] therefore making scandium less accessible to bulky substrates. As such, similar reactivity was pursued using a less bulky aniline, $MesNH_2$ (Scheme 3.12). In this instance, double substitution of the alkyl groups was noted, resulting in starting material **19**, and the double anilido $L_2^{Me}Sc(NHMes)_2$ (**22**). Compound **22** was then purposefully synthesized *in situ*, with conversion from **19** achievable under ambient conditions.

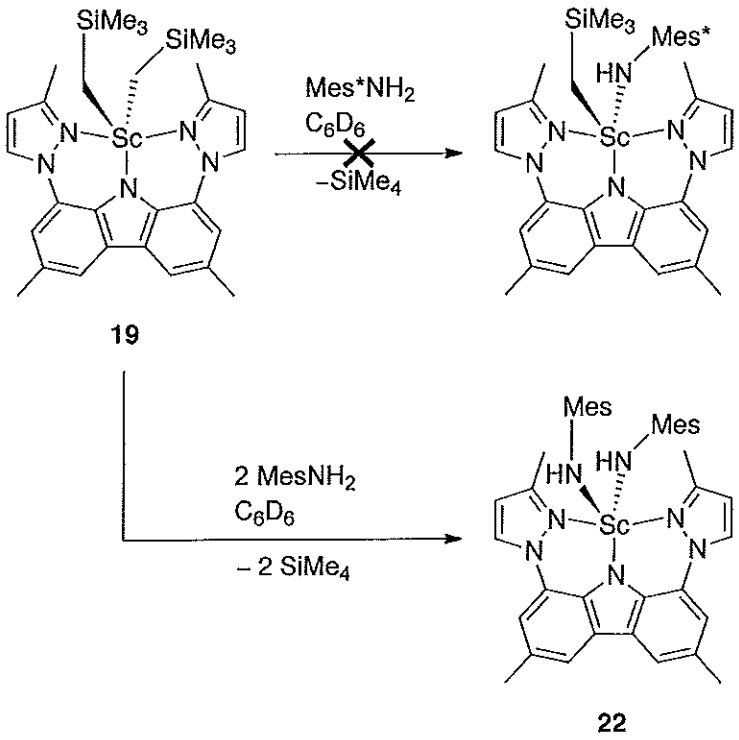

Scheme 3.12 Scoping reactions of **19** with various anilines to determine steric bulk requirements.

The diagnostic NH peak for compound **22** resonates at δ 3.57 in the ^1H NMR spectrum in benzene-d_6. No significant shifts in the ligand scaffold are noted, but the resonances corresponding to the Mes functionalities appear at 6.66 (s, 2H, Ar*H*), 2.13 (s, 3H, *p*-C*H*$_3$), and 2.09 (s, 6H, *o*-C*H*$_3$).

In probing the steric requirements for the reactivity of compound **19**, $DippNH_2$ as a substrate was also investigated, as it possesses steric bulk between that of Mes^*NH_2 and $MesNH_2$. With no reaction observed at ambient temperature, the reaction mixture was gently heated to 50 °C, resulting in the formation of the desired mixed alkyl/anilido $L_2^{Me}Sc(CH_2SiMe_3)(NHDipp)$. However, in allowing the reaction to proceed to completion, evolution of $L_2^{Me}Sc(NHDipp)_2$ is observed in the reaction mixture, in addition to starting material and $L_2^{Me}Sc(CH_2SiMe_3)(NHDipp)$. This suggests that even the Dipp functionality does not posses the proper steric bulk to generate a mixed alkyl/anilido scandium compound supported by HL_2^{Me}.

3.6 Conclusions

In summary, the synthesis of a novel *NNN* tridentate pincer ligand composed of carbazole (Cz) and pyrazole (Pz) groups was successfully accomplished and the corresponding compounds characterized by multinuclear NMR spectroscopy and single-crystal X-ray diffraction, where applicable. The resulting ligand system was able to support base-free and monomeric scandium and lutetium dialkyl compounds that were prepared *via* protonolysis routes. These compounds exude enhanced thermal stability relative to the phosphinimine analogues presented in Chapter 2. This increase in stability may be due to reduced peripheral steric bulk of the ancillary combined with less accessible C–H functionalities, as both pyrazole moieties are computationally observed to be near coplanar with respect to carbazole in the presence of a metal. In addition, the rigid geometry imposed by the

pyrazole groups prevents unwanted intramolecular reactions between the ligand and metal centre from occurring by hindering formation of the necessary 4-centred transition state. An yttrium congener of HL_2^{Me} was also explored, but decomposition occurring between 24-48 hours at ambient temperature led to an indiscernible mixture of products that could not be easily reconstituted in solution. Decomposition of this nature could potentially be due to dimerization or oligomerization of the metal complex, as yttrium does possess a larger ionic radius than either lutetium or scandium. To gain further insight into the resultant metal complexes, computational modeling was employed. These models confirmed the rigidity of HL_2^{Me}, as deviation from the proteo ligand was minor upon metal complexation. Slight rotations of the pyrazole moieties were noted in the presence of the metal centre, with the resultant change in torsion angle directly correlated to the size of the metal centre. Additional computational studies with bulkier versions of CzPz demonstrated that increasing steric bulk primarily affects the geometry at the metal centre, changing from trigonal bipyramidal to square pyramidal as the size of the substituent increases. In addition, the pyrazole groups are significantly more rotated compared to the carbazole plane when larger substituents are analyzed.

Finally, reactivity of compounds $L_2^{Me}Lu(CH_2SiMe_3)_2$ and $L_2^{Me}Sc(CH_2SiMe_3)_2$ (**18** and **19**, respectively) is highly dependent on the size of the substrate due to differences in ionic radii between the two metal centres. Single substitution of one alkyl group can be achieved in the case of **18**, affording the mixed alkyl/anilido compound $L_2^{Me}Lu(CH_2SiMe_3)(NHMes^*)$. Studies on **19**, however, have demonstrated

that bulky systems, such as Mes^*NH_2, result in no reaction. The employment of less sterically bulky anilines with **19**, such as $MesNH_2$ and $DippNH_2$, results in the bis(amido) complex $L_2^{Me}Sc(NHMes)_2$ (**22**), and concomitant formation of $L_2^{Me}Sc(NHDipp)_2$ and $L_2^{Me}Sc(CH_2SiMe_3)(NHDipp)$, respectively.

Chapter 4

Future Work and Conclusions

4.1.1 HL_1^{Pipp} Organometallic Chemistry

As presented in Chapter 2, the bis(phosphinimine) ligand containing constrained phospholane moieties did not suffice in preventing unwanted cyclometalative reactivity. While decomposition of both the lutetium (**12**) and scandium (**14**) dialkyl complexes was observed, the rates at which the resulting metalated products formed was notably slower than previous ligand systems reported by the Hayes group. As such, potential reactivity of complexes **12** and **14** could be explored upon their formation *in situ*. Indeed, preliminary investigations of this nature were conducted. Scoping reactions to generate the mixed amide/alkyl derivative of **12** were performed in hopes of generating a terminal lutetium imide through loss of $SiMe_4$ (Scheme 4.1).[43]

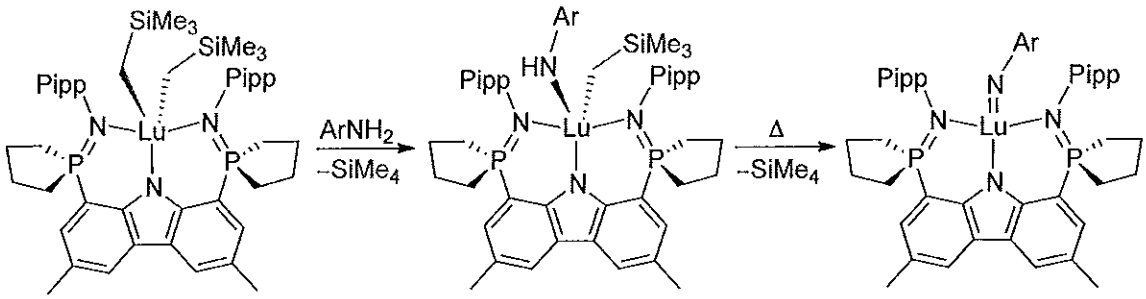

Scheme 4.1 Proposed synthetic pathway for the formation of a terminal Lu imido complex.

In order to gauge the steric bulk requirements of the binding pocket, two anilines were employed. The bulkier of the two anilines, Mes*NH_2, had shown promise with the ligand systems **1a** and **1b** in metalacycle ring opening, resulting in only single substitution to afford the mixed anilido/alkyl compound **6** (Scheme 1.15). The less bulkier congener, PippNH_2, was also explored, though previous work with **1a** and **1b** had demonstrated that the bis(anilido) was obtained.[68]

With regard to reactivity of complex **12**, reaction with one equivalent of Mes*NH_2 resulted in no immediate reaction. This lack of reaction can likely be attributed to the extreme steric bulk of the Mes* aryl group. Gentle heating of the reaction mixture (40 °C) was performed, but the thermal instability of precursor **12** led to decomposition. Investigations employing one equivalent of PippNH_2 yielded the bis(anilide) compound L_1^{Pipp}Lu(NHPipp)$_2$ (Scheme 4.2) at ambient temperature, suggesting that PippNH_2 does not possess sufficient steric bulk to generate a Lu complex of the ilk L_1^{Pipp}Lu(CH_2SiMe_3)(NHPipp). These findings advocate that additional scoping reactions with anilines of steric bulk between that of Mes* and Pipp are required to form the desired mixed alkyl/anilido species.

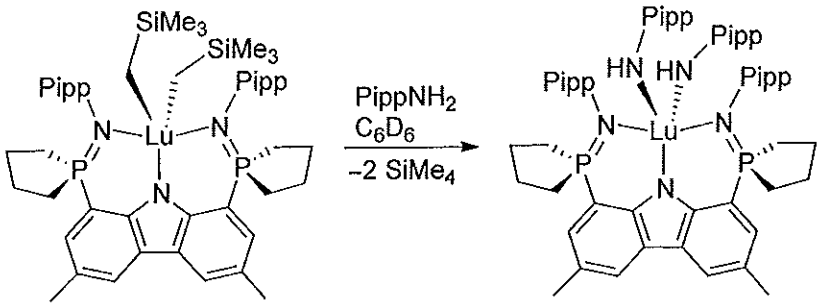

Scheme 4.2 Reactivity of **12** to form the bis(anilido) compound $L_1^{Pipp}Lu(NHPipp)_2$.

The above reactions imply that the chemistry of **12** can be explored prior to cyclometalation. However, this reactivity is somewhat limited by the thermal sensitivity of the parent compound.

4.1.2 HL_2^{Me} Organometallic Chemistry

Similar to the reactivity attempted with compound **12**, formation of a L_2^{Me} Ln=NR species was pursued. While reactions of $L_2^{Me}Lu(CH_2SiMe_3)_2$ (**17**) with Mes^*NH_2 have yielded the mixed anilido/alkyl compound, subsequent loss of alkane to generate the desired lutetium imido complex was not observed (Scheme 3.11). Therefore, the use of alternate anilines with reduced steric bulk might be required to drive imide formation.

Additional multiply bonded lanthanide compounds, including phosphinidenes and silylenes, are also of interest. Using an approach similar to that attempted for imido formation, addition of one equivalent of either an aryl phosphine or aryl silane to the lutetium dialkyl compound **17** may result in formation of either a mixed phosphido/alkyl (Scheme 4.3) [159] or silyl/alkyl (Scheme

4.4) compound, respectively. It is expected that under thermal conditions, the resulting compounds will lose an additional equivalent of tetramethylsilane, yielding a phosphinidene (Scheme 4.3) or silylene complex (Scheme 4.4).

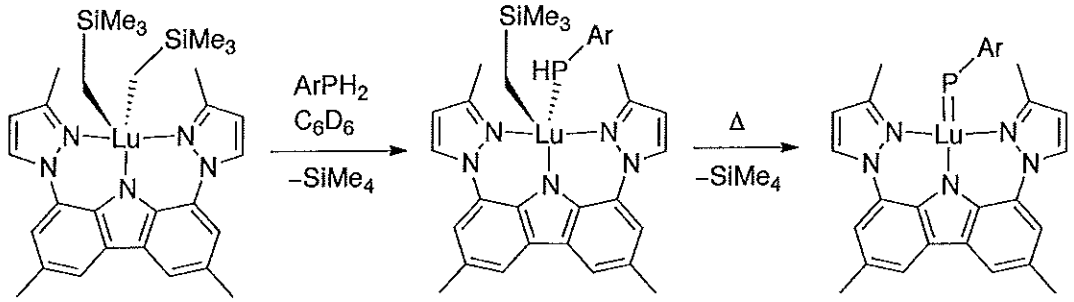

18

Scheme 4.3 Proposed synthetic approach for the formation of a lutetium phosphinidene.

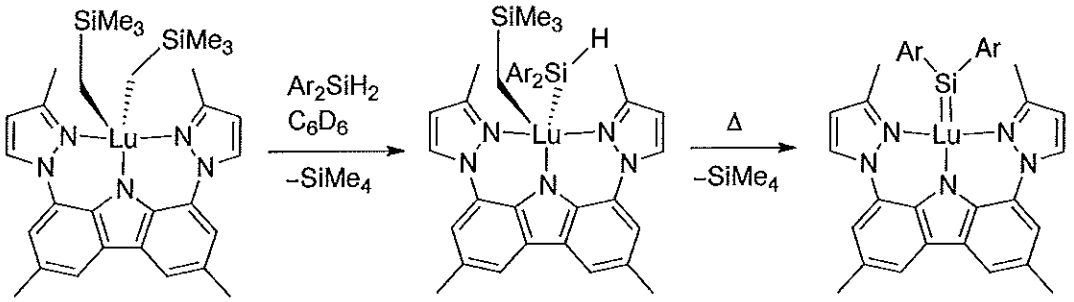

18

Scheme 4.4 Synthesis of a lutetium silylene complex from compound **17**.

Interest in multiply bonded lanthanide compounds stems from the unique reaction chemistry reported for their transition metal analogues. Processes such as hydroamination, as well as C–H bond activation can be mediated by complexes of the form $L_nM{=}E'$ (L = ancillary ligand; M = transition metal; E' = SiR_2, NR, PR). Notably, these are vital transformations in both the pharmaceutical and petrochemical industries, respectively.[44] Formation of lanthanide multiply-bonded compounds (Ln=E') may offer enhanced catalytic reactivity (i.e. higher activity,

greater selectivity) for these important synthetic processes, or alternatively, offer entirely new transformations.[45]

4.2 Tuning of Existing Ligands

4.2.1 HL_1^{Pipp} Modifications

The bis(phosphinimine) framework **11** offers a sterically encumbered environment for organometallic lanthanide compounds. While the phospholane rings were intended to reduce the peripheral steric bulk and enhance electron donation to the metal centre, orthometalation of the N-aryl group was still observed. A viable option to circumvent this problem is to eliminate sources of C–H bonds capable of participating in metalation. This can be achieved by modification of the *N*-aryl rings. Of particular interest is the inclusion of pyrimidine moieties, which would create a ligand capable of pentadentate *NNNNN* coordination (Figure 4.1). The nitrogen atoms, which are located in the *ortho* position, are also anticipated to increase the electron donation of the overall ligand, by potentially serving as additional Lewis bases.

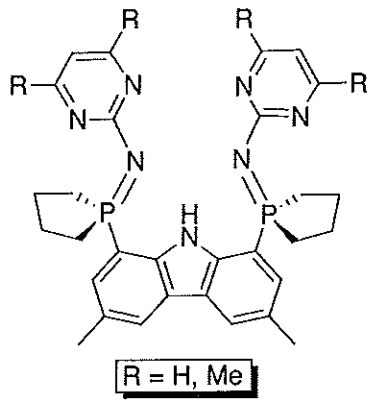

Figure 4.1 Modified HL_1 ligand with pyrimidine *N*-aryl groups.

Accordingly, two pyrimidine derivatives were pursued, pyrimidine and 2,4-dimethylpyrimidine, in which both of the precursors can be prepared using modified literature procedures.[160-162] As with **11**, the pyrimidine functionalities can be installed using the Staudinger reaction. Preliminary work has primarily consisted of the synthesis and characterization of the bis(phosphinimine) ligand substituted with 2,4-dimethyl-pyrimidine. Previous work in the Hayes lab has utilized the unsubstituted pyrimidine version of the bis(diphenylphosphine) ligand (Scheme 4.5).[68] The resultant κ^5-bound dialkyl lutetium complex (Scheme 4.5) exhibits enhanced stability, but after 5 hours decomposition begins, and is completed after 18 hours at ambient temperature. In contrast to the cyclometalation commonly observed, dearomatization of the pyrimidine rings occurred *via* a 1,5-alkyl migration, in which the alkyl groups on lutetium migrated to the 4 position of the pyrimidine ring (Scheme 4.6). The final bimetallic product was identified by single-crystal X-ray diffraction.[68]

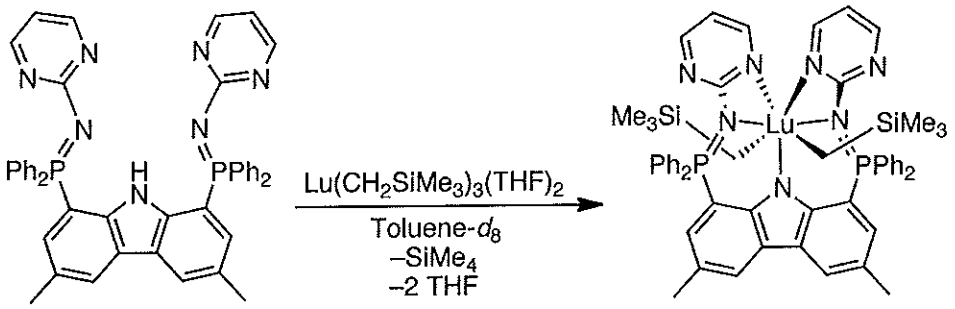

Scheme 4.5 Reactivity of bis(diphenylphosphine) pyrimidine ligand.

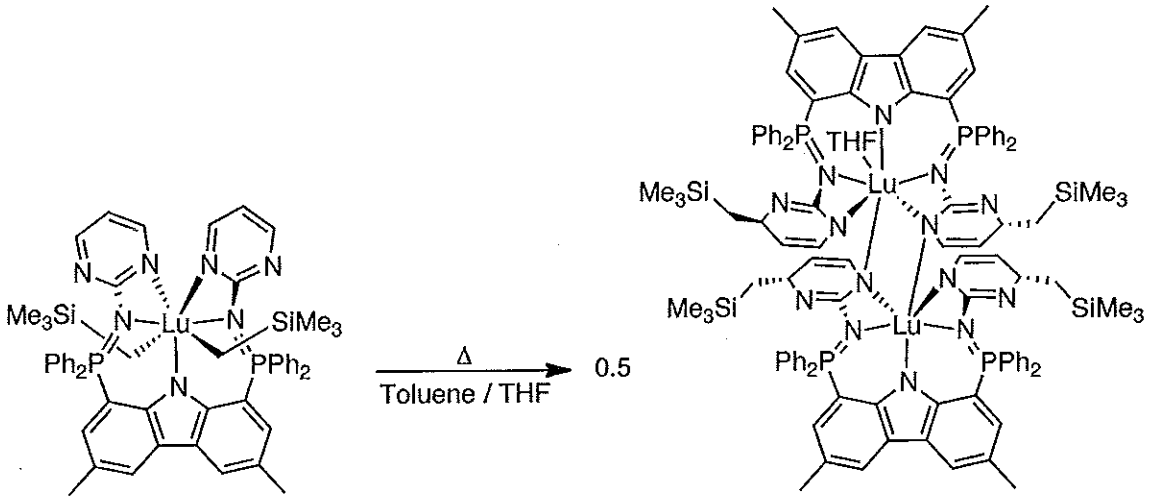

Scheme 4.6 1,5-alkyl migration in a dialkyl lutetium complex.

Attempts to prevent the alkyl migration from occurring resulted in the incorporation of 2,4-dimethyl pyrimidine, yielding compound **23**. Exhibiting additional steric bulk, the intent of the methyl groups was to potentially block similar rearrangements from taking place. This new scaffold was subsequently reacted with $Lu(CH_2SiMe_3)_3(THF)_2$, as shown in Scheme 4.7, to afford the dialkyl lutetium compound **24**.

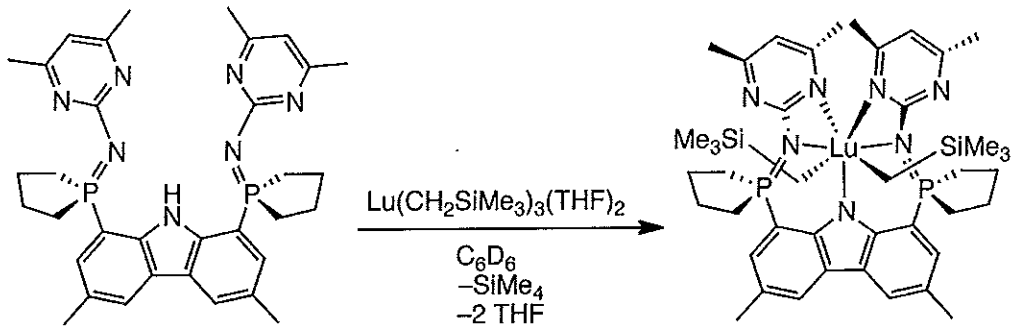

23 **24**

Scheme 4.7 Reaction of compound **23** with $Lu(CH_2SiMe_3)_2(THF)_2$ to yield the *NNNNN* bound dialkyl lutetium **24**.

Unfortunately, over time (12 hours), an indiscernible mixture of decomposition products was obtained. While it was not possible to unambiguously establish, a similar 1,5-alkyl migration may have occurred. Literature precedent for this phenomenon has demonstrated that bulkier ancillaries, such as the 2,2':6',2''-terpyridine (terpy) ligand system are also susceptible to a similar form of rearrangement (Scheme 4.8).[163] Future studies of this system and attempts at recrystallization are still required to determine the identity of the decomposition products. Incorporation of even bulkier pyrimidine functionalities, such as 2,4-di-*tert*-butylpyrimidine, might also be useful for preventing decomposition.

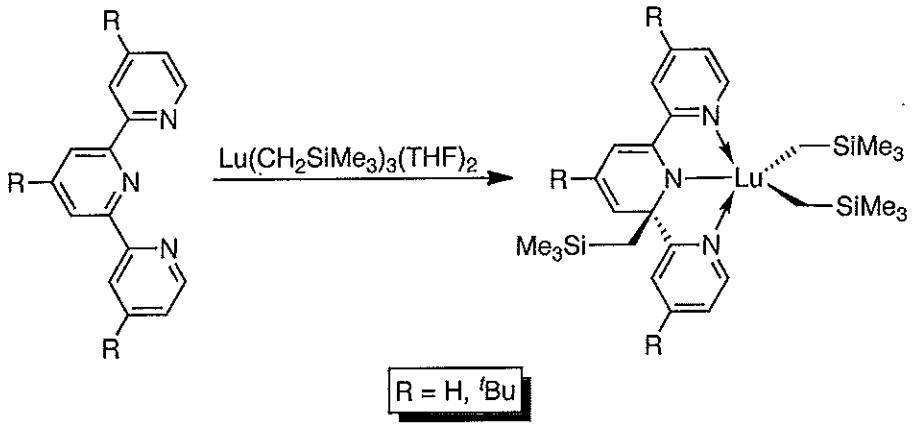

Scheme 4.8 1,3-CH_2SiMe_3 alkyl migration of a terpy supported lutetium dialkyl complex.

4.2.2 HL_2 Modifications

The CzPzMe ligand presented in Chapter 3 proved to be a viable option for supporting thermally stable lutetium and scandium dialkyl complexes. As determined computationally, rotation of the 3-methylpyrazole moieties is dependent on the size of the metal centre, whereby increasing size results in greater rotation. In the case of the yttrium analogue, which possesses the largest ionic radius, this rotation may have decreased the steric pressure at the metal centre, thus facilitating processes such as dimerization or oligomerization. Employing bulkier substituents at the 3-position of pyrazole could potentially inhibit such activity. Preliminary work to synthesize bulkier pyrazole molecules to be used in future CzPz syntheses is currently underway in the Hayes lab. Of particular interest are the ^{i}Pr, ^{t}Bu, and Ph pyrazole derivatives (Figure 4.2). While these bulkier substituents should aid in sterically protecting the metal centre, literature precedent also indicates that in the absence of electron withdrawing groups,

increased steric bulk should assist in enhancing electronic donation to the metal centre.

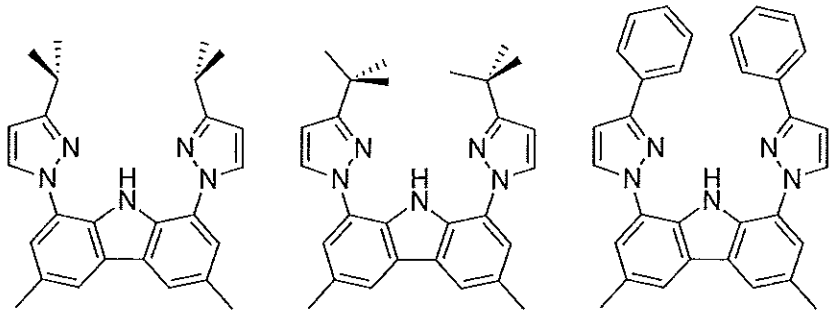

Figure 4.2 Proposed family of CzPz ligands of different steric bulk: **A)** ^{i}Pr **B)** ^{t}Bu **C)** Ph.

4.3 Alternative Ancillary Ligands

Following suit with the inclusion of *N*-heterocyclic donors, the 3,6-dimethyl-1,8-bis(indazolyl)-carbazole (CzIndz) ancillary is of interest. Indazole itself is a relatively expensive starting material ($194 for 5 g, Sigma-Aldrich), therefore, it is more economically appealing to synthesize the chemical precursor. This can be achieved by reducing 2-nitrobenzonitrile ($84 for 10 g, Sigma-Aldrich) with one equivalent of lithium aluminum hydride (LAH) (Scheme 4.9). However, indazole exists in two tautomeric forms, the kinetically favored 1H-indazole (Scheme 4.9, **D**) and thermodynamically favored 2H-indazole (Scheme 4.9, **E**), whereby **E** is the principal tautomer. As such, it is anticipated that in performing the Ullman coupling reaction formation of CzIndz**E** (Figure 4.3) would predominantly occur, based on the reaction conditions (155 °C) required for synthesis. In the case of aryl iodides, this is indeed the case.[164] However, for reactions involving aryl bromides, a mixture of both products is observed, as the equilibrium rate of **D** and **E** is in competition

with the rate of oxidative addition.[164] With the separation potential of these two compounds unknown, and a greater desire to synthesize CzIndz**D** as it provides greater steric bulk at the binding pocket, a synthetic approach that does not utilize Ullman coupling principles is of interest.

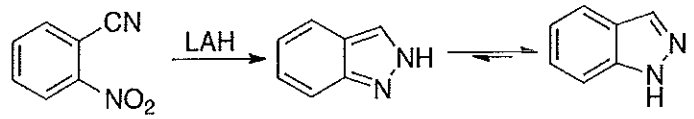

D **E**

Scheme 4.9 Synthesis of 1H-indazole (**D**) and 2H-indazole (**E**).

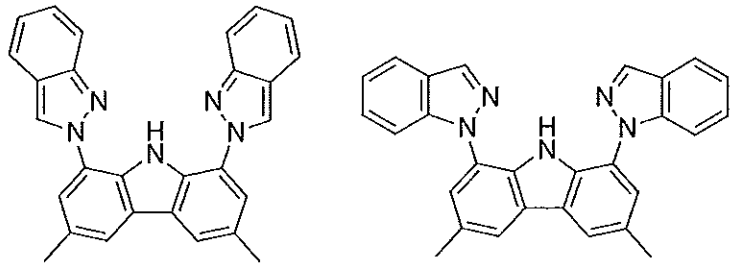

CzIndz**D** CzIndz**E**

Figure 4.3 Potential CzIndz ligands.

As such, an alternative synthetic strategy has been hypothesized to allow for greater control over the final product (Scheme 4.10). Starting from carbazole, chlorination of the 3,6-positions can be achieved using thionyl chloride.[165] Following chlorination, nitration at the 1,8-positions can be accomplished using nitric acid.[165] A palladium-mediated reduction allows for conversion of the nitro to the amine, which can be performed on multigram scales.[166] Direct formation of the indazole moiety can likely be induced in the presence of a copper catalyst, generating the desired CzIndz**D** ligand.[167]

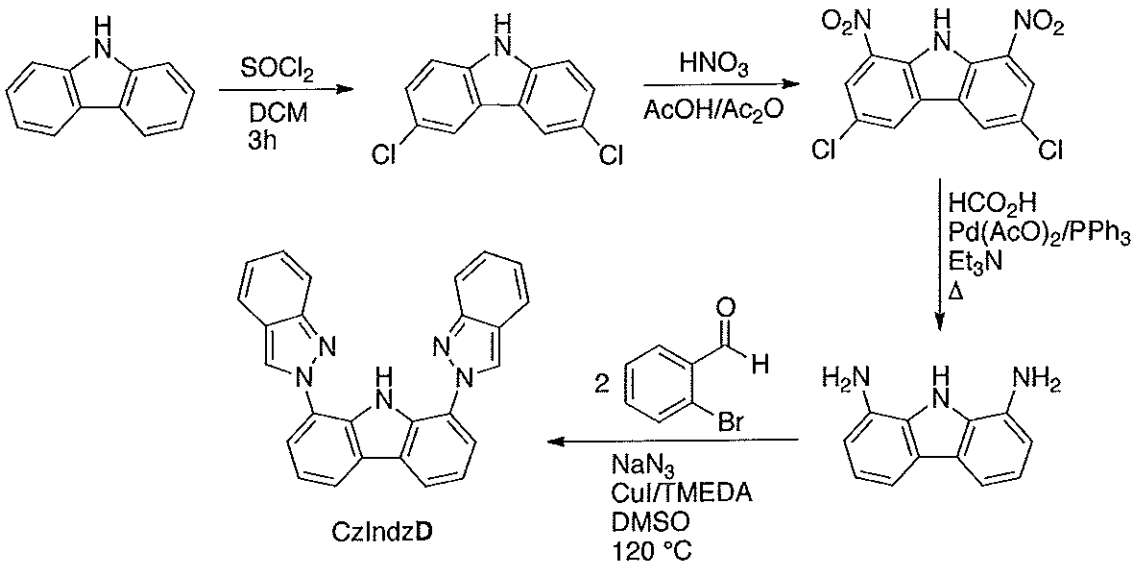

Scheme 4.10 Proposed CzIndzD synthesis.

4.4 Alternative Ligand Synthesis

4.4.1 Synthesis of HL_1^{Pipp}

As presented in Chapter 2, phospholane rings can be installed at the 1,8-positions of carbazole *via* a lithium-halogen exchange route. The overall complexity of the multi-step synthesis and low yield (41.6%) of the chlorophospholane precursor, however, has resulted in the development of additional methods. One such approach is to generate the cyclic phosphine on the ancillary itself (Scheme 4.11). Starting from 1,8-dibromo-3,6-dimethyl-9^{t}BOC-carbazole, a lithium-halogen exchange can be performed, allowing for the installation of PCl_2. The resulting bis(dichlorophosphine) molecule could subsequently be reacted with the desired Grignard reagent, in this case $MgBr(C_4H_8)MgBr$, to yield the bis(phospholane)

compound **9**. From a time perspective, this method is advantageous as it completely removes the synthesis, and subsequent isolation and purification, of the chlorophospholane.

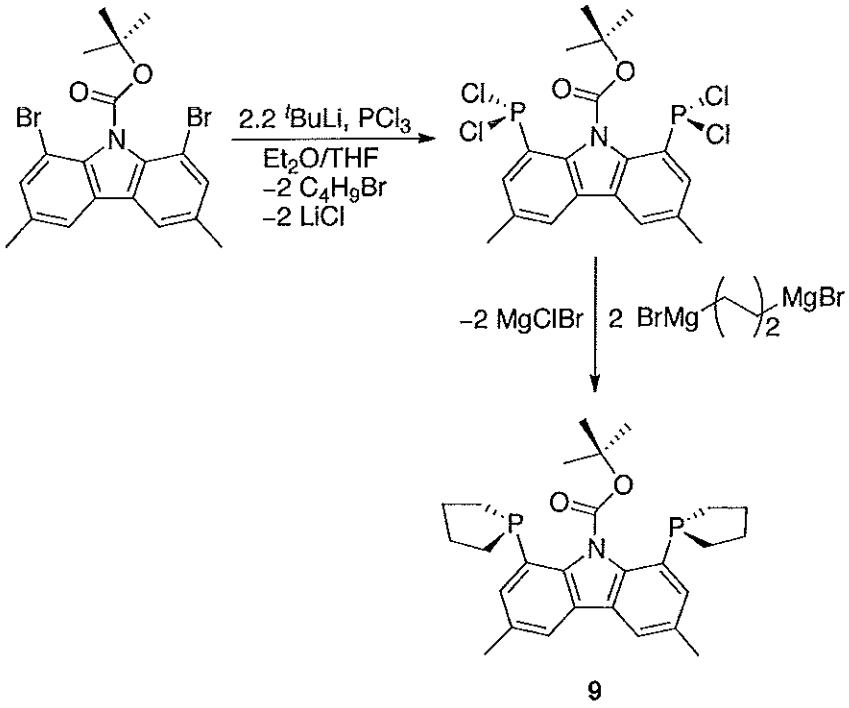

9

Scheme 4.11 Alternative synthetic approach for the formation of **9**.

Initial investigations into this alternative synthesis have been attempted, in which installation of the PCl_2 groups resulted in the formation of a mixed chloro/bromo phosphine due to halogen exchange (**25**). This was determined crystallographically (Figure 4.4), where each chlorine atom experiences substitional disorder with a bromine atom. Determination of exact disorder percentages during refinement was difficult, but crude values for the occupations are as follows: 0.48, Cl1 / 0.52, Br1; 0.46, Cl2 / 0.54, Br2; 0.42, Cl3 / 0.58, Br3; 0.48, Cl4 / 0.52, Br4; 0.47, Cl5 / 0.53, Br5; 0.60, Cl6 / 0.40, Br6; 0.39, Cl7 / 0.61, Br7; 0.52, Cl8 / 0.48, Br8. A total of 8 values for each halide atom is attributed to two molecules co-crystallizing

in the asymmetric unit. To circumvent the formation of this mixture, and gain greater stoichiometric control of future reactivity, PBr_3 should be considered as an alternative phosphine source.

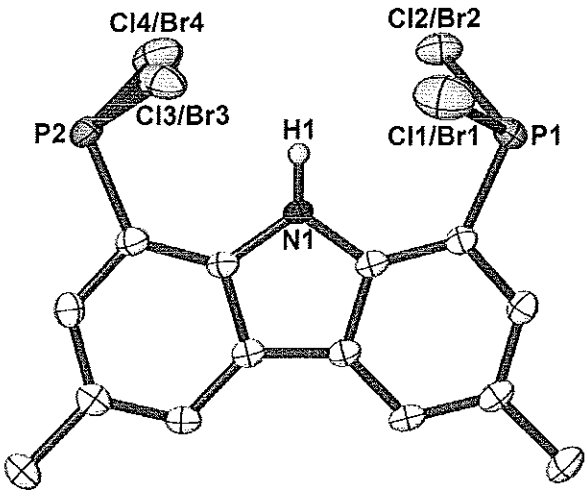

Figure 4.4 Molecular representation of the bis(dichlorophosphine/bromine) (**25**) at the 50% probability level. Hydrogen atoms, except H_1, have been removed for clarity.

4.4.2 Synthesis of HL_2^{Me}

Difficulties surrounding the removal of residual copper during the synthesis of HL_2^{Me} have prompted the investigation of alternate synthetic strategies. Replacing bromine with fluorine at the 1,8-positions of carbazole should allow for alternate aromatic nucleophilic substitution pathways without the need for a metal catalyst. To accomplish this, a series of chemical precursors must first be synthesized. Preparation of 2-fluoro-4-methylphenyl trifluoromethanesulfonate can be achieved by the reaction of the relatively inexpensive 2-fluoro-4-methylaniline ($71, 100 g, Matrix Scientific) with one equivalent of ^{n}Bu-nitrite, forming the diazonium salt

(Scheme 4.12).[168] Addition of triflic acid with loss of N_2 gas yields the desired 2-fluoro-4-methylphenyl trifluoromethanesulfonate (Scheme 4.12).[168]

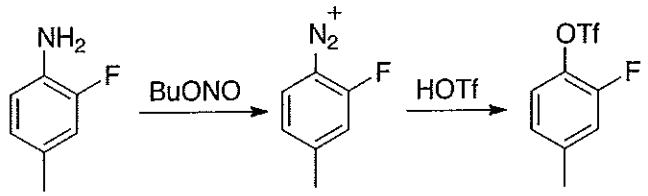

Scheme 4.12 Synthesis of 2-fluoro-4-methylphenyl trifluoromethanesulfonate.

The resultant 2-fluoro-4-methylphenyl trifluoromethanesulfonate can be reacted with 2-fluoro-4-methylaniline under palladium coupling conditions to yield the fluorinated diphenylamine.[168] An additional palladium coupling reaction will allow for ring closure, generating the desired 1,8-difluoro-3,6-dimethyl-9H-carbazole.[169] Reaction with the pyrazole salt should allow for installation of the pyrazole rings, with the loss of KF.

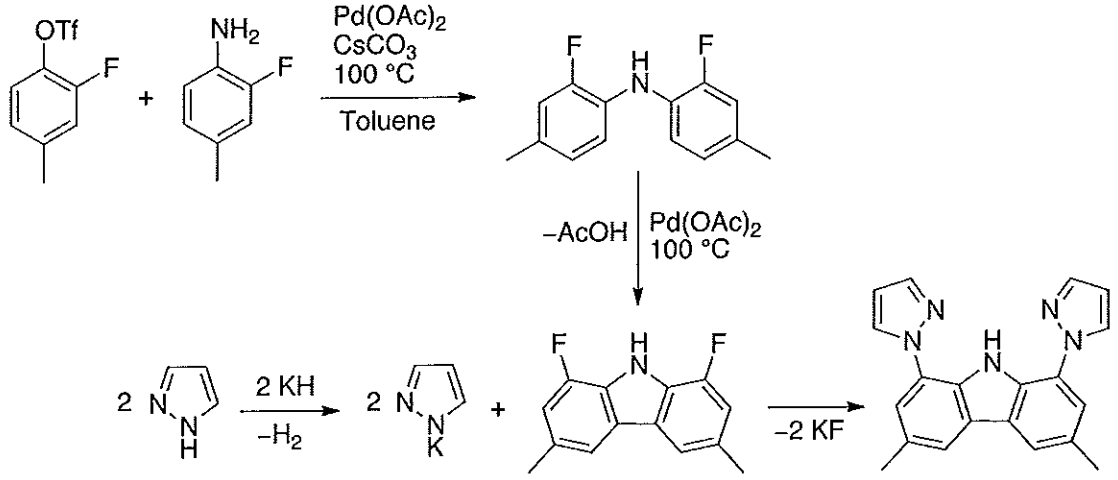

Scheme 4.13 Alternative synthesis of HL_2.

While this approach involves a total of 6 synthetic steps, if product requiring less taxing purification is acquired it might prove beneficial from a time perspective.

In addition, it is a more atom economical route, as an excess of starting materials should not be required to drive complete product formation.

4.5 Conclusions

The development of two novel pincer ligands and their subsequent organolanthanide reactivity was presented in this thesis. While both scaffolds were carbazole-based, careful steric and electronic tuning at the 1,8-positions resulted in two unique ancillaries. The bulkier bis(phosphinimine)carbazole ligand **11** offers greater peripheral steric protection with respect to the metal centre. This additional bulk, however, yields thermally unstable lanthanide dialkyl compounds, whereby decomposition occurs *via* an intramolecular C–H bond activation. This decomposition pathway appears to be directly correlated to the size of the lanthanide metal, with *N*-aryl or phospholane metalation observed for lutetium and scandium, respectively. In comparison to previous work within the Hayes group, the rate of decomposition is substantially reduced, and this can likely be attributed to the constrained phospholane rings in comparison to a diphenylphosphine group.

In attempts to mitigate cyclometalation, a reduction of steric bulk and enhanced ligand rigidity was desired. This in turn resulted in the design of a bis(pyrazolyl)carbazole (HL_2^{Me}) ligand. These modifications proved critical for the synthesis and isolation of thermally stable rare earth dialkyl compounds, in which lutetium (**18**) and scandium (**19**) complexes were readily formed and isolated. In addition, compounds **18** and **19** exhibit enhanced thermal stability in benzene

solution, with no decomposition of either complex observed after 48 hours at 75 °C. Preliminary investigations have also demonstrated that derivatization of the alkyl groups can be achieved in the presence of an appropriate aniline. As such, the CzPz ligand family is expected to serve as an instrumental framework in the future development of organolanthanide chemistry.

Chapter 5

Experimental

5.1 General Procedures

5.1.1 Laboratory Equipment and Apparatus

Unless otherwise specified, all synthetic manipulations were performed under the exclusion of water and oxygen by employing an inert atmosphere using either a double manifold high-vacuum line with Kontes Teflon valves, or an MBraun Labmaster 130 glovebox. Specialty glassware utilized for air-sensitive reactions included swivel frit apparati and thick walled (5 mm) glass bombs (herein referred to as bombs), equipped with Kontes Teflon valves.[170] Glassware for air and moisture sensitive reactions were stored in an oven set to 115 °C for a minimum of 12 hours prior to use, or heat-flamed with the aid of a Bunsen burner, allowing for direct use, and immediately assembled on the vacuum line or placed in the glovebox antechamber while hot and evacuated.

5.1.2 Solvents and Purification

Solvents for air and moisture sensitive reactions were obtained from an MBraun Solvent Purification System (SPS), and further dried and degassed in 500 mL bombs over the following drying agents/indicators: sodium benzophenone ketyl (diethyl ether, tetrahydrofuran), "titanocene" (benzene, pentane, toluene), or CaH_2 (dichloromethane). Unless otherwise specified, solvents for air-sensitive reactions were transferred into reaction vessels under reduced pressure and temperature (–78 °C) by means of condensation. Air and moisture stable syntheses utilized solvents obtained from EMD (chloroform, dichloromethane, diethyl ether, dimethylformamide, ethyl acetate, *n*-hexanes, THF), without requirement of further purification.

Deuterated solvents for NMR spectroscopy were dried over sodium benzophenone ketyl (benzene-d_6, toluene-d_8), or CaH_2 (chloroform-*d*, dichloromethane-d_2), and degassed *via* multiple freeze-pump-thaw cycles, followed by distillation into bombs containing molecular sieves (4 Å) and stored under argon.

Water/ice (0 °C), dry ice/acetone (–78 °C), liquid nitrogen/acetone (–94 °C), and liquid nitrogen (–196 °C) baths were used to cool receiving flasks and maintain low temperatures conditions for thermally sensitive reactions.

5.1.3 NMR Spectroscopy

Unless otherwise specified, all NMR spectroscopy data were acquired at ambient temperature (~295 K) using a Bruker Avance II (Ultrashield) 300 MHz

NMR spectrometer (^{1}H 300.13 MHz, ^{13}C{^{1}H} 75.47 MHz, ^{31}P{^{1}H} 121.49 MHz). NMR spectroscopy data is reported in ppm, where ^{1}H and ^{13}C{^{1}H} shifts are referenced to $SiMe_4$ through internal residual ^{1}H and ^{13}C resonance(s), respectively, of the employed solvent: chloroform-*d* (7.27 ppm, 77.36 ppm), benzene-d_6 (7.16 ppm, 128.0 ppm), toluene-d_8 (2.09, 6.98, 7.02, 7.09 ppm, 20.4, 125.2, 128.0, 128.9, 137.5 ppm). ^{31}P{^{1}H} spectra were referenced to an external standard of 85% H_3PO_4.

^{1}H NMR spectral data are presented in the following format: chemical shift (ppm), multiplicity, J = coupling constant (Hz), number of protons, assignment. ^{13}C{^{1}H} NMR spectral data are listed using the following system: chemical shift (ppm), J = coupling constant (Hz), assignment. ^{31}P{^{1}H} NMR spectral data are listed by chemical shift.

5.1.4 Kinetic Analysis

With respect to each kinetic experiment performed on compound **12**, a consistent amount of ligand (0.0091 g) and stoichiometric equivalent of $Lu(CH_2SiMe_3)_3(THF)_2$ (0.0083 g) were measured into an NMR tube. The tube was sealed using a rubber septum, and the seal between the rubber septum and glass was covered with parafilm. The NMR tube was then placed in a block of dry ice to reduce decomposition of the tris(alkyl) lutetium complex. Prior to inserting the tube into the probe, 0.5 mL of toluene-d_8 was injected into the NMR tube through the septum *via* syringe. The tube was vigorously shaken to ensure mixing, and placed back into the block of dry ice. Additional parafilm was utilized to cover the resultant hole following injection. For experiments performed at variable temperatures, the

probe was set to the desired temperature prior to inserting the sample. Progress of the reaction was monitored by integration of the $^{31}P\{^{1}H\}$ NMR spectrum, in which the dialkyl compound **12** was integrated to a constant of 1 and the decomposition product integrated with respect to it. Each trial was followed to at least 3 half lives, and the run at 295.3 K was repeated an additional 2 times to ensure experimental replicability.

5.1.5 Computational Methodology

All calculations were performed using the Gaussian 09 software suite.[171] Crystallographic data of **11** and **17** served as the input for calculations on the proteo ligands, which were allowed to freely optimize at the B3WP91/6-31G(d,p) level of theory in benzene (ε = 2.2706) using the IEF-PCM formalism,[117] to ensure accuracy of the functional and the basis set. The DFT functional B3WP91 is similar to B3LYP, in that it is a hybrid functional. Therefore, it accounts for electron correlation but determines the electron exchange using Hartree Fock methodology on the Kohn Sham derived orbitals, which are representative of the electron density. The dialkyl lanthanide compounds were generated from their respective ligand structures, in which the ligand scaffold remained conserved and the N_1–Ln bond length determined by the van der Waals radii of the two atoms. In cases where THF was included, the THF molecules were added explicitly either in the coordination sphere of the metal centre, or outside of the binding pocket. The remaining bond lengths (Ln–C, C–Si), and angles (Ln–C–Si), were input based off of typical literature values. Optimization of the resultant lanthanide dialkyls was performed using B3WP91 in

benzene, whereby the C, H, N, Si, and where pertinent, O and P atoms were treated with the 6-31G(d,p) basis set. Alternatively, the lanthanide centre was treated using the appropriate Gaussian basis sets pre-determined by the Dolg group, and are presented below (Table 5.1) with their respective effective core pseudopotential (ECP) keyword in brackets.

Table 5.1 Basis sets employed for calculations performed on lanthanide containing compounds. Effective core pseudopotentials (ECP) are in brackets.

Sc (ECP10MDF)	**Y** (ECP28MWB)	**Lu** (ECP60MWB)
Sc 0	Y 0	Lu 0
S 3 1.00	S 3 1.00	S 3 1.00
10.0092600 1.0078960	5.1329580 -1.3875107	0.14711137D+02 -
8.4707620 -1.1766550	4.2401920 1.9445128	0.26965788D-01
4.1791160 -0.8026470	1.2982800 0.4416434	0.86536100D+01
S 1 1.00	S 1 1.00	0.20615318D+00
1.0692080 1.0	0.8321130 1.0	0.40118673D+01 -
S 1 1.00	S 1 1.00	0.60390795D+00
0.4412480 1.0	0.3499050 1.0	S 1 1.00
S 1 1.00	S 1 1.00	0.81506793D+00 1.0
0.0644320 1.0	0.0665510 1.0	S 1 1.00
S 1 1.00	S 1 1.00	0.37556587D+00 1.0
0.0272000 1.0	0.0286590 1.0	S 1 1.00
S 1 1.00	S 1 1.00	0.15000000D+00 1.0
0.0100000 1.0	0.0100000 1.0	S 1 1.00
P 2 1.00	P 2 1.00	0.42603697D-01 1.0
41.7118460 0.0209120	2.7279200 -3.5841846	S 1 1.00
6.0260150 -1.0073290	1.9790500 3.0212057	0.89254406D-02 1.0
P 2 1.00	P 2 1.00	P 3 1.00
2.7159950 0.2536440	0.8734760 0.4638586	0.13173490D+02
1.0569140 0.7926430	0.4410670 0.5708554	0.31057924D-02
P 1 1.00	P 1 1.00	0.77491117D+01
0.3769410 1.0	0.1838150 1.0	0.31120224D-01
P 1 1.00	P 1 1.00	0.45583010D+01 -
0.0741610 1.0	0.0605670 1.0	0.15497780D+00
P 1 1.00	P 1 1.00	P 1 1.00
0.0238050 1.0	0.0222360 1.0	0.10011764D+01 1.0
D 4 1.00	D 4 1.00	P 1 1.00
16.2735480 0.0355590	2.9007090 -0.0838205	0.41273600D+00 1.0
4.8000490 0.1693560	2.0997920 0.1525870	P 1 1.00
1.5412930 0.4204460	0.6182520 0.4792681	0.15000000D+00 1.0

0.4681800 0.6173140 D 1 1.00 0.1227990 1.0 D 1 1.00 0.0400000 1.0 F 1 1.00 0.7640000 1.0 F 1 1.00 0.1800000 1.0 G 1 1.00 0.3470000 1.0	0.2001840 0.6007504 D 1 1.00 0.0611890 1.0 D 1 1.00 0.0200000 1.0 F 1 1.00 0.5460000 1.0 F 1 1.00 0.1440000 1.0 G 1 1.00 0.2490000 1.0	P 1 1.00 0.10324844D-01 1.0 D 2 1.00 0.87055557D+01 0.55803150D-02 0.51209151D+01 - 0.21434218D-01 D 1 1.00 0.11009145D+01 1.0 D 1 1.00 0.41703790D+00 1.0 D 1 1.00 0.15000000D+00 1.0 D 1 1.00 0.51183520D-01 1.0 F 1 1.00 1.48693098 1.0 F 1 1.00 0.67996558 1.0 F 1 1.00 0.20223572 1.0 G 1 1.00 1.75606667 1.0 G 1 1.00 0.73168508 1.0

Unlike other atoms in the periodic table, the rare earth metals cannot be treated with a standard basis set, as these basis sets are not optimized for including the complicated *f* orbitals. As such, each lanthanide metal has its own unique basis set that compliments a specific pseudopotential. Pseudopotentials are used to represent a "valence-only" type model, or frozen core approximation, for a given atom, therefore reducing the computational load by neglecting the core electrons and treating only the valence electrons. They also take into account relativistic contributions. Relativistic effects are observed in many-electron atoms, and are a result of changes in molecular orbital energies due to shielding of the valence

electrons by the core electrons.[172] This results in competition for orbital occupation of a given electron. In particular, for the *f*-elements, relativistic effects are quite large, and increase exponentially by the fourth power of the nuclear charge.[172]

With respect to the lanthanides, the 4*f* electrons are treated as core electrons as they are not involved in chemical bonding, and the 6*s* and 5*d* represented as the valence orbitals.[iii158] This can be achieved by implementing the effective core pseudopotentials (ECP) from the Stuttgart/Cologne group, whereby three types of pseudopotentials, non-relativistic, relativistic, and scalar- or quasi-relativistic, are known. The keywords to implement the ECP are written in the form ECPnXY, whereby: n = the number of core electrons represented by the pseudopotential; X is the reference system of the pseudopotential (X = S represents a single-valence electron ion or X = M represents a neutral atom); Y is the level of theory of the reference system (Y = WB refers to the Wood-Boring quasirelativistic calculation; Y = DF refers to a Dirac-Fock relativistic calculation; Y = HF refers to a Hartree-Fock calculation). In the case of scandium, a fully relativistic pseudopotential (DF) was employed, as quasi-relativistic pseudopotentials are unknown, and DF is proven to provide greater accuracy than HF.

Once a structure had been optimized, frequency calculations were performed using the same level of theory to ensure that an energy minima and not maxima (transition state) had been achieved. This is indicated by all vibrational frequencies

[iii] Treatment of only the 4*f* orbitals is referred to as the small-core pseudopotentials (SPPs), or 4*f*-in core, and treat electrons from the 1*s*-4*f* orbitals as core electrons. For larger lanthanide compounds with complex bonding motifs, the large-core pseudopotentials (LPPs), are required.

being greater than zero. Due to the complexity of the calculations, and variability in the basis sets, zero-point vibration energies (ZPVE) were not scaled with a ZPVE correction factor. Where energetic comparisons have been made, single-point calculations (SPC) were performed with an expanded basis-set (6-311G+(2d,p)) for the atoms C, H, N, and where applicable, O and P, again at the B3WP91 level of theory. The basis set and ECP for the respective rare earth metal was kept the same. Energy values were scaled with the appropriate ZPVE determined by the respective frequency calculation, as outlined by Equation 1.

$$E_{\text{molecule}} = E_{\text{SPC}} + \text{ZPVE}$$

Equation 1

Relative energies were calculated by the following formula:

$$(E_{\text{max}} - E_{\text{min}}) \times 2625.5$$

Equation 2

whereby values were converted from Hartrees (H) to $kJ \cdot mol^{-1}$ by the conversion factor of 2625.5.

5.1.6 Other Instrumentation and Analysis

Elemental analyses of C, H, and N content were performed using an Elementar Americas Vario MicroCube instrument, by Drs. Craig Wheaton and Kevin Johnson at the University of Lethbridge.

5.1.7 Materials

Solutions of *n*-BuLi (1.6 M, hexanes), and *t*-BuLi (1.7 M, pentane), were obtained from Sigma-Aldrich and used as received. The reagents cupric oxide, 3-methylpyrazole, potassium *tert*-butoxide, tetramethylethylenediamine, trichlorophosphine, tribromophosphine, magnesium, 1,4-dibromobutane, diethylamine, 2-mercaptopyrimidine, tetrabutylammonium bromide, potassium carbonate, dimethyl carbonate, chlorine gas, and sodium azide, were obtained from Strem and Alfa Aesar, and used as received. Deuterated solvents were obtained from Cambridge Isotope Laboratories.

The compounds diethylaminodichlorophosphine,[111] 3,6-dibromo-9H-carbazole,[112] 3,6-dimethyl-9H-carbazole,[112] 1,8-dibromo-3,6-dimethyl-9H-carbazole,[112] 1,8-dibromo-3,6-dimethyl-9-*t*BOC-carbazole,[64] $Sc(CH_2SiMe_3)_3(THF)_2$,[68] $Lu(CH_2SiMe_3)_3(THF)_2$,[68] and $Y(CH_2SiMe_3)_3(THF)_2$[173] were prepared according to literature procedures.

5.1.8 Preparation of Materials from Modified Procedures

Synthesis of $ClP(C_4H_8)$[110]

Magnesium turnings (9.09 g, 374 mmol) were added to a reflux apparatus equipped with a 2-neck 500 mL round bottom flask. 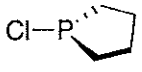

Anhydrous diethyl ether (200 mL) was added to the turnings under reduced pressure and temperature (–78 °C). While refluxing at 35 °C, 1,4-dibromobutane (11.2 mL, 93.8 mmol) was added dropwise to the ethereal solution and the mixture

was allowed to stir for 1.25 h. An additional aliquot of 1,4-dibromobutane (11.2 mL, 93.8 mmol) was added to the reaction mixture, which was then allowed to stir for a further 1.5 h. The resultant solution was transferred *via* cannula into a 1 L flask. Diethylaminodichlorophosphine (24.5 mL, 168 mmol), diluted in anhydrous diethyl ether (150 mL), was added dropwise to the Grignard solution at reduced temperature (–78 °C), and the solution was allowed to stir for 3 h. The resulting solution was transferred to a distillation apparatus, and the remaining magnesium salts were washed with pentane. Both the diethyl ether and pentane were distilled at 40 °C (oil bath temperature), yielding a yellow oil. The oil was transferred to a separate distillation apparatus, in which the product was distilled under full static vacuum (~0.01 torr) at 96 °C (oil bath temperature). The distilled 1-diethylaminophospholane (13.72 g, 86.2 mmol) was added to a 100 mL bomb, where at –78 °C, 11.6 mL (85.5 mmol) of dichlorophenylphosphine was added dropwise. After the addition, the bomb was sealed and cooled to –35 °C for 2 d. The product was then distilled under dynamic vacuum between 60 °C and 75 °C (oil bath temperature). The NMR data matched that reported in the literature.[110] Yield: 8.57 g (69.9 mmol, 41.6%). ^{1}H NMR (benzene-d_6): δ 1.80 (m, 4H, PCH_2), 1.30 (m, 4H, PCH$_2$CH_2). ^{31}P{^{1}H} NMR (benzene-d_6): δ 126.44.

Synthesis of Pyrimidine Azide[161-162]

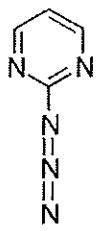

A 250 mL round bottom flask was charged with 2-mercaptopyrimidine (1.682 g, 15.00 mmol), tetrabutylammonium bromide (0.9677 g, 3.000 mmol), potassium carbonate (3.107 g, 22.50 mmol), and dimethyl carbonate (24.32 g, 0.2700 mol). With the presence of a condenser, the

resulting slurry was heated to 90 °C in an oil bath for a period of 3 h with constant stirring. The resulting orange solution was cooled to ambient temperature and filtered to remove residual potassium carbonate. Following an aqueous work-up (2 × 25 mL), the organic layer was dried over $MgSO_4$, filtered, and the solvent removed *in vacuo*, yielding a canary yellow oil. The oil was dissolved in $_{dd}H_2O$, transferred to a 100 mL bomb, and cooled in an ice bath. Chlorine gas was continually bubbled through the solution until dissolution of the oil in water occurred. The pH of the solution was adjusted to a value of 8 using potassium carbonate, and the product extracted from water using chloroform (3 × 15 mL). The chloroform was removed under reduced pressure, then the residue was reconstituted in dimethylformamide (2 mL). To the dimethylformamide solution, an excess of sodium azide (0.9715 g, 14.94 mmol) was added, and the resulting solution heated in an oil bath at 100 °C for 3 h. The resulting red solution was diluted with chloroform (30 mL), and filtered to remove unreacted sodium azide. Concentration yielded orange crystals. Yield: 0.2534 g (2.092 mmol, 42.00%). ^{1}H NMR data matched the published data.[160]

Synthesis of 3,6-dimethylpyrimidine azide[161]

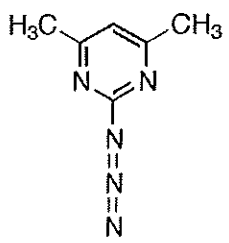

Sodium azide (0.6256 g, 8.054 mmol) was added to a 100 mL round bottom flask containing 2-methylsulfonylpyrimidine (0.5001 g, 2.685 mmol), and the reagents were dissolved in dimethylformamide (5 mL). The solution was heated at 90 °C in an oil bath for 3 h, following which the solution was cooled to ambient temperature, diluted with chloroform, and filtered. The resulting orange solution was

concentrated to yield orange crystals. Yield: 0.3308 g (0.2217 mmol, 82.60%). ^{1}H NMR data matched that published in the literature.[160]

5.2 Experimental Procedures Pertaining to Chapter 2

5.2.1 Synthesis of Compounds

Synthesis of 1,8-bis(phospholano)-3,6-dimethyl-9-^{t}BOC-carbazole (9)

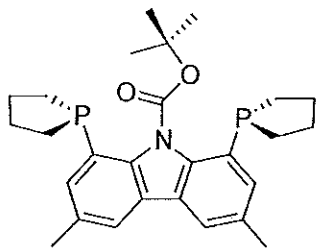

To a solution of 1,8-dibromo-3,6-dimethyl-9-^{t}BOC-carbazole (1.01 g, 2.24 mmol) in diethyl ether (80 mL), 1.7 M *t*-BuLi in pentane (2.63 mL, 4.47 mmol) was added dropwise at –78 °C. The solution was stirred at this temperature for 3.5 h, during which time the colour changed from yellow to persimmon red. At –78 °C, ClP(C_4H_8) (0.470 mL, 4.47 mmol) was added, causing the solution to become a light brown colour. The solution was allowed to gradually warm to ambient temperature while stirring over 18 h, resulting in a yellow solution. After removing the solvent under vacuum, an orange-yellow powder ensued. In a glovebox, the powder was reconstituted in toluene (25 mL) and filtered to remove any residual LiCl. Toluene was removed from the filtrate under vacuum, to afford a thick yellow oil. Yield: 0.535 g (1.14 mmol, 51.2%) (Note: This is a crude yield as the resulting product was not analytically pure. During synthesis, this compound slowly begins to deprotect, and as such, both **9** and **10** were found within the reaction mixture. Due to this, **9** is usually not isolated, and simply deprotected to **10** immediately. As such, EA data was not obtained.) ^{1}H NMR (benzene-d_6): δ 7.30

(s, 2H, Ar-*H*), 7.26 (s, 2H, Ar-*H*), 2.50–1.67 (br ov m, 16H, CH_2), 2.23 (s, 6H, CH_3), 1.53 (s, 9H, CH_3). $^{13}C\{^1H\}$ (benzene-d_6): 152.93 (s, COO^{t}Bu), 142.87 (d, $^1J_{CP}$ = 6.04 Hz, aromatic *ipso*–C), 135.00 (s, Ar–*C*), 134.54 (s, aromatic *ipso*–C), 133.69 (s, aromatic *ipso*–C), 130.55 (d, $^1J_{CP}$ = 12.85 Hz, aromatic *ipso*–C), 118.86 (s, Ar–*C*), 84.94 (s, ^{t}Bu *ipso*–C), 28.03 (s, ^{t}Bu CH_3), 27.81 (d, $^2J_{CP}$ = 2.3 Hz, P–CH_2), 27.69 (d, $^1J_{CP}$ = 10.6 Hz, P–CH_2), 20.98 (s, Ar–CH_3). $^{31}P\{^1H\}$ NMR (benzene-d_6): δ –8.89.

Synthesis of 1,8-bis(phospholano)-3,6-dimethyl-9-H-carbazole (10)

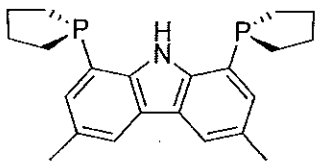

Compound **9** (0.535 g, 1.14 mmol) was reconstituted in toluene (30 mL) in a 100 mL bomb, affording an amber coloured solution. The solution was heated at 155 °C for 2 h to remove the *t*-BOC protecting group. Afterwards, the solution was transferred *via* cannula to a 100 mL flask, and the solvent removed under vacuum, resulting in a yellow oil. Additional washing of the oil with pentane (10 mL) resulted in the formation of a butter-yellow precipitate. The precipitate was dissolved in additional pentane (20 mL) and filtered. Following a period of 1 day at ambient temperature, pale yellow plate-like crystals developed. The mother liquor was decanted, and the crystals were dried under vacuum. Yield: 0.409 g (1.10 mmol, 96.5%). ^1H NMR (benzene-d_6): δ 9.16 (s, 1H, N*H*), 7.81 (s, 2H, Ar*H*), 7.24 (s, 2H, Ar*H*), 2.45 (s, 6H, CH_3), 2.09–1.31 (br ov m, 16H, CH_2). $^{13}C\{^1H\}$ (benzene-d_6): δ 141.40 (d, $^1J_{CP}$ = 18.9 Hz, aromatic *ipso*–C) 128.13 (s, Ar–*C*), 123.19 (s, aromatic *ipso*–C), 122.29 (s, aromatic *ipso*–C), 121.96 (s, aromatic *ipso*–C), 120.78 (s, Ar–*C*), 28.28 (d, $^2J_{CP}$ = 3.0 Hz, P–CH_2), 25.78 (d, $^1J_{CP}$ = 11.3 Hz, P–CH_2), 21.55 (Ar–CH_3). δ $^{31}P\{^1H\}$ NMR

(benzene-d_6): δ –35.58. Anal. Calcd. (%) for $C_{21}H_{27}P_2N$: C, 71.92; H, 7.41; N, 3.81. Found: C, 72.14; H, 7.80; N, 4.05.

Synthesis of HL_1^{Pipp} (11)

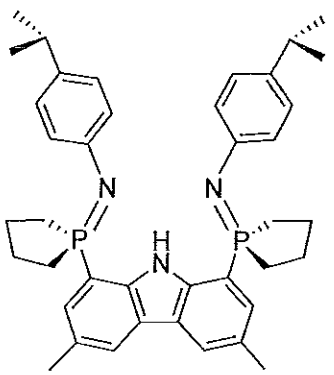

Pentane (30 mL), was added to a 100 mL round bottom flask containing 1,8-bis(phospholano),3,6-dimethyl-9-H-carbazole (0.2030 g, 0.5525 mmol) under reduced temperature (–78 °C) and pressure. Using a syringe, *para*-isopropylphenyl azide (0.1789 g, 1.105 mmol) was added dropwise at ambient temperature, resulting in a pale yellow solution. The solution was allowed to stir for 18 h, after which the solvent was removed under vacuum, affording a fluffy yellow solid. Recrystallization from benzene-d_6/pentane yielded pale yellow crystals. Yield: 0.1940 g (0.3061 mmol, 58.2%) ^{1}H NMR (benzene-d_6): δ 12.55 (s, 1H, N*H*), 7.80 (s, 2H, Ar*H*), 7.31 (d, $^2J_{HH}$ = 7.2 Hz, 4H, Ar*H*), 7.22 (s, 2H, Ar*H*), 7.11 (d, $^2J_{HH}$ = 7.8 Hz, 4H, Ar*H*), 2.79 (sp, $^2J_{HH}$ = 6.9 Hz, 2H, C*H*), 2.36 (s, 6H, CH_3), 2.33-1.35 (br ov m, 16H, CH_2), 1.22 (d, $^3J_{HH}$ = 6.9 Hz, 12H, CH_3). ^{13}C{^{1}H} NMR (benzene-d_6): δ 151.03 (d, $^1J_{CP}$ = 3.8 Hz, aromatic *ipso*–C), 141.30 (s, aromatic *ipso*–C), 137.87 (s, aromatic *ipso*–C), 128.39 (s, Ar–*C*), 128.07 (s, aromatic *ipso*–C), 127.47 (s, aromatic *ipso*–C), 124.49 (s, aromatic *ipso*–C), 124.05 (d, $^3J_{CP}$ = 8.3 Hz, Ar–*C*), 123.60 (s, Ar–*C*), 123.39 (s, Ar–*C*), 34.19 (s, *C*H(CH_3)$_2$), 27.26 (d, $^1J_{CP}$ = 64.3 Hz, P–*C*H_2), 25.92 (d, $^2J_{CP}$ = 11.3 Hz, P–*C*H_2), 25.09 (s, CH(*C*H_3)$_2$), 21.83 (s, Ar–*C*H_3). ^{31}P{^{1}H} NMR (benzene-d_6): δ 31.30. Anal. Calcd. (%) for $C_{40}H_{49}P_2N_3$: C, 75.80; H, 7.79; N, 6.63. Found: C, 75.41; H, 7.66; N, 6.85.

***In situ* Generation of $(L_1^{Pipp})Lu(CH_2SiMe_3)_2$ (12)**

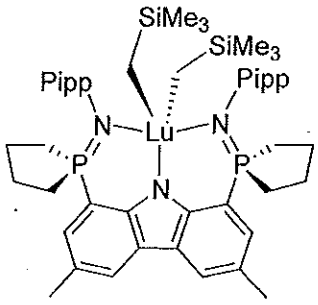

An NMR tube was charged with **11** (0.0091 g, 0.014 mmol) and $Lu(CH_2SiMe_3)_3(THF)_2$ (0.0083 g, 0.014 mmol). Benzene-d_6 (0.5 mL) was added to the tube at ambient temperature to afford a pale yellow solution. ^{1}H NMR (benzene-d_6): δ 8.14 (s, 2H, Ar*H*), 7.25 (d, $^2J_{HH}$ = 1.5 Hz, 4H, Ar*H*), 7.22 (d, $^2J_{HH}$ = 1.8 Hz, 4H, Ar*H*), 7.03 (s, 2H, Ar*H*), 2.70 (sp, $^3J_{HH}$ = 0.97 Hz, 2H, CH), 2.50 (s, 6H, Ar–C*H*$_3$), 2.12-1.64 (br ov m, 16H, C*H*$_2$), 1.16 (d, $^3J_{HH}$ = 6.9 Hz, 12H, C*H*$_3$), 0.14 (s, 18H, Si(C*H*$_3$)$_3$), –0.57 (s, 4H, Lu-C*H*$_2$). ^{13}C{^{1}H} NMR (toluene-d_8, 213 K): δ 152.11 (s, aromatic *ipso*–C), 144.22 (d, $^1J_{CP}$ = 6.8 Hz, aromatic *ipso*–C), 142.68 (s, aromatic *ipso*–C), 137.07 (s, aromatic *ipso*–C), 136.96 (s, aromatic *ipso*–C), 126.62 (s, Ar–*C*), 126.50 (s, Ar–*C*), 126.37 (s, Ar–*C*), 124.36 (s, Ar–*C*), 124.22 (s, Ar–*C*), 112.21 (s, Ar–*C*), 111.07 (s, Ar–*C*), 70.97 (s, Lu–*C*H$_2$), 33.40 (s, *C*H(CH$_3$)$_2$), 30.09 (s, P–*C*H$_2$), 24.22 (s, P–*C*H$_2$), 24.08 (s, CH(*C*H$_3$)$_2$), 21.41 (s, Ar–*C*H$_3$), 4.69 (s, Si(*C*H$_3$)$_3$),. ^{31}P{^{1}H} NMR (benzene-d_6): δ 54.61. *In situ* formation and thermal instability of complex **12** rendered analytically pure samples for EA analysis impossible. As such, this data was not obtained.

Decomposition of (12) to (13)

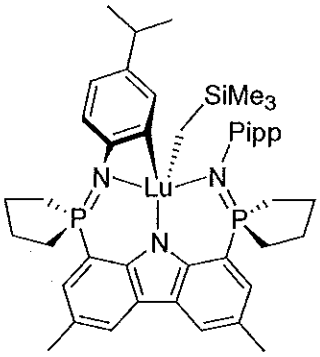

An NMR tube containing **12** was allowed to sit at ambient temperature over a period of 4 hours to generate the asymmetric decomposition product **13**. This decomposition product is also thermally sensitive, resulting in further decomposition to a variety of unknown products at ambient

temperature over a time period of 4 hours. ^{1}H NMR (benzene-d_6): 8.17 (s, 1H, Ar*H*), 8.11 (s, 1H, Ar*H*), 7.56 (s, 1H, Ar*H*), 7.31 (s, 1H, Ar*H*), 7.09 (s, 1H, Ar*H*), 7.08 (d, $^{2}J_{HH}$ = 3.3 Hz, 2H, Ar*H*), 7.06 (s, 1H, Ar*H*), 6.96 (s, 1H, Ar*H*), 6.92 (s, 1H, Ar*H*), 6.87 (s, 1H, Ar*H*), 2.75-2.66 (ov sp, 2H, CH), 2.56 (s, 3H, Ar–CH_3), 2.52 (s, 3H, Ar–CH_3), 2.34-1.46 (br ov m, 16H, CH_2), 1.18 (d, $^{3}J_{HH}$ = 6.9 Hz, 6H, CH_3), 1.14 (d, $^{3}J_{HH}$ = 6.9 Hz, 6H, CH_3), 0.54 (s, 9H, Si(CH_3)$_3$), 0.47 (s, 2H, Lu–CH_2), ^{31}P{^{1}H} NMR (benzene-d_6): δ 55.85, 53.08. *In situ* formation and thermal instability of complex **13** rendered acquisition of ^{13}C NMR data and isolation of analytically pure samples for EA analysis impossible. As such, this data was not obtained.

***In situ* Generation of (L_1^{Pipp})Sc(CH$_2$SiMe$_3$)$_2$ (14)**

Compound **11** (0.0097 g, 0.016 mmol) was added to an NMR tube containing Sc(CH$_2$SiMe$_3$)$_3$(THF)$_2$ (0.0072 g, 0.016 mmol), and dissolved in benzene-d_6. The resulting orange solution slowly decomposed at ambient temperature over a period of 3 hours. ^{1}H NMR (benzene-d_6): δ 8.14 (s, 2H, Ar*H*), 7.04 (s, 4H, Ar*H*), 7.02 (s, 4H, Ar*H*), 6.98 (s, 2H, Ar*H*), 2.91 (sp, $^{3}J_{HH}$ = 0.97 Hz, 2H, CH), 2.51 (s, 6H, ArCH_3), 2.15-1.51 (br ov m, 16H, CH_2), 1.19 (d, $^{3}J_{HH}$ = 6.9 Hz, 12H, CH_3), 0.018 (s, 18H, Si(CH_3)$_3$), –0.19 (s, 4H, ScCH_2). ^{31}P{^{1}H} NMR (benzene-d_6): δ 54.97. *In situ* formation and thermal instability of complex **14** rendered rendered acquisition of ^{13}C NMR data and isolation of analytically pure samples for EA analysis impossible. As such, this data was not obtained.

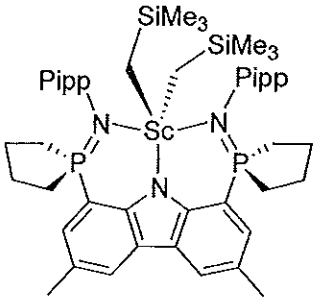

Decomposition of (14) to (16)

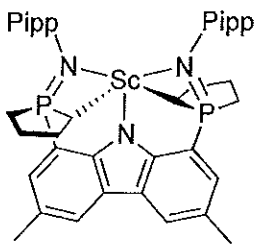

An NMR tube containing **14** was left at ambient temperature over a period of 24 hours to afford the symmetric, doubly metalated species **16** with the concomitant loss of two equivalents of tetramethylsilane. ^{1}H NMR (benzene-d_6): δ 7.85 (s, 2H, Ar*H*), 7.48 (d, $^{3}J_{HP}$ = 11.1 Hz, 2H, Ar*H*), 7.12 (d, $^{2}J_{HH}$ = 8.4 Hz, 2H, Ar*H*), 6.99 (d, $^{2}J_{HH}$ = 8.4 Hz, 2H, Ar*H*), 2.74 (sp, $^{3}J_{HH}$ = 6.8 Hz, 2H, C*H*), 2.51 (s, 6H, ArCH_3), 2.14-1.23 (br ov m, 12H, CH_2), 1.12 (d, $^{3}J_{HH}$ = 6.6 Hz, 12H, CH_3). ^{13}C{^{1}H} NMR (benzene-d_6): 151.33 (d, $^{1}J_{CP}$ = 4.5 Hz, aromatic *ipso*–C), 148.55 (s, aromatic *ipso*–C), 148.47 (s, aromatic *ipso*–C), 138.58 (s, Ar–*C*), 127.10 (s, Ar–*C*), 124.58 (s, aromatic *ipso*–C), 124.24 (s, Ar–*C*), 120.48 (d, $^{2}J_{CP}$ = 15.8 Hz, Ar–*C*), 115.56 (s, aromatic *ipso*–C), 114.63 (s, aromatic *ipso*–C), 33.52 (s, *C*H(CH$_3$)$_2$), 32.20 (s, Sc-*C*H), 32.16 (d, $^{2}J_{CP}$ = 3.8 Hz, P–CH$_2$*C*H$_2$), 30.18 (d, $^{2}J_{CP}$ = 17.4 Hz, P–CH$_2$*C*H$_2$), 24.3 (s, CH(*C*H$_3$)$_2$), 21.53 (d, $^{1}J_{CP}$ = 43.8 Hz, P–*C*H$_2$), 21.60 (s, Ar–*C*H$_3$). ^{31}P{^{1}H} NMR (benzene-d_6): δ 56.24. *In situ* formation and thermal instability of complex **16** rendered isolation of analytically pure samples for EA analysis impossible. As such, this data was not obtained.

5.3 Experimental Procedures Pertaining to Chapter 3

5.3.1 Synthesis of Compounds

Synthesis of HL_2^{Me} (17)

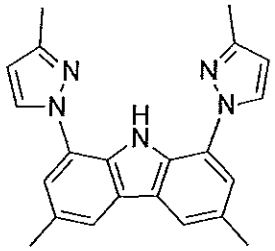

Under an inert atmosphere, K^{t}BuO (1.9395 g, 0.0172 mol) was transferred to a 150 mL, 2-neck round bottom flask equipped with a refluxing condenser. Dimethylformamide (25 mL) was added *via* syringe, and the slurry stirred for 15 minutes under argon. Pyrazole (3.5470 g, 0.0432 mol), and TMEDA (2.0090 g, 0.0172 mol), were added to the slurry *via* syringe, followed by the addition of Cu_2O (2.0642 g, 0.0216 mol) and 1,8-dibromo-3,6-dimethyl-9H-carbazole (1.5265 g, 0.004320 mol). Under constant stirring and an inert atmosphere, the reagents were heated to reflux at 150 °C for a period of 62 h. Afterwards, the solution was allowed to cool, and 80 mL of DCM was added. A saturated solution of $NH_4Cl_{(aq)}$ was added to the organic layer, and the two solutions were allowed to stir until the aqueous layer turned blue, at which point it was decanted. This process was repeated until the aqueous layer was no longer coloured. The organic layer was separated with the aid of a separatory funnel. The organic solvent was removed *in vacuo*, resulting in a forest green powder. The powder was reconstituted in a 1:1 solvent mixture of hexanes:ethyl acetate, and purified by filtering through a silica column approximately 1 cm in diameter and 20 cm long. The resulting pale yellow solution was dried over $MgSO_4$, filtered, and the organic solvents removed *in vacuo*. Yield:

0.1359 g (0.3823 mmol, 13.50%). ^{1}H NMR (chloroform-*d*): δ 11.66 (s, 1H, N*H*), 8.03 (d, $^2J_{HH}$ = 2.4 Hz, 2H, Ar*H*), 7.76 (s, 2H, Ar*H*), 7.32 (s, 2H, Ar*H*), 6.34 (d, $^2J_{HH}$ = 2.4 Hz, 2H, Ar*H*), 2.59 (s, 6H, ArCH_3), 2.55 (s, 6H, ArCH_3). ^{13}C NMR (chloroform-*d*): δ 150.01 (s, aromatic *ipso*–C), 129.98 (s, aromatic *ipso*–C), 128.51 (s, aromatic *ipso*–C), 127.78 (s, Ar*C*), 125.58 (s, aromatic *ipso*–C), 124.60 (s, aromatic *ipso*–C), 118.07 (s, Ar–*C*), 115.16 (s, Ar–*C*), 106.92 (s, Ar–*C*), 22.92 (s, Ar–*C*H$_3$), 14.36 (s, Ar–*C*H$_3$). Anal. Calcd. (%) for $C_{22}H_{21}N_5$: C, 74.34; H, 5.96; N, 19.70. Found: C, 69.47; H, 5.80; N, 16.12.

Synthesis of (L_2^{Me})Lu(CH_2SiMe_3)$_2$ (18)

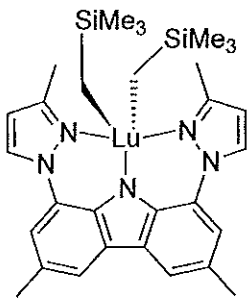

Benzene was added to a flask charged with **17** (0.1092 g, 0.3072 mmol) and Lu(CH_2SiMe_3)$_3$(THF)$_2$ (0.1784 g, 0.3072 mmol), resulting in an orange solution. The solution was allowed to stir at ambient temperature for 2 hours to ensure reaction completion. The solvent was removed *in vacuo*, yielding an orange solid. Yield: 73.67% (0.1593 g, 0.2263 mmol). ^{1}H NMR (benzene-d_6): δ 7.87 (s, 2H, Ar*H*), 7.42 (d, $^2J_{HH}$ = 2.4 Hz, 2H, Ar*H*), 6.87 (s, 2H, Ar*H*), 5.83 (d, $^2J_{HH}$ = 2.4 Hz, 2H, Ar*H*), 2.76 (s, 6H, ArCH_3), 2.41 (s, 6H, ArCH_3), –0.23 (s, 18H, Si(CH_3)$_3$), –0.30 (s, 4H, LuCH_2). ^{13}C{^{1}H} NMR (benzene-d_6): δ 153.73 (s, aromatic *ipso*–C), 138.36 (s, aromatic *ipso*–C), 131.56 (s, aromatic *ipso*–C), 130.97 (s, Ar–*C*), 127.21 (s, aromatic *ipso*–C), 125.73 (s, aromatic *ipso*–C), 119.72 (s, Ar–*C*), 117.95 (s, Ar–*C*), 108.61 (s, Ar–*C*), 29.93 (s, Lu–*C*H$_2$), 21.01 (s, Ar–*C*H$_3$), 14.94 (s, Ar–*C*H$_3$), 3.17 (s, Si(*C*H$_3$)$_3$). Anal. Calcd. (%) for $C_{30}H_{42}LuN_5Si_2$: C, 51.19; H, 6.01; N, 9.95. Found: C, 43.22; H, 5.59; N, 7.22.

Synthesis of $(L_2^{Me})Sc(CH_2SiMe_3)_2$ (19)

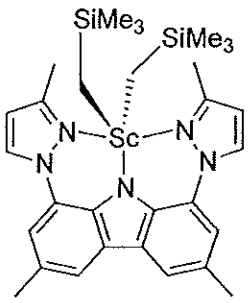

To a flask charged with **17** (0.0260 g, 0.0731 mmol) and $Sc(CH_2SiMe_3)_3(THF)_2$ (0.0330 g, 0.0731 mmol), benzene (10 mL), was added, resulting in a light orange solution. The solution was allowed to stir for 2 hours, after which the solvent was removed *in vacuo*, resulting in an orange solid. Yield: 86.70% (0.0364 g, 0.0634 mmol). ^{1}H NMR (benzene-d_6): δ 7.81 (s, 2H, Ar*H*), 7.51 (d, $^2J_{HH}$ = 2.4 Hz, 2H, Ar*H*), 6.97 (s, 2H, Ar*H*), 5.88 (d, $^2J_{HH}$ = 2.4 Hz, 2H, Ar*H*), 2.85 (s, 6H, ArCH_3), 2.41 (s, 6H, ArCH_3), 0.35 (s, 4H, ScCH_2), –0.34 (s, 18H, Si(CH_3)$_3$). ^{13}C{^{1}H} NMR (benzene-d_6): δ 153.38 (s, aromatic *ipso*–C), 137.03 (s, aromatic *ipso*–C), 129.98 (s, aromatic *ipso*–C), 128.61 (s, aromatic *ipso*–C), 127.72 (s, aromatic *ipso*–C), 125.52 (s, Ar–*C*), 119.85 (s, Ar–*C*), 117.71 (s, Ar–*C*), 109.14 (s, Ar–*C*), 40.61 (br s, Sc–*C*H_2), 21.68 (s, Ar–*C*H_3), 16.61 (s, Ar–*C*H_3), 3.13 (Si(*C*H_3)$_3$). Anal. Calcd. (%) for $C_{30}H_{42}ScN_5Si_2$: C, 62.79; H, 7.38; N, 12.20. Found: C, 51.18; H, 5.32; N, 12.15.

In situ Generation of $(L_2^{Me})Y(CH_2SiMe_3)_2$ (20)

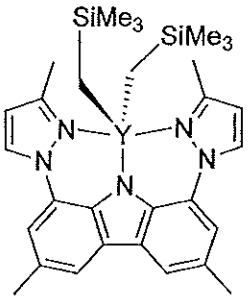

Compound **17** (0.0093 g, 0.026 mmol) and $Y(CH_2SiMe_3)_3(THF)_2$ (0.013 g, 0.026 mmol), were added to an NMR tube and dissolved in benzene-d_6, resulting in a deep orange solution. ^{1}H NMR (benzene-d_6): δ 7.88 (s, 2H, Ar*H*), 7.37 (d, $^2J_{HH}$ = 2.4 Hz, 2H, Ar*H*), 6.83 (s, 2H, Ar*H*), 5.82 (d, $^2J_{HH}$ = 2.4 Hz, 2H, Ar*H*), 2.76 (s, 6H, ArCH_3), 2.41 (s, 6H, ArCH_3), –0.14 (d, $^2J_{YH}$ = 2.7 Hz, 4H, YCH_2), –0.18 (s, 18H, Si(CH_3)$_3$). ^{13}C{^{1}H} NMR (benzene-d_6): δ 153.71 (s, aromatic *ipso*–C), 138.65 (s, aromatic *ipso*–C), 132.36 (s, aromatic *ipso*–C), 128.71 (s, Ar–*C*), 126.94 (s,

aromatic *ipso*-C), 125.79 (s, aromatic *ipso*-C), 120.39 (s, Ar-*C*), 119.40 (s, Ar-*C*), 108.98 (s, Ar-*C*), 35.85 (d, $^1J_{CY}$ = 38.6 Hz, Y-*C*H_2), 21.57 (s, Ar-*C*H_3), 15.60 (s, Ar-*C*H_3), 3.74 (s, Si(*C*H_3)$_3$).

***In situ* Generation of (L_2^{Me})Lu(CH_2SiMe_3)(NHMes*) (21)**

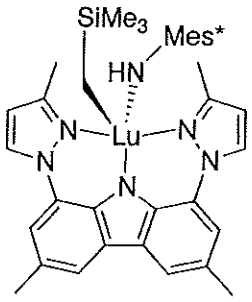

To an NMR tube containing 0.0103 g (0.0146 mmol) of **18**, one equivalent of 2,4,6-tri-*tert*-butylaniline (Mes*NH_2) (0.0038 g, 0.0146 mmol) was added. The reagents were dissolved in benzene-d_6, and heated at 50 °C for 19 hours, yielding the mixed alkyl/anilido compound **21**. ^{1}H NMR (benzene-d_6): δ 7.94 (s, 2H, Ar*H*), 7.39 (d, $^2J_{HH}$ = 2.7 Hz, 2H, Ar*H*), 7.34 (s, 2H, aniline Ar*H*), 6.81 (s, 2H, Ar*H*), 5.81 (d, $^2J_{HH}$ = 2.4 Hz, 2H, Ar*H*), 3.45 (s, 1H, Lu-N*H*), 2.77 (s, 6H, ArC*H*$_3$), 2.43 (s, 6H, ArC*H*$_3$), 1.36 (d, $^2J_{HH}$ = 5.1 Hz, 18H, *o*-^{t}Bu-C*H*$_3$), 1.33 (s, 9H, *p*-^{t}Bu-C*H*$_3$), -0.19 (s, 9H, Si(C*H*$_3$)$_3$), -0.21 (s, 2H, Lu-C*H*$_2$). ^{13}C{^{1}H} NMR (benzene-d_6): 154.83 (s, aromatic *ipso*-C), 153.60 (s, aromatic *ipso*-C), 139.57 (s, aromatic *ipso*-C), 135.91 (s, aromatic *ipso*-C), 134.50 (s, aromatic *ipso*-C), 132.56 (s, Ar-*C*), 127.24 (s, aromatic *ipso*-C), 126.24 (s, aromatic *ipso*-C), 122.41 (s, anilido Ar-*C*), 120.18 (s, Ar-*C*), 119.51 (s, Ar-*C*), 109.19 (s, Ar-*C*), 35.30 (s, anilido *C*(CH$_3$)$_3$), 34.90 (s, *C*(CH$_3$)$_3$), 32.72 (s, C(*C*H$_3$)$_3$), 30.59 (s, C(*C*H$_3$)$_3$), 30.31 (s, Lu-*C*H$_2$), 21.60 (s, Ar-*C*H$_3$), 17.10 (s, Ar-*C*H$_3$), 3.61 (s, Si(*C*H$_3$)$_3$).

***In situ* Generation of $(L_2^{Me})Sc(NHMes)_2$ (22)**

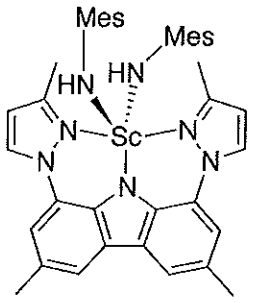

Compound **19** (0.0122 g, 0.0213 mmol), was added to an NMR tube and dissolved in benzene-d_6. With the aid of a microsyringe, 2,4,6-trimethylaniline (0.0057 g, 0.0425 mmol) was added. The creamsicle orange reaction was allowed to proceed at ambient temperature over a period of 24 hours, yielding the doubly substituted $(L_2^{Me})Sc(NHMes)_2$. ^{1}H NMR (benzene-d_6): δ 7.92 (s, 2H, Ar*H*), 7.31 (d, $^2J_{HH}$ = 2.4 Hz, 2H, Ar*H*), 6.86 (s, 2H, Ar*H*), 6.66 (s, 2H, Ar*H*), 5.59 (d, $^2J_{HH}$ = 2.4 Hz, 2H, Ar*H*), 2.86 (s, 2H, N*H*), 2.63 (s, 6H, ArCH_3), 2.47 (s, 6H, ArCH_3), 2.13 (s, 3H, *p*-ArCH_3), 2.09 (s, 6H, *o*-ArCH_3). ^{13}C{^{1}H} NMR (benzene-d_6): δ 154.88 (s, aromatic *ipso*–C), 151.20 (s, aromatic *ipso*–C), 141.19 (s, aromatic *ipso*–C), 137.71 (s, aromatic *ipso*–C), 130.77 (s, Ar–*C*), 129.53 (s, anilido Ar–*C*), 127.45 (s, aromatic *ipso*–C), 125.84 (s, aromatic *ipso*–C), 124.32 (s, aromatic *ipso*–C), 122.35 (s, aromatic *ipso*–C), 119.70 (s, Ar–*C*), 117.93 (s, Ar–*C*), 109.73 (s, Ar–*C*), 21.69 (s, Ar–CH_3), 21.00 (s, anilido Ar–CH_3), 20.05 (s, anilido Ar–CH_3), 15.83 (s, Ar–CH_3).

5.4 Experimental Procedures Pertaining to Chapter 4

5.4.1 Synthesis of Compounds

Synthesis of $HL_1^{2,4\text{-diMePym}}$ (23)

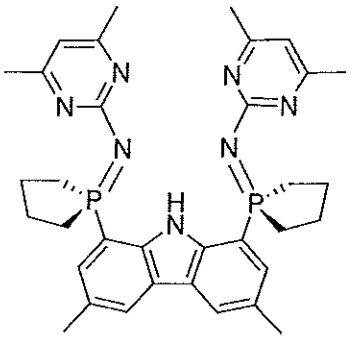

To a vial containing **10** (0.0706 g, 0.1922 mmol), 2,4-dimethylpyrimidine azide was added (0.0573 g, 0.3843 mmol). The solids were dissolved in 15 mL of benzene and allowed to stir over 48 hours, after which the solvent was removed *in vacuo*, affording a golden yellow solid. Yield: 56.68% (0.0664 g, 0.1089 mmol) ^{1}H NMR (benzene-d_6): δ 13.26 (s, 1H, N*H*), 7.85 (s, 2H, Ar*H*), 7.55 (d, $^3J_{HP}$ = 13.2 Hz, 2H, Ar*H*), 5.95 (s, 2H, Ar*H*), 3.11-1.57 (br ov m, 8H, CH_2), 2.41 (s, 6H, ArCH_3), 2.10 (s, 12H, ArCH_3). ^{13}C{^{1}H} NMR (benzene-d_6): δ 167.26 (d, $^1J_{CP}$ = 3.8 Hz, aromatic *ipso*–C), 141.09 (s, aromatic *ipso*–C), 131.18 (s, aromatic *ipso*–C), 130.40 (s, aromatic *ipso*–C), 128.92 (s, Ar–*C*), 124.79 (s, Ar–*C*), 124.13 (s, aromatic *ipso*–C), 124.02 (s, aromatic *ipso*–C), 109.68 (s, Ar–*C*), 26.52 (d, $^1J_{CP}$ = 7.5 Hz, P–*C*H$_2$), 24.10 (d, $^2J_{CP}$ = 3.8 Hz, P–*C*H$_2$), 23.96 (s, Ar–*C*H$_3$), 21.78 (s, Ar–*C*H$_3$). ^{31}P{^{1}H} NMR (benzene-d_6): δ 50.72.

In situ Generation of $(L_1^{2,4\text{-diMePym}})Lu(CH_2SiMe_3)_2$ (24)

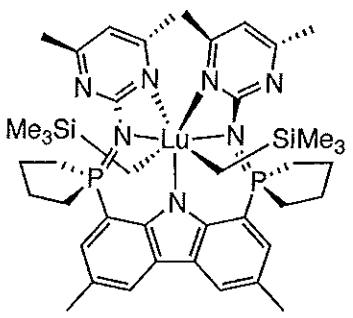

An NMR tube was charged with 0.0099 g of **23** (0.0123 mmol) and Lu(CH$_2$SiMe$_3$)$_3$(THF)$_2$ (0.0071 g, 0.0123 mmol). Benzene-d_6 was added to dissolve the reagents, yielding a bright red solution. Within 10 minutes at ambient temperature, the compound began to decompose to a mixture of

products, many of which were not soluble in benzene or THF. ^{1}H NMR (benzene-d_6): δ 8.21 (s, 2H, Ar*H*), 7.45 (m, 2H, Ar*H*), 6.01 (s, 2H, Ar*H*), 2.51 (s, 12H, ArCH_3), 2.29 (s, 6H, ArCH_3), –0.24 (s, 18H, Si(CH_3)), –0.59 (s, 4H, Lu–CH_2). ^{31}P{^{1}H} NMR (benzene-d_6): δ 57.18. *In situ* formation and thermal instability of complex **24** rendered rendered acquisition of ^{13}C NMR data and isolation of analytically pure samples for EA analysis impossible. As such, this data was not obtained.

Synthesis of 1,8-(P(Cl/Br)$_2$)$_2$-3,6-dimethyl-9-^{t}BOC-carbazole (25)

Compound **9** (0.5628 g, 1.2419 mmol), was added to a 100 mL round bottom flask. Under reduced temperature (–78 °C) and pressure, Et_2O (60 mL), was added. While still at –78 °C, an excess of ^{t}BuLi (3.00 mL, 5.091 mmol), was added dropwise, yielding a camel coloured solution. The solution was stirred at this temperature for an additional 3.5 hours, after which 2 equivalents of PCl_3 (0.3411 g, 2.4838 mmol) was added dropwise *via* syringe, affording a caramel tone solution which turned canary yellow upon warming to ambient temperature. After stirring for 15 hours, the solvent was removed under vacuum, generating a light yellow solid. ^{1}H NMR (benzene-d_6): δ 10.53 (br s, 1H, N*H*), 7.28 (s, 2H, Ar*H*), 7.24 (d, $^{3}J_{HP}$ = 0.6 Hz, 2H, Ar*H*), 2.05 (s, 6H, ArCH_3), 1.53 (s, 9H, ^{t}BuCH_3). ^{31}P{^{1}H} NMR (benzene-d_6): δ 159.29 (0.48), 159.27 (0.54), 151.46 (0.25), 151.38 (1.00), 140.62 (0.18), 140.55 (0.19).[iv] Anal. Calcd. (%) for $C_{14}H_{11}Cl_4NP_2$: C, 42.35; H, 2.79; N, 3.53; $C_{14}H_{11}Cl_3BrNP_2$: C: 38.09; H: 2.51; N: 3.17;

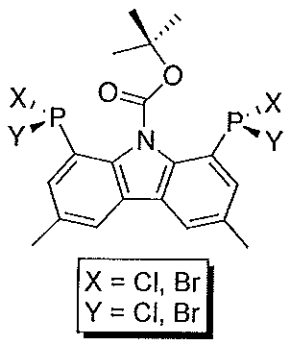

[iv] Numbers presented in brackets are relative intensities of the phosphorus chemical shifts with respect to the ^{31}P{^{1}H} signal at δ 151.38.

$C_{14}H_{11}Cl_2Br_2NP_2$: C: 34.61; H: 2.28; N: 2.88; $C_{14}H_{11}Cl_1Br_3NP_2$: C: 31.71; H: 2.09; N: 2.64; $C_{14}H_{11}Br_4NP_2$: C: 29.25; H: 1.93; N: 2.44. Found (sample recrystallized from benzene): C, 42.55; H, 3.18; N, 3.32. Due to the mixture of compounds formed in the synthesis of **25**, ^{13}C NMR data was not obtained.

5.5 X-ray Crystallography

Crystals of X-ray quality were coated with Paratone oil and placed on a glass slide. The crystals were further analyzed under either a polarizing light microscope or regular light microscope, and one suitable crystal was mounted on a glass fiber attached to the goniometer head. The crystal was mounted and centred on a Bruker SMART APEX II diffractometer equipped with a CCD area-detector, liquid nitrogen controlled KRYO-FLEX cooling device, and molybdenum radiation source (Kα, λ = 0.71073 Å). Crystal data was collected at −100 °C to reduce molecular vibrations. Data collection was performed over a full hemisphere using ω-2θ scans yielding resolutions between 0.78 – 0.84 Å. APEX2[174] software was employed for the refinement of unit cell parameters, whereas Lorentz-polarization correction and absorption corrections were performed using the SAINT-Plus[175] and SADABS[176] software, respectively. Both structures were solved using the SHELXTL[177] software suite using direct methods and refined by least-squares methods. All hydrogen atom positions were implicitly calculated and refined isotropically as riding models of their parent atoms, except for H_1 of **10**, **11**, **17**, and **25**, which were manually located and freely refined. General crystallographic data for compounds **10**, **11**, **17**, and **25**

can be found in Table 5.2, with more detailed parameters presented in the CIF files, located on the attached disc.

***Specific Crystallographic Refinement Details for** 25*

The structure contained substitutionally disordered halide atoms (Cl and Br) bound to all phosphorous atoms (0.48, Cl1 / 0.52, Br1; 0.46, Cl2 / 0.54, Br2; 0.42, Cl3 / 0.58, Br3; 0.48, Cl4 / 0.52, Br4; 0.47, Cl5 / 0.53, Br5; 0.60, Cl6 / 0.40, Br6; 0.39, Cl7 / 0.61, Br7; 0.52, Cl8 / 0.48, Br8). Attempts to restrain the P–Cl and P–Br distances to idealized bond lengths were unsuccessful and gave a poor quality model. Because of this, the P–Cl and P–Br distances were allowed to freely refine; however, theses distances should not be taken to be representative of true P–Cl or P–Br bond distances. Rather, the P–Cl and P–Br bond distances both exhibited very similar values, which can be interpreted as an averaging of the expectedly shorter P–Cl distance and the expectedly longer P–Br distance.

Table 5.2 Summary of X-ray crystallography data collection and structure refinement for compounds **10**, **11**, **17**, and **25**.

	10	**11**[a]	**17**[b]	**25**[c]
Formula	$C_{22}H_{27}NP_2$	$C_{40}H_{49}N_3P_2$	$C_{22}H_{21}N_5$	$C_{14}H_{11}NP_2(XY)_2$
FW /g·mol^{-1}	367.39	633.76	355.44	490.23
Crystal system	Orthorhombic	Monoclinic	Orthorhombic	Triclinic
Space group	*Pbcn*	*C2/c*	*Pbca*	*P-1*
a /Å	6.5804(4)	28.899(9)	11.0022(10)	7.0923(9)
b /Å	17.0388(11)	20.046(6)	14.3599(13)	12.2162(15)
c /Å	17.1877(11)	15.256(5)	23.155(2)	20.326(3)
α /°	90	90	90	87.7290(10)
β /°	90	120.566(3)	90	86.8070(10)
γ /°	90	90	90	77.1540(10)
Volume /Å^3	1927.1(2)	7610(4)	3658.3(6)	1713.6(4)
Z	4	8	8	4
D_{calc} /g·cm^{-3}	1.266	1.106	1.291	1.900
μ /mm^{-1}	0.230	0.144	0.080	5.432
Crystal size /mm^3	0.25 × 0.22 × 0.11	0.21 × 0.19 × 0.08	0.55 × 0.19 × 0.12	0.55 × 0.25 × 0.08
θ range /°	2.37 to 27.10	2.56 to 25.03	1.76 to 25.03	1.71 to 26.02
N	19785	44871	33041	18209
N_{ind}	2132	6711	3222	6724
Data/restraints/parameters	2132 / 0 / 115	6711 / 0 / 413	3222 / 0 / 249	6724/0/463
GoF on F^2	1.091	1.001	1.046	1.047
R_1 (I>2σ(I))[c]	0.0371	0.0766	0.0856	0.0273
wR_2 (I>2σ(I))[d]	0.0960	0.2090	0.2256	0.0686
R_1 (all data)[c]	0.0422	0.1032	0.0980	0.0353
wR_2 (all data)[d]	0.0995	0.2292	0.2367	0.0715
$\Delta\rho_{max}$ and $\Delta\rho_{min}$ /e·Å^{-3}	0.591 and −0.167	0.786 and −0.665	2.761 and −0.215	0.462 and −0.519

Notes: [a]Crystallized with a molecule of benzene and pentane. The electron density associated with these residual solvent molecules was removed from the reflection file using PLATON software and the SQUEEZE function. [b]Contains residual electron density at one of the carbazole methyl groups. [c]Exhibits substitional disorder where X = Cl, Br, and Y = Cl, Br, whereby two molecules co-crystallize in the asymmetric unit.

References

1. Evans, W. J. *Polyhedron* **1987**, *6*, 803.
2. Edelmann, F. T. *Angew. Chem., Int. Ed.* **1995**, *34*, 2466.
3. Gysling, H.; Tsutsui, M. *Adv. Organomet. Chem.* **1970**, *9*, 361.
4. Jensen, W. B. *J. Chem. Educ.* **1982**, *59*, 634.
5. Cotton, S. A. *Coord. Chem. Rev.* **1997**, *160*, 93.
6. Atwood, J. L.; Hunter, W. E.; Rogers, R. D.; Holton, J.; McMeeking, J.; Pearce, R.; Lappert, M. F. *J. Chem. Soc., Chem. Commun.* **1978**, 140.
7. Wilkinson, G.; Birmingham, J. M. *J. Am. Chem. Soc.* **1954**, *76*, 6210.
8. Watson, P. L.; Parshall, G. W. *Acc. Chem. Res.* **1985**, *18*, 51.
9. Bercaw, J. E. *Pure Appl. Chem.* **1990**, *62*, 1151.
10. Thiele, J. *Ber. Dtsch. Chem. Ges.* **1900**, *34*, 666.
11. Birmingham, J. M.; Wilkinson, G. *J. Am. Chem. Soc.* **1956**, *78*, 42.
12. Reed, J. B.; Hopkins, B. S.; Audrieth, L. F. *Inorg. Synth.* **1931**, *1*, 28.
13. Schumann, H.; Meese-Marktscheffel, J. A.; Esser, L. *Chem. Rev.* **1995**, *95*, 865.
14. Watson, P. L.; Whitney, J. F.; Harlow, R. L. *Inorg. Chem.* **1981**, *20*, 3271.
15. Watson, P. L.; Roe, D. C. *J. Am. Chem. Soc.* **1982**, *104*, 6471.
16. Watson, P. L. *J. Am. Chem. Soc.* **1982**, *104*, 337.
17. Evans, W. J. *Inorg. Chem.* **2007**, *46*, 3435.
18. Evans, W. J.; Bloom, I.; Hunter, W. E.; Atwood, J. L. *J. Am. Chem. Soc.* **1981**, *103*, 6507.
19. Evans, W. J.; Hughes, L. A.; Hanusa, T. P. *J. Am. Chem. Soc.* **1984**, *106*, 4270.
20. Evans, W. J.; Davis, B. L. *Chem. Rev.* **2002**, *102*, 2119.
21. Thompson, M. E.; Bercaw, J. E. *Pure Appl. Chem.* **1984**, *56*, 1.
22. Thompson, M. E.; Baxter, S. M.; Bulls, A. R.; Burger, B. J.; Nolan, M. C.; Santarsiero, B. D.; Schaefer, W. P.; Bercaw, J. E. *J. Am. Chem. Soc.* **1987**, *109*, 203.
23. Fendrick, C. M.; Mintz, E. A.; Schertz, L. D.; Marks, T. J. *Organometallics* **1984**, *3*, 819.
24. Bruno, J. W.; Marks, T. J.; Day, V. W. *J. Organomet. Chem.* **1983**, *250*, 237.
25. Piers, W. E.; Shapiro, P. J.; Bunel, E. E.; Bercaw, J. E. *Synlett.* **1990**, *2*, 74.
26. Kim, W.-K.; Fevola, M. J.; Liable-Sands, L. M.; Rheingold, A. L.; Theopold, K. H. *Organometallics* **1998**, *17*.
27. Feldman, J.; McLain, S. J.; Parthasarathy, A.; Marshall, W. J.; Calabrese, J. C.; Arthur, S. D. *Organometallics* **1997**, *16*, 1514.
28. Carey, D. T.; Cope-Eatough, E. K.; Vilaplana-Mafe, E.; Mair, F. S.; Pritchard, R. G.; Warren, J. E.; Woods, R. J. *Dalton Trans.* **2003**, 1083.
29. McGeachin, S. G. *Can. J. Chem.* **1968**, *46*, 1903.
30. Hitchcock, P. B.; Lappert, M. F.; Tian, S. *J. Chem. Soc., Dalton Trans.* **1997**, 1945.
31. Piers, W. E.; Emslie, D. J. H. *Coord. Chem. Rev.* **2002**, *233-234*, 131.
32. Bourget-Merle, L.; Lappert, M. F.; Severn, J. R. *Chem. Rev.* **2002**, *102*, 3031.
33. Hayes, P. G.; Piers, W. E.; McDonald, R. *J. Am. Chem. Soc.* **2002**, *124*, 2132.

34. Shen, X.; Xue, M.; Jiao, R.; Ma, Y.; Zhang, Y.; Shen, Q. *Organometallics* **2012**, *31*, 6222.
35. Sánchez-Barba, L. F.; Hughes, D. L.; Humphrey, S. M.; Bochmann, M. *Organometallics* **2005**, *24*, 3792.
36. Hayes, P. G.; Piers, W. E.; Lee, L. W. M.; Knight, L. K.; Parvez, M.; Elsegood, M. R. J.; Clegg, W. *Organometallics* **2001**, *20*, 2533.
37. Constable, E. C. *Polyhedron* **1984**, *3*, 1037.
38. Kenward, A. L.; Ross, J. A.; Piers, W. E.; Parvez, M. *Organometallics* **2009**, *28*, 3625.
39. Neculai, D.; Roesky, H. W.; Neculai, A. M.; Magull, J.; Schmidt, H.-G.; Noltemeyer, M. *J. Organomet. Chem.* **2002**, *643–644*, 47.
40. Neculai, A. M.; Neculai, D.; Roesky, H. W.; Magull, J. *Polyhedron* **2004**, *23*, 183.
41. Neculai, D.; Roesky, H. W.; Neculai, A. M.; Magull, J.; Herbst-Irmer, R.; Walfort, B.; Stalke, D. *Organometallics* **2003**, *22*, 2279.
42. Xu, X.; Xu, X.; Chen, Y.; Sun, J. *Organometallics* **2008**, *27*, 758.
43. Lu, E.; Li, Y.; Chen, Y. *Chem. Commun.* **2010**, *46*, 4469.
44. Mindiola, D. J. *Acc. Chem. Res.* **2006**, *39*, 813.
45. Giesbrecht, G. R.; Gordon, J. C. *Dalton Trans.* **2004**, 2387.
46. Scott, J.; Basuli, F.; Fout, A. R.; Huffman, J. C.; Mindiola, D. J. *Angew. Chem., Int. Ed.* **2008**, *47*, 8502.
47. Lu, E.; Chu, J.; Chen, Y.; Borzov, M. V.; Li, G. *Chem. Commun.* **2011**, *47*, 743.
48. Chu, J.; Lu, E.; Liu, Z.; Chen, Y.; Leng, X.; Song, H. *Angew. Chem., Int. Ed.* **2011**, *50*, 7677.
49. Chu, J.; Lu, E.; Chen, Y.; Leng, X. *Organometallics* **2012**, *32*, 1137.
50. Wang, C.; Friedrich, S.; Younkin, T. R.; Li, R. T.; Grubbs, R. H.; Bansleben, D. A.; Day, M. W. *Organometallics* **1998**, *17*, 3149.
51. Emslie, D. J. H.; Piers, W. E.; Parvez, M. *Dalton Trans.* **2003**, 2615.
52. Emslie, D. J. H.; Piers, W. E.; MacDonald, R. *J. Chem. Soc., Dalton Trans.* **2002**, 293.
53. Emslie, D. J. H.; Piers, W. E.; Parvez, M.; McDonald, R. *Organometallics* **2002**, *21*, 4226.
54. Hayes, P. G.; Welch, G. C.; Emslie, D. J. H.; Noack, C. L.; Piers, W. E.; Parvez, M. *Organometallics* **2003**, *22*, 1577.
55. Arndt, S.; Spaniol, T. P.; Okuda, J. *Chem. Commun.* **2002**, 896.
56. Lee, L.; Berg, D. J.; Einstein, F. W.; Batchelor, R. J. *Organometallics* **1997**, *16*, 1819.
57. Cameron, T. M.; Gordon, J. C.; Michalczyk, R.; Scott, B. L. *Chem. Commun.* **2003**, 2282.
58. Zimmermann, M.; Törnroos, K. W.; Waymouth, R. M.; Anwander, R. *Organometallics* **2008**, *27*, 4310.
59. Yoshida, Y. M., Shigekazu; Takagi, Yukihiro; Mitani, Makoto; Nitabaru, Masatoshi; Nakano, Takashi; Tanaka, Hidetsugu; Fujita, Terunori *Chem. Lett.* **2000**, *11*, 1270.
60. Matsuo, Y.; Mashima, K.; Tani, K. *Organometallics* **2001**, *20*, 3510.
61. Meyer, N.; Kuzdrowska, M.; Roesky, P. W. *Eur. J. Inorg. Chem.* **2008**, 1475.
62. Gao, W.; Cui, D. *J. Am. Chem. Soc.* **2008**, *130*, 4984.

63. Li, T.; Jenter, J.; Roesky, P. W. *Z. Anorg. Allg. Chem.* **2010**, *636*, 2148.
64. Johnson, K. R. D.; Hayes, P. G. *Organometallics* **2009**, *28*, 6352.
65. Hayes, P. G.; Piers, W. E.; Parvez, M. *Organometallics* **2005**, *24*, 1173.
66. Conroy, K. D.; Hayes, P. G.; Piers, W. E.; Parvez, M. *Organometallics* **2007**, *26*, 4464.
67. Johnson, K. R. D.; Hayes, P. G. *Organometallics* **2011**, *30*, 58.
68. Johnson, K. R. D. Ph.D. Thesis, University of Lethbridge, Lethbridge, AB, 2012.
69. Johnson, K. R. D.; Hayes, P. G. *Chem. Soc. Rev.* **2013**, *42*, 1947.
70. Stephan, D. W.; Stewart, J. C.; Guérin, F.; Spence, R. E. v. H.; Xu, W.; Harrison, D. G. *Organometallics* **1999**, *18*, 1116.
71. Dehnicke, K.; Krieger, M.; Massa, W. *Coord. Chem. Rev.* **1999**, *182*, 19.
72. Aparna, K.; Ferguson, M.; Cavell, R. G. *J. Am. Chem. Soc.* **2000**, *122*, 726.
73. Liddle, S. T.; Mills, D. P.; Wooles, A. J. *Chem. Soc. Rev.* **2011**, *40*, 2164.
74. Liddle, S. T.; Mills, D. P.; Wooles, A. J. *Organomet. Chem.* **2010**, *36*, 29.
75. Gamer, M. T.; Roesky, P. W. *Z. Anorg. Allg. Chem.* **2001**, *627*, 877.
76. Kamalesh Babu, R. P.; Aparna, K.; McDonald, R.; Cavell, R. G. *Inorg. Chem.* **2000**, *39*, 4981.
77. Kasani, A.; Kamalesh Babu, R. P.; McDonald, R.; Cavell, R. G. *Angew. Chem. Int. Ed.* **1999**, *38*, 1483.
78. Ong, C. M.; Stephan, D. W. *J. Am. Chem. Soc.* **1999**, *121*, 2939.
79. Rastätter, M.; Zulys, A.; Roesky, P. W. *Chem.—Eur. J.* **2007**, *13*, 3606.
80. Gamer, M. T.; Dehnen, S.; Roesky, P. W. *Organometallics* **2001**, *20*, 4230.
81. Rastätter, M.; Zulys, A.; Roesky, P. W. *Chem. Commun.* **2006**, 874.
82. Roesky, P. W. *Z. Anorg. Allg. Chem.* **2006**, *632*, 1918.
83. Diez-Gonzalez, S.; Nolan, S. P. *Annual Reports Section "B" (Organic Chemistry)* **2005**, *101*, 171.
84. Aparna, K.; Ferguson, M.; Cavell, R. G. *J. Am. Chem. Soc.* **2000**, *122*, 726.
85. Liddle, S. T.; McMaster, J.; Green, J. C.; Arnold, P. L. *Chem. Commun.* **2008**, 1747.
86. Mills, D. P.; Wooles, A. J.; McMaster, J.; Lewis, W.; Blake, A. J.; Liddle, S. T. *Organometallics* **2009**, *28*, 6771.
87. Buchard, A.; Auffrant, A.; Ricard, L.; Le Goff, X. F.; Platel, R. H.; Williams, C. K.; Le Floch, P. *Dalton Trans.* **2009**, 10219.
88. Wooles, A. J.; Cooper, O. J.; McMaster, J.; Lewis, W.; Blake, A. J.; Liddle, S. T. *Organometallics* **2010**, *29*, 2315.
89. Orzechowski, L.; Jansen, G.; Harder, S. *J. Am. Chem. Soc.* **2006**, *128*, 14676.
90. Mills, D. P.; Cooper, O. J.; McMaster, J.; Lewis, W.; Liddle, S. T. *Dalton Trans.* **2009**, 4547.
91. Mills, D. P.; Soutar, L.; Lewis, W.; Blake, A. J.; Liddle, S. T. *J. Am. Chem. Soc.* **2010**, *132*, 14379.
92. Mills, D. P.; Lewis, W.; Blake, A. J.; Liddle, S. T. *Organometallics* **2013**, *32*, 1239.
93. Mills, D. P.; Soutar, L.; Cooper, O. J.; Lewis, W.; Blake, A. J.; Liddle, S. T. *Organometallics* **2012**, *32*, 1251.
94. Fustier, M.; Le Goff, X. F.; Le Floch, P.; Mézailles, N. *J. Am. Chem. Soc.* **2010**, *132*, 13108.

95. Rong, W.; Liu, D.; Zuo, H.; Pan, Y.; Jian, Z.; Li, S.; Cui, D. *Organometallics* **2012**, *32*, 1166.
96. Edelmann, F. T. *Coord. Chem. Rev.* **2009**, *253*, 2515.
97. Edelmann, F. T. *Coord. Chem. Rev.* **2011**, *255*, 1834.
98. Edelmann, F. T. *Coord. Chem. Rev.* **2012**, *256*, 1151.
99. Masuda, J. D.; Wei, P.; Stephan, D. W. *Dalton Trans.* **2003**, 3500.
100. Li, D.; Li, S.; Cui, D.; Zhang, X.; Trifonov, A. A. *Dalton Trans.* **2011**, *40*, 2151.
101. Li, D.; Li, S.; Cui, D.; Zhang, X. *J. Organomet. Chem.* **2010**, *695*, 2781.
102. Shannon, R. *Acta Crystallogr., Sect. A: Found. Crystallogr.* **1976**, *32*, 751.
103. Bambirra, S.; van Leusen, D.; Meetsma, A.; Hessen, B.; Teuben, J. H. *Chem. Commun.* **2003**, 522.
104. Welch, G. C.; Piers, W. E.; Parvez, M.; McDonald, R. *Organometallics* **2004**, *23*, 1811.
105. Liu, B.; Cui, D.; Ma, J.; Chen, X.; Jing, X. *Chem.—Eur. J.* **2007**, *13*, 834.
106. Conroy, K. D.; Piers, W. E.; Parvez, M. *J. Organomet. Chem.* **2008**, *693*, 834.
107. Giffin, N. A.; Hendsbee, A. D.; Masuda, J. D. *J. Organomet. Chem.* **2011**, *696*, 2533.
108. Zhu, D.; Budzelaar, P. H. M. *Organometallics* **2008**, *27*, 2699.
109. Cariou, R.; Graham, T. W.; Dahcheh, F.; Stephan, D. W. *Dalton Trans.* **2011**, *40*, 5419.
110. Hacklin, H.; Roeschenthaler, G. V. *Phosphorus, Sulfur Silicon Relat. Elem.* **1988**, *36*, 165.
111. King, R. B.; Sadanani, N. D. *Synth. React. Inorg. Met.-Org. Chem.* **1985**, *15*, 149.
112. Britovsek, G. J. P.; Gibson, V. C.; Hoarau, O. D.; Spitzmesser, S. K.; White, A. J. P.; Williams, D. J. *Inorg. Chem.* **2003**, *42*, 3454.
113. Neugebauer, F. A.; Fischer, H. *Chem. Ber.* **1972**, *105*, 2686.
114. Gibson, V. C.; Spitzmesser, S. K.; White, A. J. P.; Williams, D. J. *Dalton Trans.* **2003**, 2718.
115. Johnson, K. R. D.; Hannon, M. A.; Ritch, J. S.; Hayes, P. G. *Dalton Trans.* **2012**, *41*, 7873.
116. Fulmer, G. R.; Miller, A. J. M.; Sherden, N. H.; Gottlieb, H. E.; Nudelman, A.; Stoltz, B. M.; Bercaw, J. E.; Goldberg, K. I. *Organometallics* **2010**, *29*, 2176.
117. Scalmani, G.; Frisch, M. J. *J. Chem. Phys.* **2010**, *132*, 114110.
118. Dolg, M.; Stoll, H.; Savin, A.; Preuss, H. *Theor. Chim. Acta* **1989**, *75*, 173.
119. Ward, B. D.; Gade, L. H. *Chem. Commun.* **2012**, *48*, 10587.
120. Aspinall, H. C.; Greeves, N. *J. Organomet. Chem.* **2002**, *647*, 151.
121. Aspinall, H. C.; Bickley, J. F.; Greeves, N.; Kelly, R. V.; Smith, P. M. *Organometallics* **2005**, *24*, 3458.
122. Desimoni, G.; Faita, G.; Guala, M.; Laurenti, A.; Mella, M. *Chem. – Eur. J.* **2005**, *11*, 3816.
123. Matsumoto, K.; Suzuki, K.; Tsukuda, T.; Tsubomura, T. *Inorg. Chem.* **2010**, *49*, 4717.
124. Morimoto, H.; Lu, G.; Aoyama, N.; Matsunaga, S.; Shibasaki, M. *J. Am. Chem. Soc.* **2007**, *129*, 9588.
125. Lu, G.; Morimoto, H.; Matsunaga, S.; Shibasaki, M. *Angew. Chem., Int. Ed.* **2008**, *47*, 6847.

126. Evans, D. A.; Sweeney, Z. K.; Rovis, T.; Tedrow, J. S. *J. Am. Chem. Soc.* **2001**, *123*, 12095.
127. Qian, C.; Wang, L. *Tetrahedron: Asymmetry* **2000**, *11*, 2347.
128. Hong, S.; Tian, S.; Metz, M. V.; Marks, T. J. *J. Am. Chem. Soc.* **2003**, *125*, 14768.
129. W. Gorlitzer, H.; Spiegler, M.; Anwander, R. *J. Chem. Soc., Dalton Trans.* **1999**, 4287.
130. Zou, J.; Berg, D. J.; Stuart, D.; McDonald, R.; Twamley, B. *Organometallics* **2011**, *30*, 4958.
131. Inoue, M.; Suzuki, T.; Nakada, M. *J. Am. Chem. Soc.* **2003**, *125*, 1140.
132. Marques, N.; Sella, A.; Takats, J. *Chem. Rev.* **2002**, *102*, 2137.
133. Trofimenko, S. *Polyhedron* **2004**, *23*, 197.
134. Trofimenko, S. *J. Chem. Ed.* **2005**, *82*, 1715.
135. Trofimenko, S., *Scorpionates: The Coordination Chemistry of Polypyrazolylborate Ligands*. Imperial College Press: London, 1999.
136. Trofimenko, S. *J. Am. Chem. Soc.* **1966**, *88*, 1842.
137. Takats, J. *J. Alloys Compd.* **1997**, *249*, 52.
138. Blackwell, J.; Lehr, C.; Sun, Y.; Piers, W. E.; Pearce-Batchilder, S. D.; Zaworotko, M. J.; Young Jr, V. G. *Can. J. Chem.* **1997**, *75*, 702.
139. Cheng, J.; Saliu, K.; Kiel, G. Y.; Ferguson, M. J.; McDonald, R.; Takats, J. *Angew. Chem., Int. Ed.* **2008**, *47*, 4910.
140. Wanniarachchi, S.; Liddle, B. J.; Toussaint, J.; Lindeman, S. V.; Bennett, B.; Gardinier, J. R. *Dalton Trans.* **2010**, *39*, 3167.
141. Wanniarachchi, S.; Liddle, B. J.; Toussaint, J.; Lindeman, S. V.; Bennett, B.; Gardinier, J. R. *Dalton Trans.* **2011**, *40*, 8776.
142. Wanniarachchi, S.; Liddle, B. J.; Lindeman, S. V.; Gardinier, J. R. *J. Organomet. Chem.* **2011**, *696*, 3623.
143. Ullmann, F., Bielecki, J. *Ber. Dtsch. Chem. Ges.* **1901**, *34*, 2174.
144. Ullmann, F. *Justus Liebigs Ann. Chem.* **1904**, 38.
145. Sperotto, E.; van Klink, G. P. M.; van Koten, G.; de Vries, J. G. *Dalton Trans.* **2010**, *39*, 10338.
146. Creutz, S. E.; Lotito, K. J.; Fu, G. C.; Peters, J. C. *Science* **2012**, *338*, 647.
147. Giri, R.; Hartwig, J. F. *J. Am. Chem. Soc.* **2010**, *132*, 15860.
148. Tye, J. W.; Weng, Z.; Johns, A. M.; Incarvito, C. D.; Hartwig, J. F. *J. Am. Chem. Soc.* **2008**, *130*, 9971.
149. Jones, G. O. L., P.; Houk, K. N.; Buchwald, S. L. *J. Am. Chem. Soc.* **2010**, *132*, 6205.
150. Klapars, A.; Huang, X.; Buchwald, S. L. *J. Am. Chem. Soc.* **2002**, *124*, 7421.
151. Zhou, H.-P.; Wang, P.; Hu, Z.-J.; Li, L.; Chen, J.-J.; Cui, Y.; Tian, Y.-P.; Wu, J.-Y.; Yang, J.-X.; Tao, X.-T.; Jiang, M.-H. *Eur. J. Inorg. Chem.* **2007**, *2007*, 1854.
152. Kramer, M. U.; Yahia, A.; Maron, L.; Okuda, J. *C. R. Chim.* **2010**, *13*, 626.
153. Becke, A. D. *J. Chem. Phys.* **1993**, *98*, 5648.
154. Perdew, J. P.; Wang, Y. *Phys. Rev. B.* **1992**, *45*, 13244.
155. Maron, L.; Eisenstein, O. *J. Phys. Chem. A* **2000**, *104*, 7140.
156. Labouille, S.; Nief, F.; Le Goff, X.-F.; Maron, L.; Kindra, D. R.; Houghton, H. L.; Ziller, J. W.; Evans, W. J. *Organometallics* **2012**, *31*, 5196.

157. Berkefeld, A.; Piers, W. E.; Parvez, M.; Castro, L.; Maron, L.; Eisenstein, O. *J. Am. Chem. Soc.* **2012**, *134*, 10843.
158. Dolg, M.; Stoll, H.; Preuss, H. *J. Chem. Phys.* **1989**, *90*, 1730.
159. Masuda, J. D.; Jantunen, K. C.; Ozerov, O. V.; Noonan, K. J. T.; Gates, D. P.; Scott, B. L.; Kiplinger, J. L. *J. Am. Chem. Soc.* **2008**, *130*, 2408.
160. Temple, C., Jr.; McKee, R. L.; Montgomery, J. A. *J. Org. Chem* **1965**, *30*, 829.
161. Brown, D. J.; Ford, P. W. *J. Chem. Soc., C* **1967**, 568.
162. Xie, J.-G.; Quan, J.; Li, S.-B.; Zheng, Y.; Zhu, L.-M. *Synth. Commun.* **2011**, *41*, 871.
163. Jantunen, K. C.; Scott, B. L.; Hay, P. J.; Gordon, J. C.; Kiplinger, J. L. *J. Am. Chem. Soc.* **2006**, *128*, 6322.
164. Antilla, J. C.; Baskin, J. M.; Barder, T. E.; Buchwald, S. L. *J. Org. Chem.* **2004**, *69*, 5578.
165. Chmielewski, M. J.; Charon, M.; Jurczak, J. *Org. Lett.* **2004**, *6*, 3501.
166. Chmielewski, M. J. *Synthesis* **2010**, *18*, 3067.
167. Kumar, M. R.; Park, A.; Park, N.; Lee, S. *Org. Lett.* **2011**, *13*, 3542.
168. Mizuno, Y.; Takasu, I.; Uchikoga, S.; Enomoto, S.; Sawabe, T.; Amano, A.; Wada, A.; Sugizaki, T.; Yoshida, J.; Ono, T.; Adachi, C. *J. Phys. Chem. C* **2012**, *116*, 20681.
169. Wentrup, C.; Gaugaz, M. *Helv. Chim. Acta* **1971**, *54*, 2108.
170. Burger Barbara, J.; Bercaw John, E., Vacuum Line Techniques for Handling Air-Sensitive Organometallic Compounds. In *Experimental Organometallic Chemistry*, American Chemical Society: 1987; Vol. 357, pp 79.
171. Frisch, M. J.; Trucks, G. W.; Schlegel, H. B.; Scuseria, G. E.; Robb, M. A.; Cheeseman, J. R.; Scalmani, G.; Barone, V.; Mennucci, B.; Petersson, G. A.; Nakatsuji, H.; Caricato, M.; Li, X.; Hratchian, H. P.; Izmaylov, A. F.; Bloino, J.; Zheng, G.; Sonnenberg, J. L.; Hada, M.; Ehara, M.; Toyota, K.; Fukuda, R.; Hasegawa, J.; Ishida, M.; Nakajima, T.; Honda, Y.; Kitao, O.; Nakai, H.; Vreven, T.; Montgomery, J. A.; Peralta, J. E.; Ogliaro, F.; Bearpark, M.; Heyd, J. J.; Brothers, E.; Kudin, K. N.; Staroverov, V. N.; Kobayashi, R.; Normand, J.; Raghavachari, K.; Rendell, A.; Burant, J. C.; Iyengar, S. S.; Tomasi, J.; Cossi, M.; Rega, N.; Millam, J. M.; Klene, M.; Knox, J. E.; Cross, J. B.; Bakken, V.; Adamo, C.; Jaramillo, J.; Gomperts, R.; Stratmann, R. E.; Yazyev, O.; Austin, A. J.; Cammi, R.; Pomelli, C.; Ochterski, J. W.; Martin, R. L.; Morokuma, K.; Zakrzewski, V. G.; Voth, G. A.; Salvador, P.; Dannenberg, J. J.; Dapprich, S.; Daniels, A. D.; Farkas; Foresman, J. B.; Ortiz, J. V.; Cioslowski, J.; Fox, D. J., Gaussian 09, Revision B.01. Wallingford CT, 2009.
172. Cao, X.; Dolg, M. *Coord. Chem. Rev.* **2006**, *250*, 900.
173. Hultzsch, K. C.; Voth, P.; Beckerle, K.; Spaniol, T. P.; Okuda, J. *Organometallics* **2000**, *19*, 228.
174. *APEX2*, 2.1-4; Bruker AXS: Madison, WI, 2006.
175. *SAINT-Plus*, 7.23a; Bruker AXS: Madison, WI, 2004.
176. Sheldrick, G. M. *SADABS*, 2004/1; Bruker AXS: Madison, WI, 2004.
177. Sheldrick, G. M. *SHELXTL*, 6.14; Bruker AXS: Madison, WI, 2003.